PhD Thesis
Technologies for Injection Molded Antennas for Mass Production

Thesis by compendium of publications

Author : Ivan Zhou

Thesis for the degree of Industrial Doctor of Philosophy
Thesis advisor: Jordi Romeu Robert

A thesis submitted to the Department of Teoria del Senyal i Comunicacions in partial fulfillment of
the requirements for the degree of Industrial Doctor of Philosophy

Universitat Politècnica de Catalunya, September 2022

Dedicated to
Every member of my family
All my friends

Contents

List of publications

This thesis is based on the following publications, referred to by their Roman numerals:

IZ-I   **Technology Assessment of Aperture Coupled Slot Antenna Array in Groove Gapwaveguide for 5G Millimeter Wave Applications**
I. Zhou, L. Jofre and J. Romeu. in IEEE Access, vol. 9, pp. 139556-139564, 2021, doi: 10.1109/ACCESS.2021.3119748

IZ-II   **Ultra-Wideband Narrow Wall Waveguide-to-Microstrip Transition Using Overlapped Patches**
I. Zhou and J. Romeu. Sensors 2022, 22, 2964.

IZ-III   **UltraWideband Microstrip to Waveguide Transition for 5G Millimeter-Wave Applications**
I. Zhou and J. Romeu. 2022 16th European Conference on Antennas and Propagation (EuCAP), 2022, pp. 1-4.

IZ-IV   **Microstrip fed 3D printed H-Sectorial Horn Phased Array**

I. Zhou, L. Pradell, J. M. Villegas, N. Vidal, M. Albert, L. Jofre and J. Romeu. Sensors 2022, 22(14), 5329

All papers are reproduced with permission of their respective publishers.

Acknowledgements

Abstract

The deployment of 5G antenna infrastructure and the mandatory adoption of anti-collision radars for automotive cars will require large amount of antennas operating in the millimeter and sub-millimeter wavelength. These antennas are usually arrays and the possibility to manufacture the antenna array including the feeding network and the radiating element as a plastic piece reducing the need to use large (Printed Circuit Boards) PCB's on expensive dielectric substrates, can be an interesting manufacturing technology. In this regard, waveguide-based antennas can be assembled using plastic technology with a proper metallization procedure. They are more scalable in terms of efficiency than microstrip line (ML) antennas and as the number of antennas in the array increases the gain is not reduced due to the losses in the substrate.

In this thesis, the industrial challenges of this technology are addressed. A detailed tolerance study by including the plastic manufacturing errors, typically $\pm$ 0.1mm, is carried out in order to check the feasibility of plastic antennas to address mass production. The antennas will need to be integrated with the radar chipsets, so a transition between the chip and the waveguide-antennas will be presented. These transitions can act as a direct chip-waveguide launcher, potentially reducing the need of using large substrates, hence reducing the cost of the antenna. Also, the need to apply metal coating is also explored to achieve the desired performance. Conventional techniques such as copper electrodeposition is used. The main drawback is that the copper has a lot of difficulties depositing into right angle surfaces. Eventually, these antennas will have to be integrated in the aesthetics of a car, usually behind a plastic radome (with its respective manufacturing errors as well) that will need to be designed and optimized properly in order to introduce the minimum distorsions to the radar. Optimization based on simulators done with commercial electromagnetic softwares like CST is not feasible due to the required large computation time. In this regard an ad-hoc ray-tracing based simulator has been developed to asses radome induced errors in radar performance.

All these industrial problems are taken into account from the design stage where the time, price, fabrication tolerances and radiation requirements have to be compromised at the same time increasing dramatically the design complexity.

Resumen

El despliegue de infraestructura de antenas 5G y la adopción obligatoria de radares anticolisión para automóviles requerirá una gran cantidad de antenas que operen en longitudes de onda milimétricas y submilimétricas. Estas antenas suelen ser agrupaciones y la posibilidad de fabricar la agrupación de antenas, incluida la red de alimentación y el elemento radiante como una pieza de plástico, lo que reduce la necesidad de usar PCB grandes (placas de circuito impreso) en sustratos dieléctricos costosos, puede ser una tecnología de fabricación interesante. En este sentido, las antenas basadas en guía de ondas se pueden ensamblar utilizando tecnología plástica con un procedimiento de metalización adecuado. Son más escalables en términos de eficiencia que las antenas de línea microstrip (ML) y, a medida que aumenta el número de antenas en el arreglo, la ganancia no se reduce debido a las pérdidas en el sustrato.

En esta tesis se abordan los retos industriales de esta tecnología. Se lleva a cabo un estudio de tolerancia detallado que incluye los errores de fabricación de plástico, normalmente $\pm$ 0,1 mm, para comprobar la viabilidad de las antenas de plástico para hacer frente a la producción en masa. Las antenas deberán integrarse junto con los chips de radar, por lo que se presentará una transición entre el chip y las antenas de guía de ondas. Estas transiciones pueden actuar como una transición directa de chip-guía, lo que podría reducir la necesidad de usar sustratos grandes y, por lo tanto, reducir el costo de la antena. Además, también se explora la necesidad de aplicar un recubrimiento metálico para lograr el rendimiento deseado. Se utilizan técnicas convencionales como la electrodeposición de cobre. El principal inconveniente es que el cobre tiene muchas dificultades para depositarse en superficies en ángulo recto. Eventualmente, estas antenas deberán integrarse en la estética de un automóvil, generalmente detrás de un radomo de plástico (con sus respectivos errores de fabricación también) que deberá diseñarse y optimizarse adecuadamente para introducir las mínimas distorsiones al radar. La optimización basada en simuladores realizados con software electromagnético comercial como CST no es factible debido al gran tiempo de cálculo requerido. En este sentido, se ha desarrollado un simulador basado en trazado de rayos ad-hoc para evaluar los errores inducidos por el radomo en el rendimiento del radar.

Todos estos problemas industriales se tienen en cuenta desde la etapa de diseño donde el tiempo, el precio, las tolerancias de fabricación y los requisitos de radiación tienen que verse comprometidos al mismo tiempo que aumentan drásticamente la complejidad del diseño.

Chapter 1

Introduction

1.1   State of the Art

The first radar patent was registered on 30th April 1904 by Christian Hülsmeyer. At this time, almost all the applications and breakthroughs were exclusively in the military field. After the II World War, different applications were developed in different fields, such as the civil aviation radars, the weather radars, the mapping radars or other different radar applications. In the automotive field, the first ideas and investigations came up in the 1960 s, continuing in the 1970 s by Bendix, Info Systems Inc., RCA, and General Motors, partly supported by the U.S. Department of transportation [1,2,3,4], followed by the Japanese companies Mitsubishi and Nissan. The intended application was precollision obstacle detection and/or emergency braking.

Planar integrated circuits, e.g. microstrip, and integrated antennas were introduced only in the lower frequency range (10 GHz, X-band; 15 GHz, Ku-band); with higher frequencies, waveguide-based circuits and antennas were employed. Distance measurement and collision warning worked well, but of course, technology was not yet mature enough. In the following years, technology of RF devices and circuits as well as signal processing circuits improved considerably. The 24 GHz ISM band became a preferred frequency for low-cost sensors, and the 76–77 GHz band was assigned worldwide for automotive radar.

Some years later, in the early 90's, it started the serial introduction of radars into vehicles in the USA. More than 4000 buses and trucks in the US were equipped with the EATON-VORAD system (Figure 1.1). It used GUNN diode oscillators and planar antennas at the 24GHz band.

Figure 1.1: 24 GHz VORAD radar mounted at the front side of a Greyhound bus [5]

The first commercial 76 GHz automotive radar for passenger cars was introduced 1998/99 by Mercedes Benz (Fig. 1.2). It was built by Macom in the USA [6].
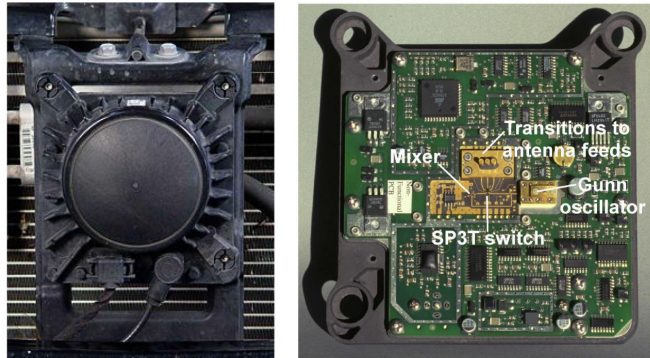
Figure 1.2: Front and back side of first commercial automotive ARS100 radar by Mercedes Benz [5]

The development of SiGe MMICs with several radar channels integrated on a single chip was an important step [7] for the advancement of high density integration and cost reduction. A first radar sensor based on such a chip was the Bosch LRR3 sensor (Figure 1.3). As antenna, a lens configuration [8] was chosen, fed by four separated ML patch feeds, resulting in four beams. Each feed antenna was connected to one of four channels of a SiGe MMIC.

Figure 1.3: Exploded view of the Bosch LRR3 sensor [9]

In Figure 1.4 an overview of the evolution of automotive radars from 1970 to 2000 is shown.
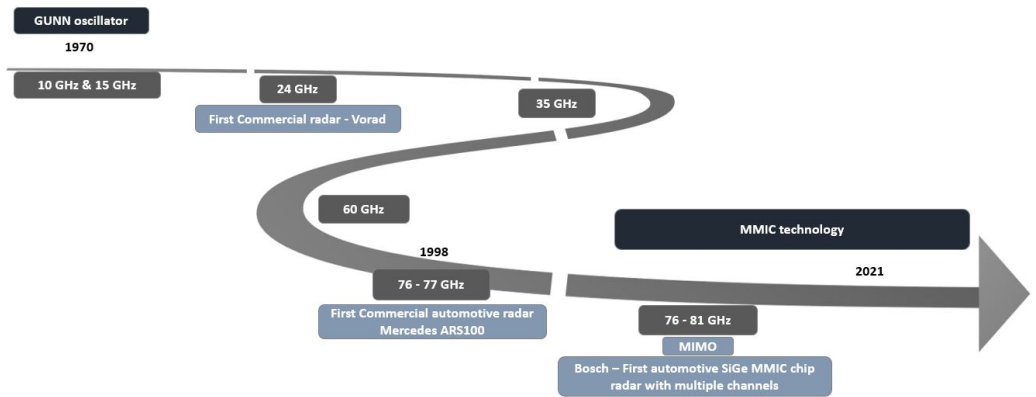
Figure 1.4: Evolution of automotive radars from 1970 to the first SiGe MMIC automotive radar sensor from Bosch

With the easy and relatively low-cost availability of several radar channels on one chip, a new system and antenna configuration became possible with one or more transmit and multiple receive channels, each connected to one antenna element. With several transmit channels, MIMO concepts can be introduced (although, at the beginning, the term MIMO was not used) [10], see Figure 1.5.
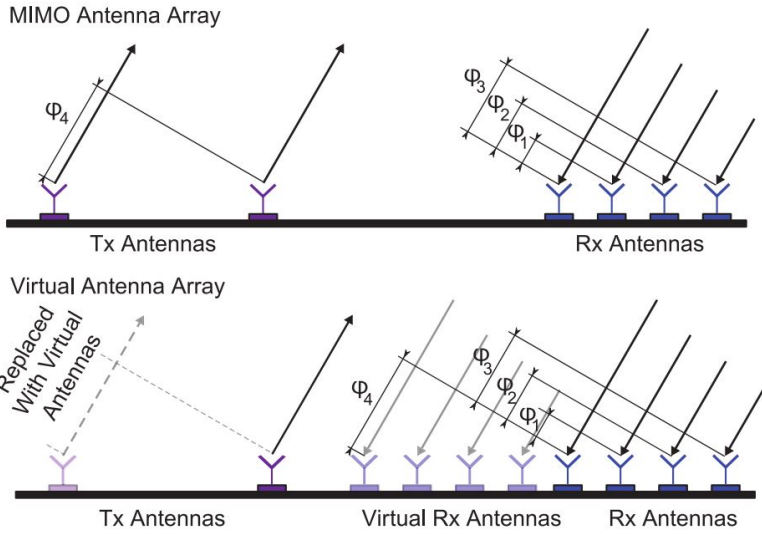
Figure 1.5: Principle of MIMO radar and virtual antennas concept [9]

With proper arrangements of transmitters and receivers, a better target acquisition can be performed because a finer spatial resolution is achieved. This concept now is pursued by many companies like Aptiv, Bosch, Conti, Denso, Hella, Mando, Valeo, or Veoneer. Also startups like Arbe or Uhnder have emerged, presenting their own approach to a high-performance automotive radar.

1.2 Motivation and Objectives

The rapid development of new radar sensor generations is driven by a strong market demand as shown in Figure 1.6, mainly for Advanced Driver Assistance Systems (ADAS), with the market volume starting slowly until 2010 and then massively taking off.
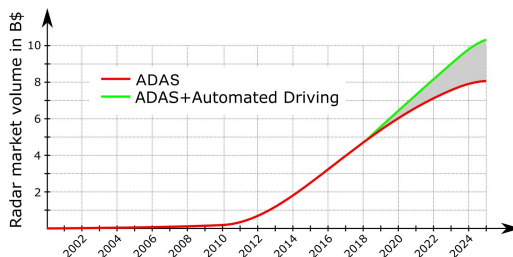
Figure 1.6: Automotive radar market developement for ADAS function [9]

4

This development was fueled by the migration of established driver assistance functions from high class into middle class vehicles, and then further accelerated by the requirement for active safety systems mandated by New Car Assessment Program (NCAP). Ten years later, another market trend towards highperformance radar sensors for ADAS with partial automation and Automated Driving (AD) with full automation is emerging.

The market is expected to almost double its volume by 2025 which obviously will require the double capacity for mass production. The antennas from all the present radar sensors are arrays, see Figure 1.7 and most of them are implemented in expensive dielectric substrates.
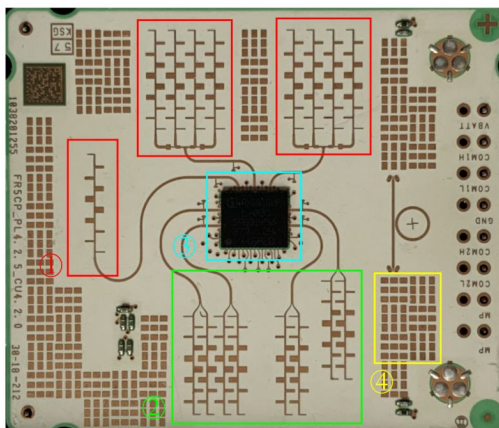
Figure 1.7: Bosch 5th generation radar [9]

As stated in the abstract, the possibility to manufacture the antenna in plastic technology by reducing the use of large substrates can be an interesting manufacturing technology, potentially reducing the costs when the product is massively deployed and improving the antenna performance as the losses can also be decreased. Many companies like Gapwaves, ZF, Bosch and Continental and research institutes like Fraunhofer are already starting to study and implement this technology. As the technology is really recent, many information are still confidential due to Intellectual property issues.

Table 1.1: Evolution of the latest three versions of radars from Continental

Model	FoV (40m)	Weight	$\Delta\theta_{-3dB}$	SLL	Gain Tx	Gain Rx	N Tx	N Rx
ARS410	$\pm45°$,	130g	94.6°	-13dB	18.9dB	13.9dB	2	2
ARS510	$\pm45°$,	140g	60°	-14dB	14dB	14dB	3	4
ARS540	$\pm60°$,	500g	60°	-12dB	14.1dB	14.1dB	5	5

In Tab. 1.1 we show the evolution of the ARS model from Continental. The ARS410 and the ARS510 use microstrip antennas while the ARS540 from this last year uses gapwaveguide technology manufactured using plastic molding processes. It can also be observed a trend to increase the number of transmitting and receiving channels.

Clearly, plastic manufacturing technology is getting the attention worldwide by many big radar companies as mentioned before owing its cheap cost, massive manufacturing potential and radiation performance, with an expected high market impact. In this regard, the objectives of this thesis are summarized as follows:

1. Explore different antenna designs that can be manufactured in plastic and at the same time, they can support tolerances of up to 0.1 mm (which is a standard deviation for a plastic molding process) at W-band (76-81GHz). So it can be mass produced with a guaranteed radiation performance.

2. Integration of the plastic antenna into RF-chips by designing the required transitions.

3. Find the correct metal coating procedure in order to completely metallize the plastic antenna for a proper radiation performance.

4. Study optimal ways of integrating the final prototype antenna into the vehicle, usually behind a radome.

1.3 Thesis Outline

- **Chapter II** is based on the work reported in paper [**IZ-I**] [11] and addresses the objective 1. The design of a Gap-waveguide (GW) antenna suitable for a W-Band automotive radar robust to fabrication tolerances of up to 0.1mm was studied and successfully designed and validated. If the antenna still performs well in terms of radiation properties like S-parameters, gain, tilting angle and sidelobe level (SLL) after a predefined combination of dimensional errors, it can be concluded to be a good candidate for mass production.

- **Chapter III** is based on the work reported in the paper [**IZ-II**] [12] and addresses the objective 2. Every waveguide-based antenna, as in [**IZ-I**], requires of an interconnection with the RF-chips, normally designed as a microstrip line (ML) to rectangular waveguide (RW) transition. A K-band ultra wide-band (UWB) narrow-wall waveguide to ML transition is shown so our waveguide-antenna array can be integrated easily to the chip. An alternative design with a more complicated manufacturing process requiring a metallic short-circuiting box was also designed and validated in W-Band [**IZ-III**] [13].

- **Chapter IV** addresses the objective 3. The last paper [**IZ-IV**] [14] consists in a 3D-printed phased array with low metallization complexity, to show the feasibility of plastic manufacturing technologies for achieving complex antenna systems similar to automotive radars.

- **Chapter V** addresses the objective 4. A software tool was implemented and used for the study of the integration of a plastic cover in front of a radar sensor, showing its impact on the main KPI's of a radar.

- **Chapter VI** shows the conclusions and **Chapter VII** the original publications of each article.

The following Figure 1.8 summarizes the work done in this thesis.
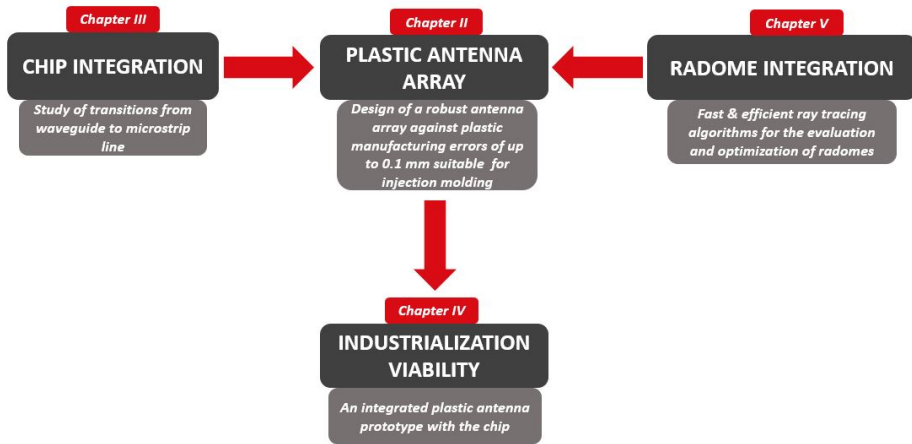
Figure 1.8: Schematic showing each chapter of this thesis

Chapter 2

Antenna Developement For Mass Production

2.1 Introduction

The rapid expansion of the automotive market for ADAS has been massively taken off and it is growing year after year, increasing the demand of radar sensors. These sensors usually use directive beams in the elevation plane and wide beam in the azimuthal plane for a higher Direction of Arrival (DoA) estimation in this plane working in the 76-81GHz band and mainly use arrays of patches in Microstrip-Line (ML) technology as transmitting and receiving antennas for target detection [15]. However, there are two main drawbacks for ML antennas that may limit them for mass production, they are expensive and gain limited by the losses introduced by the substrate [16]. A matter to be alert of is that there is an upcoming band for radars at 144GHz which will definitively require higher gain antennas to face the propagation losses at these higher frequency bands. In addition, these sensors will need to be integrated behind a plastic cover from the car acting as a radome. Commonly used locations are behind the car emblem or a bumper. This integration is usually done by separate companies and of course, the result is not optimum as they are not jointly optimized. Anyways, these plastic covers have radius of curvatures which require conformal antenna geometries that are difficult to provide with conventional substrates when using ML. For all these reasons, is there any technology that may face all the mentioned problems? A low cost, low loss antenna that is robust to mass production and highly integrable behind a radome.

The answer is yes, antennas based on Rectangular-Waveguide (RW) have been fully

explored in this thesis. It is shown that it has high plastic prototyping potential, which is very cheap with very low losses [17],[18]. It seems a very good candidate for automotive radar sensors that may also be scalable to the 144GHz band. As it is plastic, it can be really easy to be integrated in the aesthetics of the car such as a radome. However, some preliminary studies have to be carried out in order to show numerically its advantages with respect to the traditional ML solution. For an antenna to be properly working, the radiation characteristics have to be fulfilled. One of the most important parameters is the input reflection coefficient Γ_{in}, among others such as the gain and SLL.

$$\Gamma_{in} = \frac{Z_{in} - Z_0}{Z_{in} + Z_0} \tag{2.1}$$

In equation 2.1 we can see that the input reflection coefficient Γ_{in} depends on the input impedance Z_{in} and the characteristic impedance Z_0. For an antenna to be robust enough, the input impedance Z_{in} as well as the Z_0 have to be stable against manufacturing errors. A first analysis of the Z_0 stability of both RW and ML technology against manufacturing errors of typically $\pm$ 0.1 mm (a typical error case on a plastic injection molding process) is carried out. In Table 2.1 the stability of the characteristic impedance of the transmission line is shown as $|\frac{Z_0 - Z_{nom}}{Z_{nom}}|$, where Z_{nom} is the nominal characteristic impendace. By introducing dimensional errors of $\pm$ 0.1 mm, we can see that the characteristic impedance in RW technology is much more robust than in ML technology.
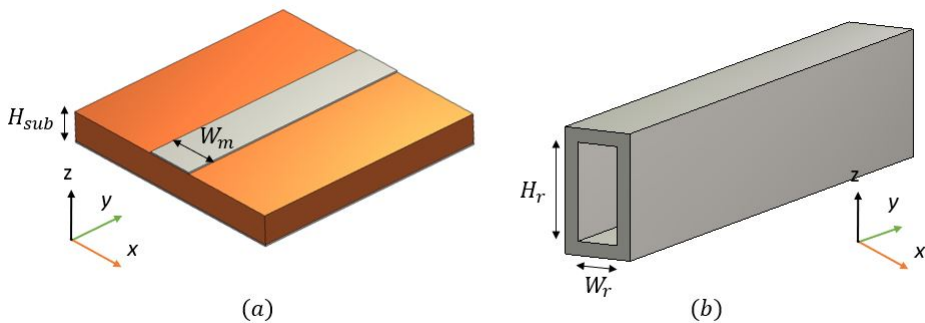

Figure 2.1: Microstrip Line Technology in the left (a) and Rectangular Waveguide Technology in the right (b)

Table 2.1: Stability analysis of the characteristic impedance Z_0 for both ML and RW technologies. The relative error is $|\frac{Z_0 - Z_{nom}}{Z_{nom}}|$ where Z_{nom} is the nominal value of the characteristic impedance of the transmission line without inserting tolerance errors of ± 0.1 mm, that are 50 and 450 for the ML and RW respectively

Parameter	Dimension (mm)	Relative Error (%)
Microstrip Line		
W_m	1 ± 0.1	7.2
H_{sub}	0.5 ± 0.1	13
Rectangular Waveguide		
W_r	1.47 ± 0.1	0.001
H_r	3.5 ± 0.1	1.5

Although the input impedance Z_{in} will really depend on the shape of the used antenna, which is different for each design, it is not direct to say whether Z_{in} will be more robust in RW too. Usually, a higher bandwidth antenna will provide higher chances for a proper impedance matching in the whole band of operation. Which is in other words, that the Z_{in} will be more stable. More details can be found in the paper [**IZ-I**], by using the same antenna shape, with an equivalent inverted ML solution in RW, it is concluded that TE_{10} mode structures (RW) are much more stable than a Q_{TEM} mode structures.

Fast prototyping of RW's needs to be manufactured on separate pieces, requiring perfect sealing when unifying them in order to avoid leakage [19].
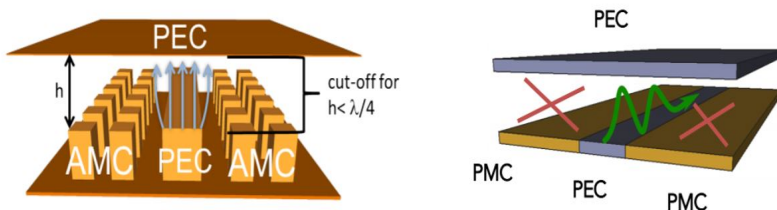
Figure 2.2: Gapwaveguide AMC cut-off boundary condition

In this context, Gap-Waveguide (GW) has attracted attention during the last decade, and the invention by S. Kildal offers a contactless full metal two parallel plates guiding structure solution by using an artificial magnetic conductor (AMC) at both sides of the transmission line, see Figure 2.2, so all the electromagnetic energy is confined by the parallel plates and the AMC [20]. The AMC can be achieved by rows of periodic nails, although other conformations can be adopted such as mushrooms type [21], with the only condition that the space between the AMC and the parallel plate is smaller than $\lambda_g/4$. Clearly, in this configuration, there is no need for an electrical connection between the top and bottom conductive planes of the RW, leading to a

low loss and relatively easy manufacturing process, such as plastic injection molding.

In order to benefit from the advantages of the GW technology, different designs have been reported in the literature, which can be classified into two main groups, Ridge Gap-Waveguide (RGW) [22] which is the most popular design owing to its analogy to the ML but in an inverted form and groove Gap-waveguide (GGW) [23] with a working principle similar to that of RW. There are two subgroups of GGW technology: named H-GGW and V-GGW, that are similar to an horizontal RW (HRW) and a vertical RW (VRW) respectively. Regarding vertically oriented waveguides V-GGW/VRW, they offer more compactness in the antenna plane because the slots are excited on the narrow wall of the transmission line. All these previous classifications are summarized in Figure 2.3. Some designs using these technologies for automotive radars have been made on H-GGW [24] but the size is too long in the transversal direction of the array. Some works exciting vertically oriented waveguides (VGGW/VRW) can be mainly found in VRW by implementing slots. However, the slots must be excited using a tilt angle as currents are in counter phase every $\lambda_g/2$ [25],[26] , which is highly undesirable as cross polarization (CPol) appears. Many studies have been conducted in order to make these elements radiate in phase while maintaining low levels of CPol by using parasitic elements inside the waveguide to modify the current distribution [27]; however, a very demanding manufacturing precision is required and they are bandwidth limited. Only a few works have been published to solve these problems of slot excitation using V-GGW, in [28] parasitic dipole elements are used in the upper layer by means of an extra layer of substrate; however, it only shows 2% fractional bandwidth (FBW) which is not enough for automotive applications.

A single series fed slotted array in V-GGW working in the automotive W-band of 76-81GHz is proposed in this work [**IZ-I**], although RGW can offer a much simple and direct solution, it is shown that it is not that stable, check Table 2 from the paper

[IZ-I].

Table 2.2: Comparison with other similar works. The minimum separation parameter from the fifth column is the minimum inter-array separation achievable of the design, η is the measured efficiency.

Ref.	Tech.	CPol	FBW (%)	Min. separation (λ)	Thickness (λ)	η
Series fed Solutions						
[29]	ML	No	7	0.55	0.03	39
[30]	HRW	No	6.2	1.3	0.7	90.2
[25]	VRW	Yes	2.1	0.5	0.7	NA
[26]	VRW	Yes	9	0.5	0.7	80
[27]	VRW	No	6.4	0.29	0.61	NA
[24]	H-GGW	No	2.8	1.32	0.33	93
[28]	V-GGW	No	2	0.57	0.75	NA
[31]	RGW	No	14.4	0.65	0.7	NA
[32]	RGW	No	3.8	0.49	0.165	NA
This work	V-GGW	No	9	0.57	1.91	92.2

In comparison to the antennas presented in the literature (see Table 2.2), we propose a new method for exciting narrow wall slots from V-GGW without added manufacturing complexity and a good fabrication tolerance stability of up to 0.1 mm (corresponding to the tolerances of a conventional manufacturing technique). The antenna consists of a triple-layer structure with a novel aperture coupling mechanism offering a linearly polarized, high efficiency (92.2%) with a high measured FBW (9%) while being compact in the transversal direction.

2.2   Antenna Design

The slot elements from a series fed design in the narrow wall of vertically oriented waveguide-related technologies cannot be directly excited as stated in the introduction. An isometric and top view of the proposed unit array antenna for this study with $0.5\lambda_g$ radiating slots in V-GGW technology can be seen in Figures. 2.4 and 2.5 respectively.
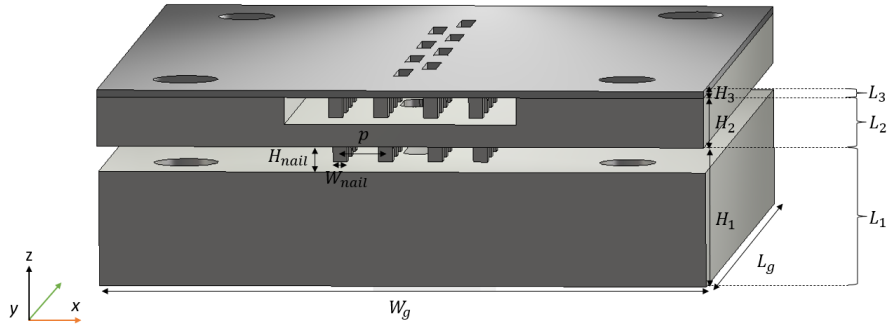
Figure 2.4: Isometric View. Bottom layer L_1, middle layer L_2 and top layer L_3

The V-GGW antenna is mainly composed of three layers: the feeding layer (bottom) L_1, coupling layer (middle) L_2 and radiating layer (top) L_3, whose dimensions are listed in Table 2.3. All the energy from the guiding groove line from the bottom layer propagates through four slots (W_{Lslot} x L_{Lslot}) from the middle layer L_2. These slots are approximately spaced λ_g from each other so they radiate in phase and each one of them, excites two of the eight $\lambda_g/2$ spaced slots of (W_{USlot} x L_{USlot}) from the top layer L_3. In this manner, all the slots radiate in phase with no grating lobes or high CPol level problems. For a more detailed explanation, please refer to the paper [**IZ-I**].
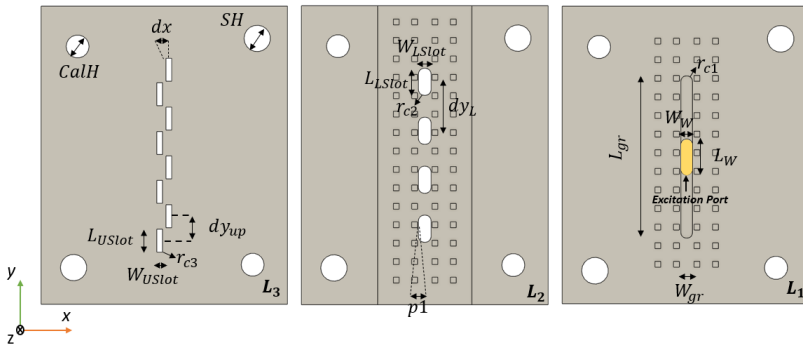
Figure 2.5: Top View of the three different layers. In yellow it is highlighted the input excitation port to the antenna prototype and r_{c1}, r_{c2}, r_{c3} represent the radius of curvature of the flagged edges.

2.2.1 Tolerance Analysis

The massive deployment of antennas requires an important analysis of the manufacturing tolerances. In order to ensure a good radiation performance for N antennas

Table 2.3: Summary of the main antenna dimensions and the deviations in the fabricated one in mm. The errors for the case of the slots and nails are the maximum errors. Parameters marked with at least one * are used for the tolerance analysis from section III.

Param.	Nom. (mm)	Error (mm)	Param.	Nom. (mm)	Error (mm)
Layer 1			**Layer 2**		
$H_{gr}*$	2.7	0.02	$L_{Lslot}**$	2.35	0.07
$L_{gr}*$	13.95	0.08	$W_{Lslot}*$	1.1	0.11
$W_{gr}*$	1	0	dY_L*	4.25	0.05
L_W*	3.1	0.05	r_{c2}	0.5	-
W_W*	1	0.12	$H_{t1}*$	0.4	0.09
H_W	1.35	-	$L_{t1}*$	1.55	-0.15
r_{c1}	0.5	-	$H_{t2}*$	0.35	0.12
H_1*	5	0.03	$L_{t2}*$	1	-0.17
			$W_{t1}*$	1.1	0
			$W_{t2}*$	1.1	0
Layer 3			H_2*	1.75	-0.04
$L_{USlot}**$	2	0.03	**AMC**		
$W_{USlot}*$	0.5	-0.01			
$dY_{up}**$	2.25	0.01	p *	0.88	0.03
$DispX3*$	0	0.15	$W_{nail}**$	0.5	0.07
$DispY3*$	0	-0.10	$H_{nail}*$	0.95	0.01
dx*	0.4	0	p1**	0.1	0.05
r_{c3}	0.025	-	H_3*	0.25	0

with fabrication tolerances of up to 0.1mm (which is a standard manufacturing tolerance for many industrial technologies) at high frequencies is one of the main challenges that this paper has focused on. There are 31 dimensional parameters for the case of V-GGW, assuming a uniform error distribution with only three discrete values of $-0.1, 0$ and $+0.1$ mm, for every single parameter this would result in a total amount of 1.59 million and over trillions of combined errors respectively, which is obviously not feasible to simulate. A first analysis of the critical dimensions was carried out to reduce this space of combinations. Errors of $\pm$ 0.1 mm were applied to each parameter separately, resulting in 54 input reflection coefficients, the parameters used in this first study are marked with at least one * in Table 2.3 respectively. Parameters from

the Table 2.3 marked with a double * are the most critical ones in terms of reflection coefficients seen at Figure 2.6 (a), resulting in a penalty of greater than 15% of FBW reduction if taking into account that the only valid bands are those marked by the input reflection coefficient when using nominal dimensions.

(a) Independent Errors **(b)** Combined Errors
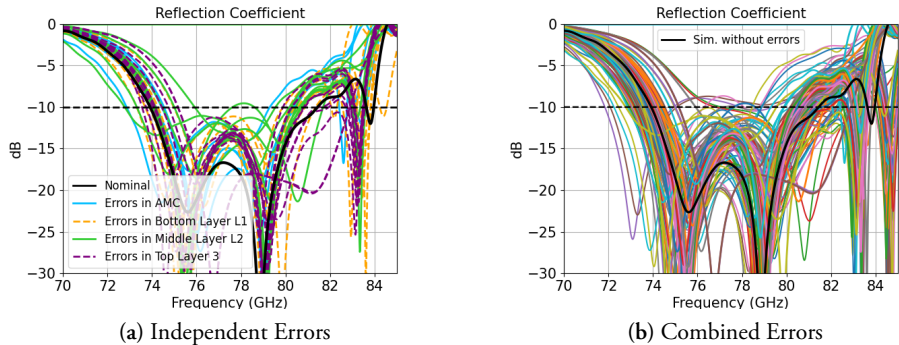
Figure 2.6: Simulated Input reflection coefficients (a) by adding independently +0.1 mm and -0.1 mm of errors (54 in total) to each dimensional parameter while keeping the rest ones in nominal dimension and (b) for the main combination of errors (243 in total) in color. The black trace corresponds to the simulated antenna with nominal dimensions.

The critical parameters are the length of the slots from each layer L_{Lslot} and L_{USlot}, W_{nail} and $p1$. Only these parameters are selected for the final study using combined errors and are plotted in Figures 2.6 (b) and 2.7. For the case of the input reflection coefficients in this V-GGW design, 89% of the combined errors guarantee a frequency range from $74.25GHz$ to $80GHz$, resulting in a 7.5% secured FBW. Note that the higher the FBW, the higher chance to guarantee a good matching against manufacturing errors in the frequency band of interest.

(a) V-GGW H-plane   (b) V-GGW E-plane
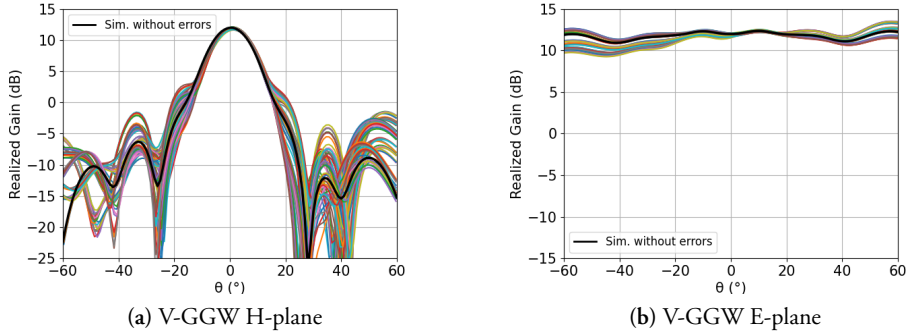
Figure 2.7: V-GGW design radiation pattern cuts for the main combination of errors in color, - corresponds to the simulated antenna with nominal dimensions.

Only pattern stability for the design in V-GGW is represented in Figure 2.7 because the results are well-matched, showing good pointing stability as well as realized gain. An increase of up to 7.5dB in SLL was due to the errors related to the slot spacing dY_{up} from the top layer L_3. Of course, if considering misalignment errors between each layer, we will have a worse response in terms of SLL although it has almost no impact on the input reflection coefficients.

2.3 Experimental Validation

The fabricated dimensional errors of the antenna are listed in Table 2.3, which were measured using the Nikon Measurescope MM-11 with a precision of 10um. The most deviated errors were caused by the displacement of the $L3$ layer ($DispX3$ and $DispY3$), the connection of the WR10 (W_W) to the waveguide structure, the width of the slots W_{Lslot} of $L2$ and dimensions (height x length) of the stepped matching element (H_{t1} x L_{t1}) and (H_{t2} x L_{t2}) with a deviation up to 0.15 mm.
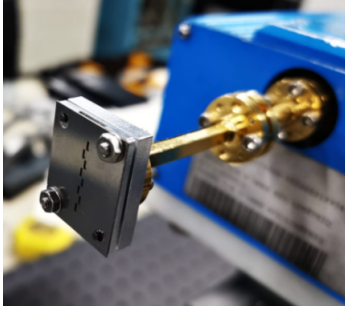
(a) Manufactured antenna at the head of the PNA N5222A Network Analyze
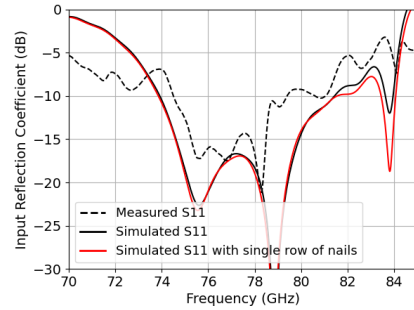
(b) Measured Input reflection coefficients of the antenna

Figure 2.8: Input reflection coefficients of the antenna. In black a double row of nails for the AMC is used and in red color corresponds to the simulated antenna by just using only one row of nails to show that it can be compact in the transversal direction of the array. Discontinuous lines (- -) are the measured results while continuous lines (-) are simulated results.

The measurements and simulations using CST Studio software included the reflection coefficients and realized gain patterns, which were cut at 77 GHz, and are shown in Figures 2.8 and 2.9.

A good matching of the antenna was achieved which ranges from 74.5GHz to 81GHz. A realized gain of 12.15 dB was measured which also showed good agreement with the simulations for both planes at 77GHz. A simulated SLL of -18.5dB in H-plane was increased up to -16.5 dB at θ = -28 deg in the measurements caused by the misalignment of the radiating layer l_3 with respect to the other two ones, leading to a non-perfect symmetrical field distribution among the radiating slots.
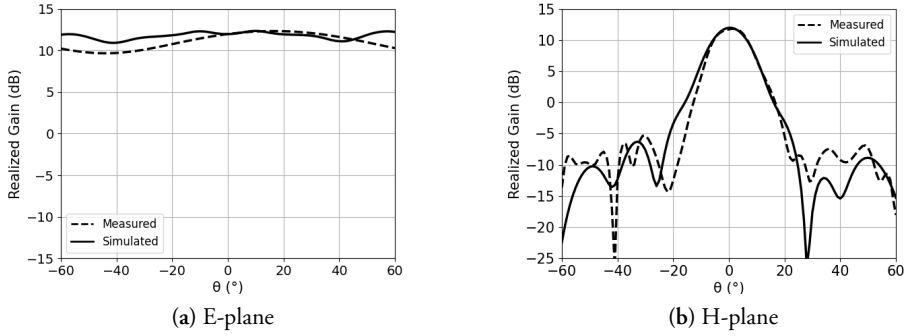
(a) E-plane

(b) H-plane

Figure 2.9: Radiation pattern cuts at E-plane (a) and H-plane (b), - corresponds to the simulated antenna, and - - corresponds to the actual measured prototype.

2.4 Conclusions

The robustness of TE_{10} mode guiding structures such as RW or V-GGW/H-GGW against manufacturing errors of $\pm$ 0.1mm are more stable than those ones found in Q-TEM mode structures such as RGW and ML. This is also reflected in the input reflection coefficient of an antenna using those technologies.

After this finding, GW solutions (RGW, V-GGW and H-GGW) were explored because of its high manufacturing potential when compared to RW, because they can be assembled in two different pieces without requiring direct contact among them. V-GGW technology was finally selected because it shows more compactness than H-GGW and offers a much higher characteristic impedance stability (TE_{10} mode) than RGW (Q-TEM mode). A triple layer V-GGW series fed slotted antenna was designed, manufactured and validated at the UPC anechoic chamber, showing great results even with a lot of manufacturing errors.

Although the antenna was not plastic manufactured because of the limitations of our resources, it offers a high tolerance stability, it is shown that for the main combination of critical simulated errors they all offer S_{11}< -10dB in the whole 76GHz-81GHz band which makes this antenna a very good candidate to be manufactured using plastic injection molding and mass produced. This can also be used to conclude that the higher the FBW, the better the input reflection coefficient against manufacturing errors.

Future works may be exploring curved solutions with this type of antenna in order to integrate it behind the aesthetics of a car.

Chapter 3

Antenna Integration to Chip

3.1 Introduction

In conventional automotive radars, the antennas are usually connected to a chip where all the transmission, reception and post-processing of the electromagnetic signal is performed. Chips at these high frequencies of 76-81GHz make Microstrip-Line (ML) based circuitry the optimum solution for this interconnection. In the previous chapter, it was shown that antennas in Rectangular-Waveguide (RW) (same propagation mode as in Groove Gap-Waveguide (GGW) can offer higher radiation performance and plastic prototyping potential, with much greater advantages than those ones in ML. Even if we implement RW antennas, we have to end up using a RW-ML transition (also known as RW launchers) [33,34], see Figure 5.1.
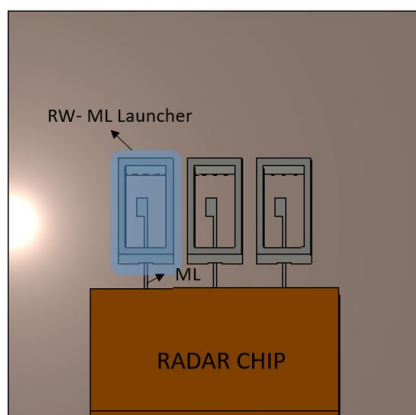
Figure 3.1: Three conventional RW launchers connected to the radar chipset via ML

There are still two main advantages; first we reduce the area of substrate used, which is a reduction of the cost with a high budget impact when mass produced; second we avoid large distribution networks in ML, which is a reduction of the losses in the antenna.

There are two main type of RW-ML transitions: bottom-side (BS) [35,36], and top-side (TS) [37,38,39,40,41]. In the case of TS, the ML and the RW are on the same face of the substrate, whereas for the BS the ML and the RW are on opposite faces, which may be necessary depending on the design requirements.

In [36], a BS transition was proposed via proximity coupling through a patch antenna, although it offers 18% of fractional bandwidth (FBW), it requires perpendicular input/output ports from the large wall of the RW, which makes the design bulkier. In [39], this large wall is avoided with a narrow-wall design consisting of a V-shaped aperture coupled patch; however, only 7.5% of FBW is achieved. TS RW to ML transitions are also explored as in [40], where the RW is excited through a transversal patch antenna coming from the narrow wall; however, intrusion elements inside the RW have to be carefully inserted in order to enhance the FBW from 11% to 15%, which increases the fabrication complexity. This intrusion element is avoided in [41] through a patch fed by a coupled ML, but only 11% of FBW is achieved.

In comparison with the transitions presented in this work, a narrow-wall ML-RW transition is designed and validated using a manufactured back-to-back (B2B) configuration that can work for both TS and BS at the same time without increased manufacturing complexity. The transition consists of a ML that feeds an array of three overlapped transversal patches from the narrow wall of the RW, offering a much higher bandwidth when compared to similar presented work. The design shows a FBW of 21.2% for the TS design and 23% for the BS design, which is much larger than the other presented works.

Table 3.1: Similar works that can be found showing the comparison of B2B parameters like minimum IL, maximum IL, FBW and the operating band.

Work	Type	Wall	Max IL	FBW	Band	Backshort
[36]	BS	Broad	NA	18%	W	No
[39]	BS	Narrow	0.7dB	7.5%	W	No
This Work BS	BS	Narrow	0.85 dB	23%	LMDS, Ka	No
[40] (A)	TS	Narrow	1dB	15%	W	No
[40] (B)	TS	Narrow	1.1dB	11%	W	No
[41]	TS	Narrow	NA	11%	W	No
This Work TS	TS	Narrow	0.67 dB	21.2%	LMDS, Ka	No

3.2 Transition Design

The focus of this first section consists of the conversion of the Q-TEM mode of a 50 Ω ML [42] to the TE01 mode of a WR-34 ($W_{rw} \times L_{rw}$) [43] for both TS and BS. A more detailed description of the working principle will be given for the case of the TS transition, the BS uses the same working principle by just adding a metallic bias to connect the TS ML with the BS ML. Because of the manufacturing limitations in the laboratories from the UPC, the design was first validated in a lower frequency band, the LMDS and K bands (24.25GHz-29.5GHz).

Figure 3.2 a shows the isometric view of the transition, and Figure 3.2 b shows its top and bottom view. The transition is designed using a 0.81 mm thick RO4003 substrate with a dielectric constant of Er = 3.55 and a loss tangent of 0.002. In order to excite the TE01 mode from the waveguide, excitation of transversal currents in the $\hat{x}$ direction is needed. A simple and direct ML-RW mode conversion can be found in [40]. By using a single transversal patch with an approximate length of $\frac{1}{2}\lambda_g$, radiation with the proper polarization is achieved to excite the TE01 mode from the RW. However, it is bandwidth limited. As a way to enhance this bandwidth, an array of three overlapped transversal patches is proposed in this chapter, the length Lp of the patches, the width W_p, inter-element distance d_y and array position with respect to the entrance of the RW y_0 are jointly optimized to provide maximum bandwidth.
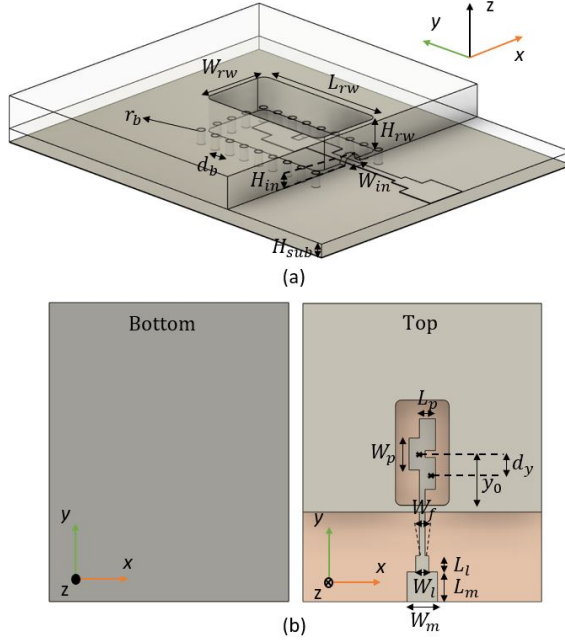
Figure 3.2: Artist view of the Top-Side transition for **(a)** isometric view and **(b)** top and bottom view.

Table 3.2: Dimensions in mm of each designed parameter for the top-side transition

| H_{sub}	0.81	W_f	0.47	W_{rw}	4.5
dy	1.625	W_l	1.1	L_{rw}	8.8
W_p	2.67	L_l	1.35	H_{rw}	2
L_p	1.35	L_m	2.5	H_{in}	0.5
Y_0	4.3	W_m	2.55	W_{in}	1.2
r_b	0.25	d_b	1.17		

The overlapped patches offer an intrinsic higher bandwidth behaviour when compared to a single patch element. The array is fed by a ML of width W_f, and it is matched to a 50 Ω circuit with a stepped section of $W_t \times L_t$. The entrance to the RW has dimensions ($Win \times Hin$), it should ideally be as little as possible to avoid leakage from the RW but not short-circuiting with the ML; however, a considerable dimension was chosen to be manufacturable. There are via holes of radius r_b and periodicity d_b surrounding the aperture of the RW that connects the RW to the ground plane of the substrate; by reducing this periodicity, the insertion losses are not reduced.

The working principle of the BS transition is the same as the TS transition. The parameters are not exactly the same, as they were slightly re-optimized for this BS case, see Table 3.3. Figure 3.3 shows the top view, bottom view, and isometric view of this transition. The entrance of the ML along the bottom side is achieved by leaving a

Table 3.3: Dimensions in mm of each designed parameter for the bottom-side transition

H_{sub}	0.81	W_f	0.44	W_m	2.55	Y_0	4.4
dy	1.73	W_l	1.45	L_m	2.5	r_b	0.25
W_p	2.77	L_l	1.2	H_{rw}	2	W_{rw}	4.5
L_p	1.33	d_b	1.17	C	0.15	L_{rw}	8.8
E_x	1.58						

U-slot of width c around the ground. By adding a bias of radius r_b at the edge of this ML, we can connect and feed the overlapped patches from the other side, the TS. The ground plane has an extension of E_x with respect to the narrow wall RW. The via holes also have to be extended to the end of this ground plane, otherwise leakage through $\hat{x}$ direction will appear due to the currents excited by the U-slot.
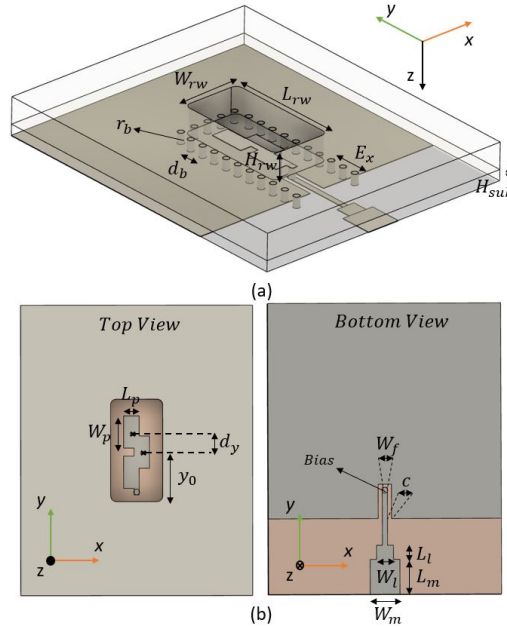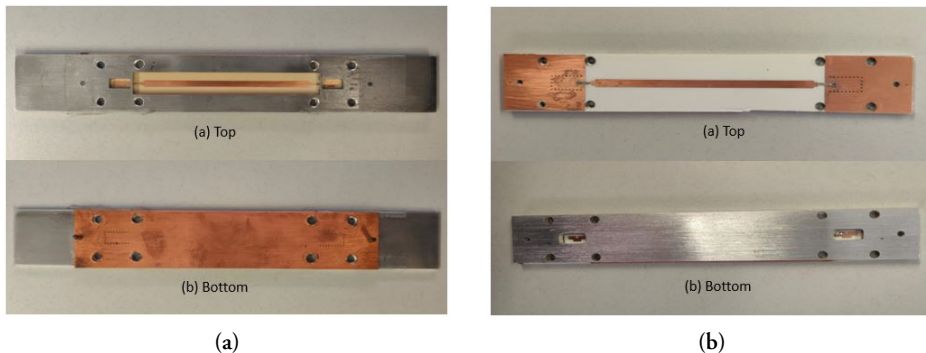

Figure 3.3: Artist view of the Bottom-Side transition for **(a)** isometric view and **(b)** top and bottom view.

This type of BS transition has an advantage with respect to the TS transitions involving interference reduction, as the RF-chipset may be located at the opposite face from the radiating elements. However, it comes with many disadvantages, as will be seen in the next section.

3.3 Main Results

A B2B transition was designed and manufactured at the UPC facilities for both TS and BS designs. The PCB was fabricated using the standard photolithography technique, and the RW assembly connection was manufactured using a CNC milling machine (see Figure 3.4 a and 3.4) b). The two designs were measured with the vector network analyzer ZNB-40 from Rohde-Schwarz.

In Figure 3.5a and 3.5b, the 73 mm long B2B input reflection coefficient and insertion loss (IL) from both simulations and measurements are shown for TS and BS designs, respectively. There is a good correlation between the simulations and measurements; for the case of TS transition the design offers a measured −10 dB bandwidth ranging from 24.25 GHz to 30 GHz (FBW of 21.2%) with a little portion of mismatched band ranging from 26.35 GHz to 26.65 GHz at just −9.5 dB and a maximum B2B IL of 1.35 dB, which is 0.67 dB (half) for a single transition. Note that the IL does not take into account the propagation losses (1.3 dB for the 73 mm long ML), as it was already taken away from both simulation and measurement plots. This portion of slightly mismatched frequencies is due to a positional error of the holes that are used to attach the WR-34 to the transition; obviously, the results would be much better if, instead of a B2B transition, a direct single ML-RW transition was used to be measured.

Figure 3.4: Top view and bottom view of the B2B manufactured TS transition (a) and BS transition (b).
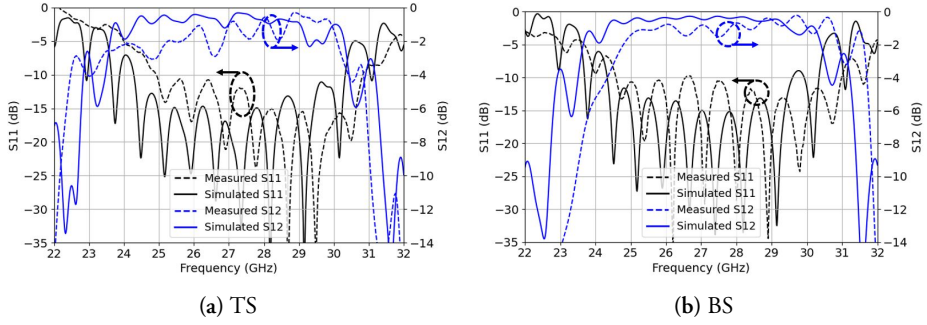
Figure 3.5: Top-side back-to-back (a) and Bottom-side back-to-back (b) S11 reflection coefficients (left y-axis) in black and insertion losses S12 (right y-axis) in blue for the measurements and simulations

For the case of BS transition, the design offers a measured −10 dB bandwidth ranging from 24.6 GHz to 31 GHz (FBW of 23%) and a maximum IL of 1.7 dB, which is 0.85 dB for a single transition. This IL is worse than the simulated one because of slight manufacturing errors, as seen in the previous section, BS is less robust than TS.

Clearly, the TS offers much better and stable IL along the frequency band of operation. Although for both cases there is a small portion of slightly mismatched frequencies around the central frequency point, the TS design is a preferred option in terms of IL, simpler manufacturing process, and robustness to fabrication errors.

3.4 Conclusions

A novel RW to ML transition using an array of three overlapped patches has been designed and validated at the whole LMDS and K-band, but it can be perfectly scaled up in frequency up to the 76-81GHz band without many problems. Two designs were designed and manufactured using the same principle for both TS and BS integration. The TS B2B transition offers a measured 21.2% of FBW with a maximum single transition IL of up to 0.67dB. The BS B2B transition offers 23% of FBW with a maximum single transition IL of up to 0.85dB. Both TS and BS transitions offers a similar input reflection coefficient, but a higher radiation leakage is found for the BS (2.7dB more).

The transition is designed and validated at the whole LMDS and K-band but it can be perfectly scaled up in frequency up to the 76-81GHz band, for the case of the TS transition there is an optimized geometry for the RO4003 substrate of 0.305mm thick at W-Band, for the dimensions see Table 3.4 and for the simulated results see Figure 3.6.

Table 3.4: Dimensions in mm of each designed parameter for the top-side transition scaled up to W-Band

H_{sub}	0.305	W_f	0.13	W_{rw}	1.46
dy	0.61	W_l	0.4	L_{rw}	3
W_p	0.68	L_l	0.67	H_{rw}	2
L_p	0.4	L_m	1	H_{in}	0.2
Y_0	1.67	W_m	0.69	W_{in}	0.5
r_b	0.25	d_b	0.4		
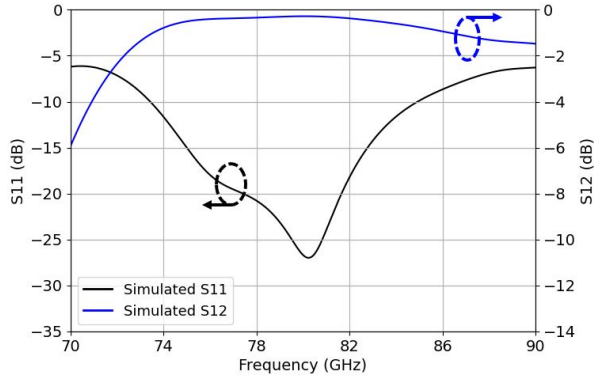
Figure 3.6: Simulated S-Parameters for the top-side transition at 77GHz

The transition can be used as a chip TE_{10} mode launcher for feeding RW/GW antennas.

Chapter 4

Plastic Printed Prototype

4.1 Introduction

A plastic Rectangular-Waveguide (RW) antenna prototype with a transition from RW to Microstrip-Line (ML) is presented in this chapter to show the industrialization viability of the studied technology. At this stage of the thesis, we just realized that horn antennas have a much higher potential for automotive radar sensors, the aperture can be just enlarged in the H-plane offering a similar radiation pattern as required by commercial radar sensor antennas, the gain can be controlled by adjusting this aperture dimension, it is not resonant so the manufacturing errors won't affect the S_{11} parameters making them a perfect robust candidate for mass production using plastic technology.

With respect to other 3D printed horn antennas, in [44] a fully 3D printed complex corporate feeding network with 256 horns was successfully manufactured. However, it was done by using direct metal laser sintering DMLS technique, which is an expensive option. 3D printed horns with conventional copper electrodeposition as a metallization method like in [45] is a well-known and cost-effective option. However, transitions from the horn RW to ML are usually required to provide an effective connection with the RF chipset which is not yet reported in any research.

The TS transition from previous section is integrated in (and used to validate) a 3D printed phased array (PA) of H-sectorial horns with reduced blind scanning and a simple metallization procedure, making the PA ready to be integrated with any RF-chipset. In this case, the design was performed at the LMDS and K bands because of the working band of the used RF-chipset. The measured results prove the feasibility of the 3D printing technology for manufacturing complex active antenna systems like

PA's, which is similar to a radar.

4.2   Phased Array Design

In Fig. 4.1 an exploded view of the whole microstrip fed 3D printed PA of four active H-Sectorial horns is shown. The antenna was designed to be attached through four 2.4mm coaxial cables to the F5288 digital beamformer from RENESAS, achieving four active channels.
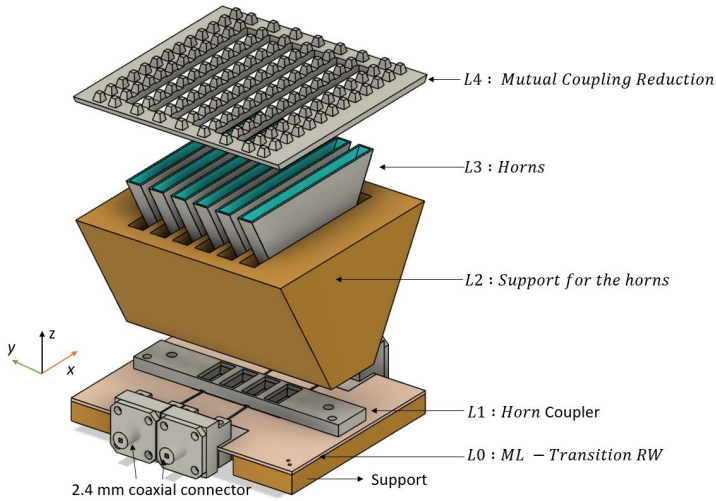

Figure 4.1: Exploded View of the whole design

It is composed of five different layers, $L0$, $L1$, $L2$, $L3$ and $L4$. The first layer $L0$ consists of four 2.4mm female connectors attached to the ML printed on the RO4003C substrate, that are used to feed the ML-RW transition presented in section II. Layer L1 is a horn coupler that attaches layer L0 to layer L2. In turn, L2 is a support for six H-sectorial horns, implemented on layer L3, through two M2.5 screwed holes. Although a direct chip to ML integration would be a more elegant option to reduce design complexity, bulkiness as well as cable losses, it is not the main goal of this research but to demonstrate the feasibility of 3D printing technology for manufacturing complex antenna systems like PA's.

Only four horns are active, being the two lateral ones dummies placed in both sides of the phased array in order to symmetrize the radiation pattern. The top $L4$ layer consists of an arrangement of periodical nails to reduce the mutual coupling (MC) between each horn antenna. Thus the blind scanning issue is minimized, maintaining

a -10dB matching of all the four active horns for a wide range of scanning angles related to a progressive phase ranging from 0° to 140°. The support, $L1$, $L2$, $L3$ and $L4$ were fully 3D printed with the printer Objet Connex 1 from Stratasys using material jetting technique. The used photosensitive resin ink was RGD525 High Temp with an electrical permitivitty of E_r = 2.95 and a loss tangent of 0.0175. All the printed materials except $L2$ are metallized using copper electrodeposition.

Six H-sectorial horns were designed and 3D printed, with dimensions shown in Fig. 4.2. The horns have height L_h, width W_h and thickness W_y. The entrance of the horn has width X_W and height X_h which was optimized in order to maximize the bandwidth of the joint horn and transition design. The inner side of the horn is empty in order to reduce the transmission losses of the EM fields, the thickness of the walls of each horn is constant of value W_{wall}.
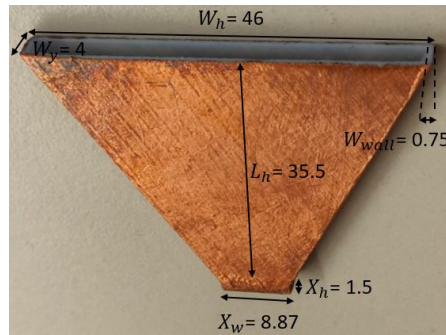

Figure 4.2: Horn Antenna (all dimensions in mm)

Only the outer lateral parts of the horn were metallized, which is a much simpler way to guarantee a complete surface deposition of the copper than metallizing both outer and inner parts as it is usually done.

A layer of mutual coupling reduction $L4$ was designed in order to reduce the well known blind scanning problem [46] of phased arrays. This layer consists in using periodic nails p_{ycorr} of trapezoidal shape with squared bottom shape W_{Anail} x W_{Anail} and top W_{Bnail} x W_{Bnail} of height H_{nail}. The periodic nails, also known as high impedance surfaces are a preferred option when compared to $\lambda_g/4$ slits because of its intrinsic wide-band behaviour.
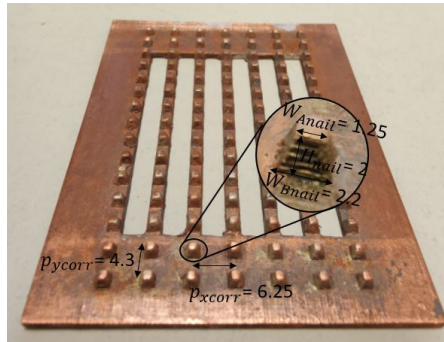
Figure 4.3: $L4$ Layer showing the corrugations used for blind scanning reduction of a phased array
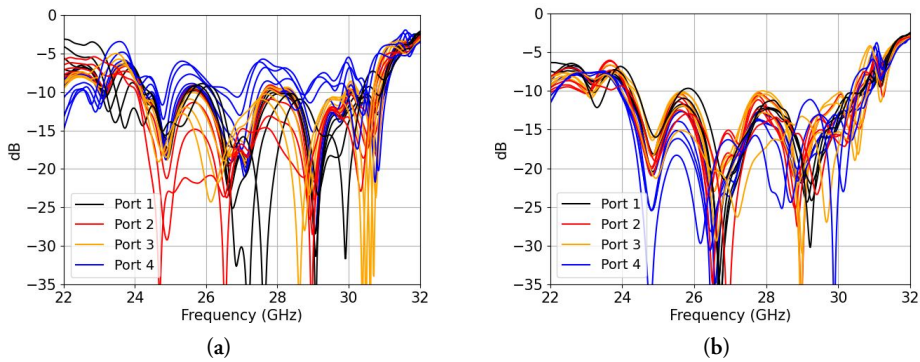
Figure 4.4: Simulated input reflection coefficients for each port (a) without nails (b) with nails. There are 6 traces per port belonging to the progressive phase from 0° to 140° at 26.5GHz

In order to find the optimal parameters to reduce the blind scanning problem, the MC between adjacent horns has to be reduced. By just selecting two horns, each one with a simulation port, it is possible to optimize its dimensions by finding the minimum coupling between them. In Fig.4.4 we can see the comparison of the input reflection coefficients between (a) without the nails and (b) with nails. For each port of the horn there are 6 traces belonging to the progressive phase from 0° to 140° at 26.5GHz. We can clearly see that port 4 becomes mismatched when a progressive phase along the arrays differs from 0, which will clearly reduce the gain of the beamformer.

4.3   Main Results
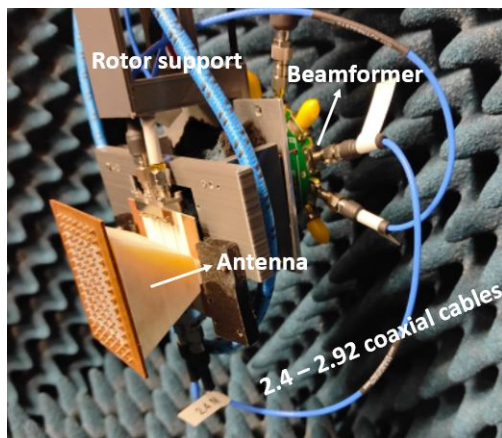
Figure 4.5: Entire manufactured phased array connected with the beamformer and ready to be measured in the anechoic chamber

This section shows the experimental results of the designed PA. Fig. 4.5 shows the manufactured and mounted PA connected to the beamformer, Fig. 4.6 shows the results of the input reflection coefficients, Fig. 4.7 the scanning pattern of the phased array in dB. In Fig. 4.6, the input reflection coefficients corresponds to each single port (when measuring one port the rest remain unexcited). Note that measuring the input reflection coefficient of each port when exciting all ports and using the beamformer for scanning in the E-plane, was not possible with the setup. The measured input reflection coefficients are all slightly shifted up in frequency with a wider bandwidth behaviour, with an unexpected resonance at 31.25GHz. Only the radiation pattern in E-Plane was measured for each scanning angle using the digital beamformer at four different frequencies ranging only from 26.5GHz to 29.5 GHz because this beamformer chip is limited to operate only in the LMDS band. Each channel of the beamformer was calibrated as each cable's curvature introduce different phases.
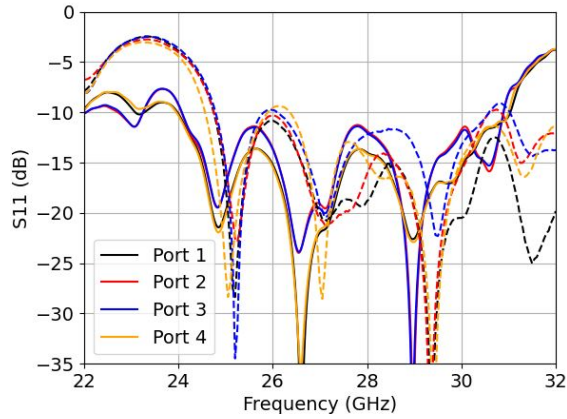
Figure 4.6: Input reflection coefficient (for measured - - and simulated -) for each port independently
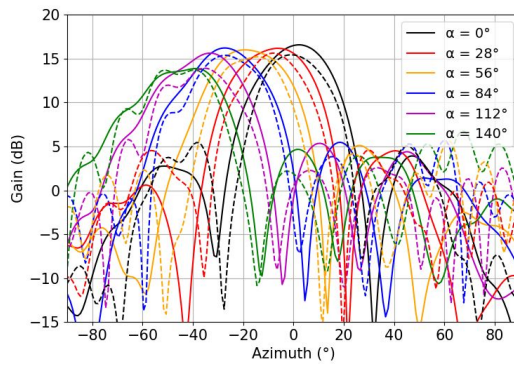
Figure 4.7: Radiation pattern in the E-plane (for measured - - and simulated -) for six different progressive phases α ranging from 0° to 140 ° at 26.5GHz.

The gain of the phased array was referenced to the measurement of a 20.8dB gain horn antenna connected to one channel of the beamformer. The maximum amount of Sidelobe Level (SLL) was measured to be 12dB for a progressive phase of 140°, which can be reduced because a uniform distribution among the channels was used along the array.

4.4 Conclusions

A 3D printed phased array of four H-sectorial horns with minimized blind scanning problem and easier to be metallized procedure has been proposed as a possible solution

for automotive radars. The antenna is non-resonant, highly integrable into RF-chips and can be manufactured using plastic technology.

A ML to RW transition has been designed for the integration of the phased array with a commercial digital beamformer in order to validate its functionality. The 3D printed phased array was used to scan from 0° to 140° at the central frequency 26.5GHz in steps of 28°, totalling an amount of 6 patterns. The measured gain of the array was 15.2dB for the case of the broadside direction and a measured FBW of 20.8% for the case of single port measurement. The results proof the feasibility of 3D printing technology for the manufacturing complex antenna systems like PA's in this case in high frequency bands and its easy integration with RF-chips. A future improvement would be to integrate the antenna directly with the beamforming chip to avoid the use of coaxial interconnections which introduce additional losses and scale it up to W-band.

Chapter 5

Radome Integration

5.1 Introduction

ADAS sensors have to be integrated in the aesthetics of a car, such as Long range radars (LRR) (76GHz-77GHz), Short range radars (SRR) (77GHz-81GHz), ultrasonic sensors, LiDARS and cameras to keep the car's aesthetics without loosing sensing capabilities.
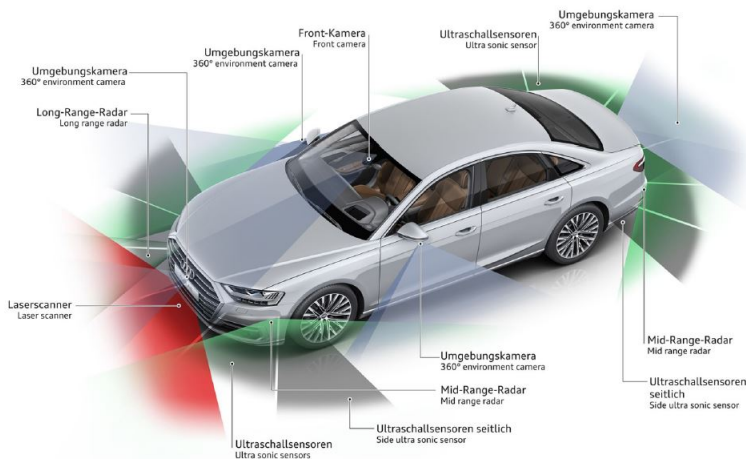
Figure 5.1: Audi A8 implementing different types of sensors such as LRR radars, SRR radars, ultrasonic sensors, LiDARS and cameras installed in different parts of the vehicle to sense all the surroundings of the vehicles.

As we are focused in radar sensors, it is important to note that LRR are usually in-

tegrated behind the emblem and SRR behind a bumper in the corner of a car. As studied in the first chapter, the importance of the manufacturing tolerances are critical for an antenna design, the same applies for the radomes of a car. A deformed plastic cover may result in a bad target detection and an accident when seen by the radar.

In this chapter, the effects of the plastic cover to a radar are studied by using a ray tracing algorithm called rAIdome, which is much faster than CST (the simulation time is reduced from days to minutes) and can be used to optimize the geometry of a radome or to evaluate it. As the plastic covers are usually deformed with tolerances of up to ± 0.1 mm due to the injection molding process (IMP), it may result in fatal Direction of Arrival (DoA) processing errors and big attenuations, a new software called rACoder was developed along the thesis in order to assemble N (~1000) virtual deformed radomes from a virtual injection molded process. As the simulation time through rAIdome is really fast, we can pass these N virtual deformed radomes from the rACoder module to the rAIdome module and evaluate the scrap. Potentially saving a lot of money to the company as it can be used to prevent and reduce the number of failed pieces of a certain radome design.

5.2 rAIdome Software

rAIdome is a fast and efficient software developed for the evaluation and optimization of the geometry of a radome. The physics used in the software are based on Snell's law using transmission line theory, full derivation of the equations can be found in [47] and summarized in a simple matrix system form in [48] for the case of a single layer:

$$\begin{bmatrix} A & B \\ C & D \end{bmatrix} = \begin{bmatrix} \cos\phi & j\frac{Z}{Z0}\sin\phi \\ j\frac{Z0}{Z}\sin\phi & \cos\phi \end{bmatrix} \tag{5.1}$$

Where the electrical length is $\phi = \frac{2\pi d\sqrt{\epsilon-\sin^2\theta}}{\lambda}$, d is the width of the material, ϵ is the relative permittivity and θ is the angle of incidence of the electromagnetic wave. $\frac{Z}{Z0}$ is the ratio of impedance in the medium to that in free space, and is $\frac{\sqrt{\epsilon-\sin^2\theta}}{\epsilon\cos\theta}$, $\frac{\cos\theta}{\sqrt{\epsilon-\sin^2\theta}}$ for the case of parallel and perpendicular polarization respectively.

The transmission coefficient and reflection coefficient is then :

$$T = \frac{2}{A+B+C+D}, R = \frac{A+B-C-D}{A+B+C+D} \tag{5.2}$$

In the case of a multilayered structure, its derivation is simply the multiplication of the ABCD matrices from each layer :

$$\begin{bmatrix} A & B \\ C & D \end{bmatrix} = [1]\,[2]\,...\,[n]\,layers \tag{5.3}$$

Having the transmission and reflection coefficients, we can discretize the whole aesthetic surface by pieces of dielectric slabs with equivalent widths and normal vectors:
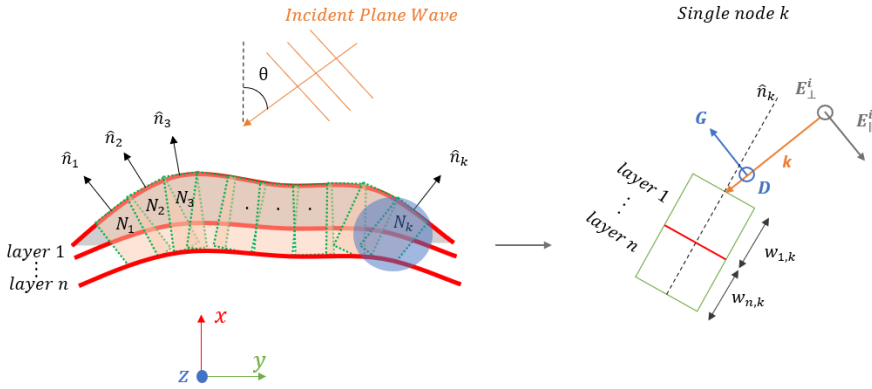
Figure 5.2: The left side of the figure is an example of a multilayered discretized surface by k nodes of n layers. At the right side we have the vectors used for the analysis of the transmittance and reflectance of a single node. The incident electric field is decomposed in a new base formed by the vectors K,D,G, being K the vector of propagation, D the vector tangent to the surface and G the vector perpendicular to K and D.

$$M_{kDG} = [\,k\,,\boldsymbol{D}\,,\boldsymbol{G}\,] \tag{5.4}$$
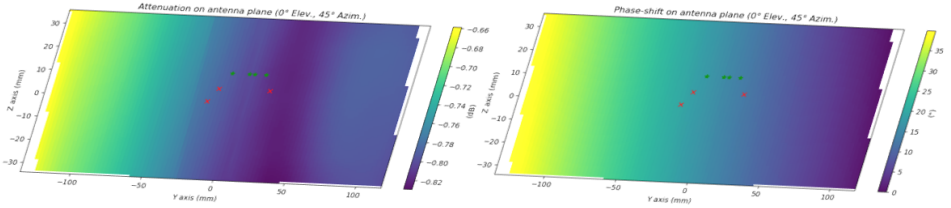
$$\boldsymbol{D} = n\,x\,k \tag{5.5}$$

$$G = D \, x \, k \qquad (5.6)$$

The transmitted field of the Ray after passing the node is simply :

$$\vec{E^t} = M_{kDG} \begin{bmatrix} 1 & 0 & 0 \\ 0 & T_\perp & 0 \\ 0 & 0 & T_\parallel \end{bmatrix} M_{kDG}^T \, \vec{E^i} \qquad (5.7)$$

By tracing rays from each node and projecting them to the plane where the radar is located, we can predict the DoA and attenuation.

Figure 5.3: This figure shows the projected attenuation and phase on the antenna plane for an angle of incidence of azimuth $= 45°$. Red crosses are the location of TX antennas and green crosses represents RX antennas

The signal received by each antenna is just the weighted sum of received rays around its center location, a first approach considering a Gaussian distribution weighting function was assumed, whose standard deviation was adjusted in order to match the effective receiving area of each antenna.

Once we have the signals for each antenna, the two way attenuation is just :

$$Att(Azimuth, elevation) = \frac{1}{n_{RX}} \sum |T(p_{Rx_i})| \frac{1}{n_{TX}} \sum |T(p_{Tx_i})| \qquad (5.8)$$

And the DoA error is, if using linear regression algorithm :

$$\theta = \sin^{-1}\left(\sin\theta - \frac{\lambda}{2\pi}\frac{\delta\angle T'}{\delta d}\right) \qquad (5.9)$$

Other DoA processing algorithms can be used depending on the radar such as Music, Esprit, Capon, Barlett or FFT among others.

Figure 5.4 shows the validations by comparing rAIdome with the CST for three types of different radome designs with different curvatures.
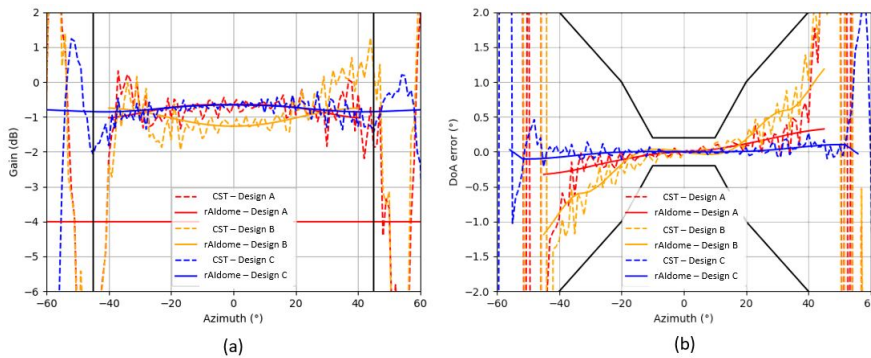
Figure 5.4: Validations by comparing rAIdome (-) with the CST (- -) for three types of different radome designs (A, B and C). (a) shows the gain in (dB) and (b) shows the DoA error.

As we can see, there is a good correlation of the tendency for both DoA error and attenuation with respect to CST.

5.3 Conclusions

A new and fast efficient ray-tracing algorithm called rAIdome for the estimation of the main radar KPIs was fully developed and validated, with a very good correlation with the simulations done using CST. This algorithm can also be used to optimize the geometry of a radome. When combined with the used radar, one can achieve an optimum integrated solution.

Chapter 6

Conclusions and Future Work

The work conducted in this thesis has achieved the goals presented in the motivation and objectives section from the beginning.

- TE_{10} mode transmission line structures (Rectangular Waveguides (RW)/Groove Gap-Waveguides (GGW)) are much more robust to manufacturing errors than Q-TEM mode transmission line structures (Microstrip-Line (ML)/Ridge Gap-Waveguide

(RGW)). A robust vertical-GGW (V-GGW) series fed slot antenna ([**IZ-I**]) working in the W-Band is designed and validated showing good radiation performance; 12.15dB of realized gain, -16.5dB of SLL and 9% of fractional bandwidth (FBW). This antenna can be clearly mass produced supporting errors of up to ± 0.1 mm. Although the manufacturing process was not validated using plastic technology because of the limitations of the lab, it is still remaining for the future.

- Two types of ultra-wideband (UWB) transitions were designed [**IZ-II**] for the integration of waveguide-based antennas into RF-chips. By using three quarter wavelength length overlapped transversal patches, ML to RW transition is achieved showing 21.2% and 23% of FBW for top-side and bottom-side designs respectively, which is much greater than previous similar transitions.

- A W-band transition was also designed and validated [**IZ-III**], with a more complex manufacturing process due to the requirement of having a short-circuiting quarter wavelength box. This transition shows that the one from [**IZ-II**] can be scaled up to W-band too without problems.

- A 3D-printed plastic phased array (PA) of H-sectorial horn antennas [**IZ-IV**] working in Ka-band and using the top-side transition from [**IZ-II**] was successfully designed and validated using a commercial beamforming chip. Showing the potential

of plastic manufacturing processes on creating complex antenna systems like PA, with no doubts can be performed for radar sensors too as the horns are non resonant structures.

- A new ray tracing software was fully implemented for the design of optimum radomes in front of a radar sensor.

In this regard, it can be concluded that all the different technologies to create a plastic injected radar antenna are well explored and validated showing that plastic manufacturing technology as well as the additional processes required such as metal coatings are good candidates for the manufacturing of high demanding automotive antennas with a great potential for mass production as required by the actual market. The integration of a plastic radar antenna in the aesthetics of a car can be optimally performed by optimizing the radome in front of a radar so the main KPIs can be estimated very fast.

There are few works remaining for the future that is combining all the explored technologies to make a plastic radar antenna prototype at the W-band (76GHz-81GHz), integrate it with the chip and evaluate the DoA and attenuation when placing it behind a radome. There has been some work done in this thesis using a MIMO configuration and H-sectorial horn antennas as radiating and receiving elements, with RW distribution lines and transition to ML so it is ready to be connected with the radar chipset through the Texas Instruments evaluation module (EVM) 1642, see Figure 6.1.

(a) Manufactured radar prototype   (b) Exploded view of the radar prototype
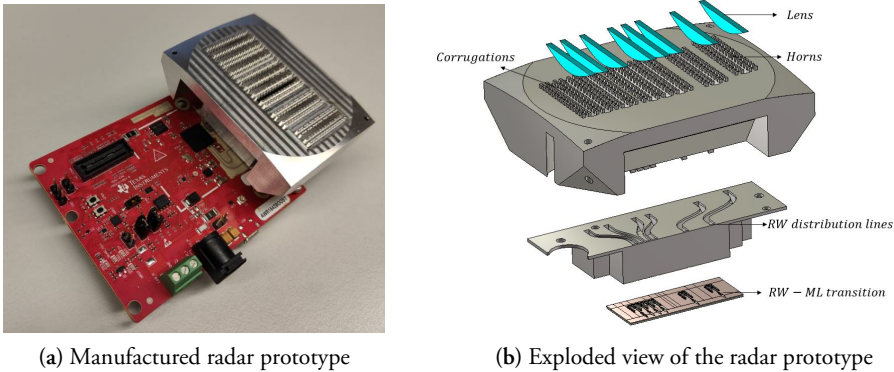
Figure 6.1: Metallic prototype manufactured using CNC technology

However, the connection of the ML to the EVM was not successful because of the limitations of our resources. A cooperation with an external company that is specialized in integrating custom antennas to the radar chipsets can be a possible solution to our limitations. After validating this prototype using CNC milling machine, the

final step would be comparing the results with a plastic prototype and integrating it to an optimized radome, so all the explored technologies for injection molded antennas would be validated at the same time.

Chapter 7

Publications

7.1 [IZ-I]

Technology Assessment of Aperture Coupled Slot Antenna Array in Groove Gapwaveguide for 5G Millimeter Wave Applications

IVAN ZHOU [iD], LLUÍS JOFRE [iD], (Life Fellow, IEEE), AND JORDI ROMEU [iD], (Fellow, IEEE)
Department of Signal Theory, Universitat Politècnica de Catalunya (UPC), 08034 Barcelona, Spain

Corresponding author: Ivan Zhou (ivan.zhou@upc.edu)

ABSTRACT A compact triple-layer series fed slot unit array using Groove Gap Waveguide (GGW) technology for 5G millimeter-wave applications is presented in this paper. The design employed a two-step coupling mechanism for the radiating slots. The aperture coupling design when combined with the groove gapWaveguide (GGW) technology allows achieving three different goals: First, a reduction of the array size in the transversal direction, so more unit arrays can be added without grating lobes. Secondly, low insertion losses with high radiation efficiency. And third, a reduction of the manufacturing complexity with good stability against fabrication tolerances of up to 0.1 mm, making the design feasible to be massively deployed. The antenna was fabricated and measured showing good agreement with the numerical simulation results, the antenna provides a peak realized gain of 12.15dB at the central frequency of operation and a fractional bandwidth (FBW) of 9%.

INDEX TERMS Compact antenna, series fed slotted array, 5G millimeter wave antennas, robust antenna.

I. INTRODUCTION

The increasing demand for high data speed, such as 8K video streaming and virtual augmented realities is expected to fold-1000 the data traffic in the upcoming decade [1]. Exploring new less-congested spectrum bands of high frequencies such as the millimeter-wave (mmWave) bands (30 - 300 GHz) is a promising solution to increase network capacity. However, new architectures with densification of small-cell technologies are required to mitigate propagation losses, reduce interference and increasing coverage [2]. Such densification requires the extensive deployment of dense wireless networks such as backhaul, for aggregating and sending data traffic from the radio access to the (wired) backbone segment or the cost-effective 5G smart repeaters to ensure a complete wireless coverage in difficult urban spots, among many other requirements. In this regard, high-gain antennas robust to manufacturing tolerances are required for the massive distribution of wireless network nodes. 5G mmWave band comprises the FR2 band, with frequencies ranging from 24.25GHz to 48.2 GHz where smart

repeaters and many backhaul applications work on. However, the FR2 band for the latter one is not sufficient to deliver today's capacity peaks [3], offloading to E-band (71-76GHz and 81-86GHz) spectrum is taking place.

In addition, a minimum antenna gain of 43 dB at E-Band is imposed by the FCC to 5G Backhaul cells, which requires a large antenna size such as 1-foot parabolic antennas, compared to 5G smart repeaters only 22 dB is required. Companies such as Ericsson and Nokia, alongside Avit and Comsearch pushed to decrease the antenna gain requirement to 38 dB in order to support smaller antennas, so integration in equipment at the street level such as light poles can be easier [4]. There is a clear trend to reduce the antenna size, so a more compact solutions can be adopted. It is obvious that gain requirements fix the minimum antenna dimension but a technology with higher efficiency and smaller thickness requirements will be preferred. More integrated solutions have been proposed such as horn arrays [5], transmit arrays [6], and lens antennas [7] but the size is still too bulky to be easily fitted on urban equipment.

In this context, compact low-thickness, high-efficiency, high-gain antennas with good fabrication tolerance stability are required for 5G mmWave network deployments. When

referring to very compact solutions traditional arrays are an attractive solution and can be mainly classified into corporate feeding networks and series fed arrays. The first is more commonly used for fixed point-to-point communications while with the latter technique, a phased array solution can be implemented making it more preferable.

Conventional series-fed arrays in a microstrip line can be found in [8] and [9]. However, the losses with dielectric and its uncertainties on the actual value of permittivity make it difficult to correlate the measured results with the simulations at these high frequencies. Waveguides can solve these problems as the dielectric is avoided by using four sealed walls to guide the electromagnetic wave through the air medium. Similar arrays in rectangular waveguide (RW) can be found in the literature by implementing slots, and they are mainly classified into two categories, vertical rectangular waveguide (V-RW) or narrow wall slots [10] and horizontal rectangular waveguide (H-RW) or broad wall slots [11]. Regarding V-RW, they offer more compactness in the antenna plane so beam steering capabilities using $\lambda/2$ separated unit arrays can be achieved without many dimensional restrictions as well as a considerable reduction in sidelobe level (SLL). However, the slots must be excited using a tilt angle as currents are in counter phase every $\lambda_g/2$ [12], [13], which is highly undesirable as cross polarization (CPol) appears. Many studies have been conducted in order to make these elements radiate in phase while maintaining low levels of CPol by using parasitic elements inside the waveguide to modify the current distribution [14]; however, a very demanding manufacturing precision is required and they are bandwidth limited. In addition, fast prototyping of waveguides needs to be manufactured on separate pieces, requiring perfect sealing when unifying them in order to avoid leakage [15].

In this context, gapWaveguide (GW) has attracted attention during the last decade, and the invention by S. Kildal offers a contactless full metal two parallel plates guiding structure solution by using an artificial magnetic conductor (AMC) at both sides of the transmission line, so all the electromagnetic energy is confined by the parallel plates and the AMC [16]. The AMC can be achieved by rows of periodic nails, although other conformations can be adopted such as mushrooms type [17], with the only condition that the space between the AMC and the parallel plate is smaller than $\lambda_g/4$. Clearly, in this configuration, there is no need for an electrical connection between the top and bottom conductive planes of the waveguide, leading to a low loss and relatively easy manufacturing process.

In order to benefit from the advantages of the GW technology, different designs have been reported in the literature, which can be classified into two main groups, ridge gapWaveguide (RGW) [18] which is the most popular design owing to its analogy to the microstrip line but in an inverted form and GGW [19] with a working principle similar to that of RW. There are two subgroups of GGW technology: named horizontal groove gapWaveguide (H-GGW) and vertical groove gapWaveguide (V-GGW). Some designs have

been made on H-GGW [20] but the size is too long in the transversal direction of the array similar to H-RW. Only a few works have been published to solve the problems of slot excitation using V-GGW, in [21] parasitic dipole elements are used in the upper layer by means of an extra layer of substrate; however, it only shows 2% FBW.

TABLE 1. Comparison with other similar works. The minimum separation parameter from the fifth column is the minimum inter-array separation achievable of the design, η is the measured efficiency.

Ref.	Tech.	CPol	FBW (%)	Min. separation (λ)	Thickness (λ)	η
Conventional Integrated Solutions						
[5]	Horn	No	29.5	NA	4	NA
[6]	TA	No	15.4	NA	11	48
[7]	Lens	No	NA	NA	27	NA
Series fed Solutions						
[9]	Micros.	No	7	0.55	0.03	39
[11]	H-RW	No	6.2	1.3	0.7	90.2
[12]	V-RW	Yes	2.1	0.5	0.7	NA
[13]	V-RW	Yes	9	0.5	0.7	80
[14]	V-RW	No	6.4	0.29	0.61	NA
[20]	H-GGW	No	2.8	1.32	0.33	93
[21]	V-GGW	No	2	0.57	0.75	NA
[22]	RGW	No	14.4	0.65	0.7	NA
[23]	RGW	No	3.8	0.49	0.165	NA
This work	V-GGW	No	9	0.57	1.91	92.2

In comparison to the antennas presented in the literature (see Table 1), we propose a new method for exciting narrow wall slots from V-GGW without added manufacturing complexity and a good fabrication tolerance stability of up to 0.1 mm (corresponding to the tolerances of a conventional manufacturing technique). The antenna consists of a triple-layer structure with a novel aperture coupling mechanism offering a linearly polarized, high efficiency (92.2%) with a high measured FBW (9%) while being compact in the transversal direction, so the gain can be simply increased by just adding more unit arrays along the transversal direction of the array without having large SLL.

The paper is organized as follows, in the next section II the antenna structure and working principle are described, section III shows a study of the tolerance in different GW technologies and a comparison with a conventional design of series fed array in RGW is made at simulation level, in section IV the results of the measured prototype and simulated ones are correlated and concluded in section VI. In section V the limitations of the work done in this study are also introduced.

II. ANTENNA DESIGN

The challenge in the development of new highly integrable antennas for urban 5G mmWave wireless nodes raises the

demand for new compact solutions with low fabrication precision requirements, high efficiency, and high gain with beam-pointing requirements in some scenarios. Series fed slots in V-GGW technology were chosen as a good candidate because of three main reasons. First, with only one excitation port, all the elements radiate in phase, reducing the complexity of the feeding network when compared to corporate feeding. Second, the antenna is compact in the transversal direction of the array, so gain can be increased by simply adding 0.5λ spaced arrays in that direction without losing beam steering capabilities. Finally, it offers an easy assembly process.
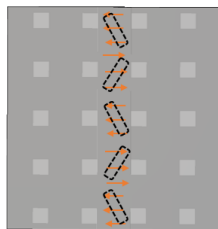
A. SLOT EXCITATION PROBLEM

The slot elements from a series fed design in the narrow wall of vertically oriented waveguide-related technologies cannot be directly excited as stated in the introduction.
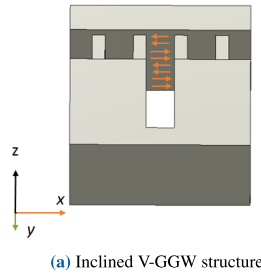
**(a)** Inclined V-GGW structure
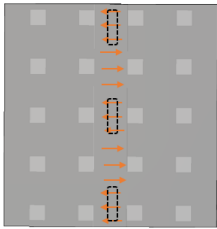
**(b)** Direct solution   **(c)** Conventional solution

FIGURE 1. (a) V-GGW transmission line structure showing the electric currents over the surface of the top wall in orange, they are in phase every λ_g (b) Solution to excite λ_g spaced longitudinal slots in V-GGW (c) Solution to excite $0.5\lambda_g$ spaced slots in V-GGW.

The currents from the top wall of the V-GGW are in counter phase every $0.5\lambda_g$ and oriented towards the transversal direction of the transmission line (see Fig. 1). Longitudinal slots can be implemented (see Fig. 1) (a) with a spacing of λ_g in order to radiate in phase; however, this will result in large grating lobes. A conventional method to keep the elements radiating every $0.5\lambda_g$ as shown in Fig. 1 (b) is performed by using tilted slots, however this will result in high levels of CPol. Many studies have been carried out using intrusion elements or an extra layer of substrate-based radiating elements as stated in the introduction an antenna with no

grating lobes and low CPol level can be achieved at the same time. However, they are either bandwidth-limited or require a high manufacturing precision. An isometric and top view of the proposed unit array antenna for this study with $0.5\lambda_g$ radiating slots in V-GGW technology can be seen in Figs. 2 and 3 respectively.
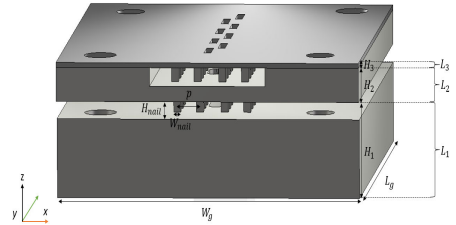
FIGURE 2. Isometric view. Bottom layer L_1, middle layer L_2 and top layer L_3.
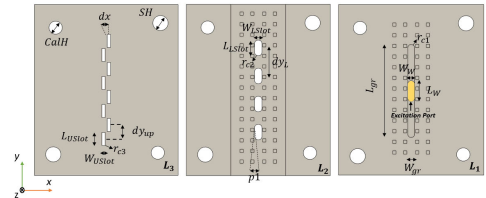
FIGURE 3. Top view of the three different layers. In yellow it is highlighted the input excitation port to the antenna prototype and r_{c1}, r_{c2}, r_{c3} represent the radius of curvature of the flagged edges.

B. PROPOSED ANTENNA

The V-GGW antenna is mainly composed of three layers: the feeding layer (bottom) L_1, coupling layer (middle) L_2 and radiating layer (top) L_3, whose dimensions are listed in Tab. 5. In the bottom layer L_1 there is a direct transition from WR-10 to GGW which consists of a slot ($W_W \times L_W \times H_W$) with corners of r_{c1} radius of curvature. An H-Plane power divider [24] is used to make a central feeding possible in order to achieve symmetrical fields at the radiating elements. The power divider is matched through a stepped transition inserted just below the middle layer L_2 with dimensions ($W_{t1} \times L_{t1} \times H_{t1}$) and ($W_{t2} \times L_{t2} \times H_{t2}$) as shown in Fig. 4.

The groove line ($W_{gr} \times L_{gr} \times H_{gr}$) has rounded ends with r_{c1} radius of curvature. All the energy from the guiding line propagates through four slots ($W_{Lslot} \times L_{LSlot}$) from the middle layer L_2 with corners of tye r_{c2} radius of curvature. These slots are approximately spaced λ_g from each other so they radiate in phase and each one of them, excites two of the eight $\lambda_g/2$ spaced slots of ($W_{USlot} \times L_{USlot}$) from the top layer L_3 with a curvature radius of r_{c3}. In this manner, all the slots radiate in phase with no grating lobes or high CPol level problems.

A symmetrical optimized distribution was considered for the radiating slots, where the intensity of the coupled fields
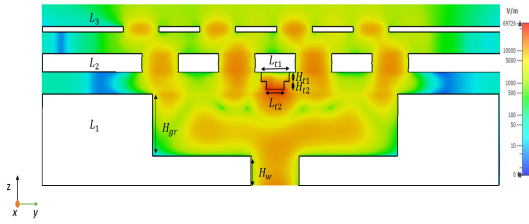
FIGURE 4. Electric Field distribution in linear scale in the x = dx plane cut.

was adjusted by L_{gr} and the offset of the radiating slots dx in order to achieve the lowest SLL while maintaining a high FBW. Lower SLL distributions such as Chebyshev and Taylor can be implemented using a non-uniform offset dx of radiating slots from the top layer L_3 to adjust the coupled energy.
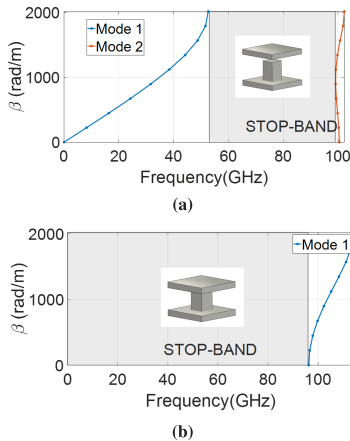

FIGURE 5. (a) With air gap = 0.25λ and (b) direct contact, being the height of the nails of 0.95 mm, width of 0.5 mm and periodicity of 1.6 mm.

The central elements from layers L_1 and L_2 are surrounded by a bed of nails with direct contact with the upper layer and a small spacing p1 with respect to the groove line. It acts as an AMC that prevents leakage through the sides of the transmission line. The dimensions of the bed of nails must be designed to ensure a good AMC performance at the frequencies of interest. A fast calculation of the modes of propagation can be performed by defining the unit cell of the bed of nails via the eigenmode solver from the CST simulator. In Fig. 5 the stopband of the AMC structure ranges from 60 GHz to 100 GHz if an air gap of 0.25λ is left between the upper layer and the nails, and 0-100GHz if they are in direct contact. If the nails are in contact with the upper layer, one single row of nails would be sufficient as will be demonstrated in the experimental section IV, resulting in a more compact unit array (0.57λ of minimum width x 1.91λ height). Two calibrated metallic screws (*CalH*) were used to

prevent misalignment between the layers and two metallic screws (*SH*) to fix the separation between the layers.

III. TOLERANCE ANALYSIS

The massive deployment of antennas requires an important analysis of the manufacturing tolerances. In order to ensure a good radiation performance for N antennas with fabrication tolerances of up to 0.1mm (which is a standard manufacturing tolerance for many industrial technologies) at high frequencies like E-Band is one of the main challenges that this paper has focused on. Gap waveguide technology was selected mainly because of its low loss and easy assembly properties.

A. DESIGN

A first test consisted of a comparison between the impedance stability of the three types of GW, the H-GGW, V-GGW and RGW when introducing dimensional errors of ±0.1mm in order to check the impedance stability of each technology.

(a) H-GGW   **(b)** RGW
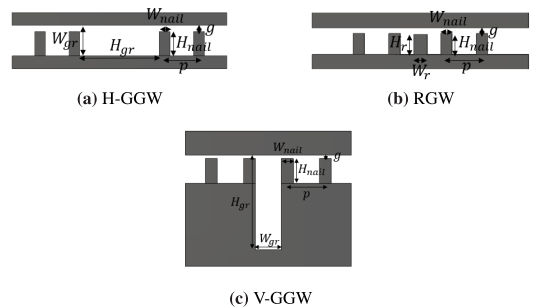

(c) V-GGW

FIGURE 6. Front view of the three main structures in GW technology that are used to analyze the characteristic impedance stability. The AMC structure dimensions are the same for (a), (b) and (c) with a constant air gap g of 0.25 mm between the nail and the top metallic layer.

TABLE 2. Tolerance analysis of the characteristic impedance for each GW technology.

H-GGW			
Parameter	Dimension (mm)	Impedance Zo (Ω)	Relative error (%)
W_{gr}	3.7 ± 0.1	150 ± 1	0.7
H_{gr}	1.05 ± 0.1	150 ± 12	8
H_{nail}	0.95 ± 0.1	150 ± 0.5	0.3
W_{nail}	0.5 ± 0.1	150 ± 0.35	0.3
p	1.6 ± 0.1	150 ± 0.2	0.1
V-GGW			
W_{gr}	1.1 ± 0.1	450 ± 2	0.4
H_{gr}	3.96 ± 0.1	450 ± 34	7.5
H_{nail}	0.95 ± 0.1	450 ± 2.5	0.5
W_{nail}	0.5 ± 0.1	450 ± 1.5	0.3
p	1.6 ± 0.1	450 ± 1.75	0.4
RGW			
W_r	0.6 ± 0.1	100 ± 6	6
H_r	0.9 ± 0.1	100 ± 27.5	27.5
H_{nail}	0.95 ± 0.1	100 ± 0.3	0.3
W_{nail}	0.5 ± 0.1	100 ± 0.25	0.25
p	1.6 ± 0.1	100 ± 0.23	0.23

As we can see in Tab. 2, H-GGW and V-GGW show similar impedance stability where the only critical dimension is the length of the narrow wall, introducing approximately 7.5 - 8 % of relative errors. For the case of RGW, up to 27.5% of the relative error was reached owing to the height of the ridge Hr, making RGW-related designs much more critical to fabrication tolerances. To compare the stability of the radiation pattern and input reflection coefficient with the design of this study, a conventional series fed array in RGW was simulated, as shown in Fig 7.
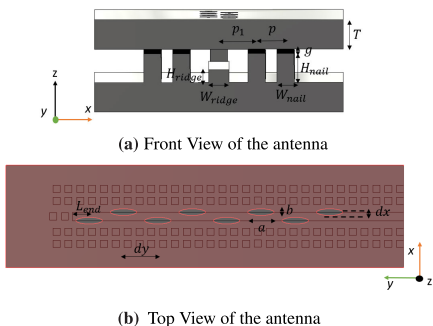

(a) Front View of the antenna

(b) Top View of the antenna

FIGURE 7. Series fed slot array in RGW design.

TABLE 3. Nominal dimensions of the antenna in RGW in mm. Parameters marked with at least one * are used for the tolerance analysis.

Param.	a**	b*	dx*	dy*	Wridge**	Hridge**	Lend*
Dim. (mm)	2.25	0.6	0.5	2.8	0.7	0.7	1.15
Param.	p*	p1*	g**	Wnail*	Hnail*	T*	-
Dim. (mm)	1	1.27	0.1	0.58	1	1.13	-

The antenna also has eight series fed slots with a spacing of approximately $0.5\lambda_g$. Note that only a single layer of radiating slots is needed to directly excite the elements in phase. L_{end} is approximately 0.25λ so all the remaining power is reflected back and a standing wave is created over the array axis. A uniform distribution of the delivered power was used with elliptical slots for bandwidth improvement. All the dimensions of each parameter are summarized at Tab. 3, for a complete description of a similar antenna, see [23].

B. ITERATION OF ERRORS

There are 13 dimensional parameters for the case of RGW design and 31 dimensional parameters for the case of V-GGW, assuming a uniform error distribution with only three discrete values of -0.1, 0 and $+0.1$ mm, see Tab. 4, for every single parameter this would result in a total amount of 1.59 million and over trillions of combined errors respectively, which is obviously not feasible to simulate.

A first analysis of the critical dimensions was carried out to reduce this space of combinations. Errors of $\pm\ 0.1$ mm were applied to each parameter separately for the RGW and V-GGW, resulting in 26 and 54 input reflection coefficients,

TABLE 4. Linear sweep used for each dimensional parameter. Each point represents the value that one parameter can get in the whole combined sweep.

| Sweep	1	2	3
Value (mm)	Nominal -0.1	Nominal	Nominal+0.1
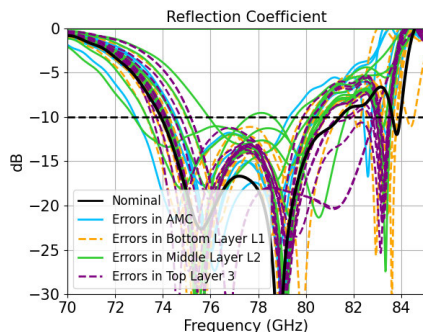
(a)Design in V-GGW.
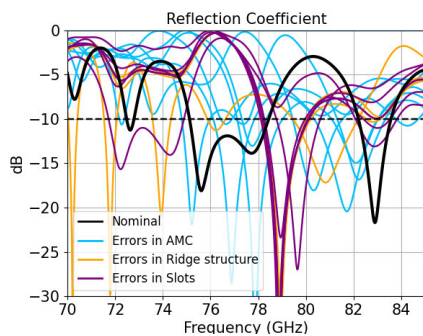
(b) Design in RGW.

FIGURE 8. Simulated input reflection coefficients by adding independently +0.1 mm and −0.1 mm of errors to each dimensional parameter while keeping the rest ones in nominal dimension.

the parameters used in this first study are marked with at least one * in Tab. 3 and Tab. 5 respectively. Some parameters were not included in the tolerance analysis such as the curvature radius (r_{c1}, r_{c2}, r_{c3}) because it is related to the shape rather than dimensional error and, the height of the feeding port (H_W) because it does not affect the impedance of the structure. Parameters from the Tabs. 3 and 5 marked with a double * are the most critical ones in terms of reflection coefficients seen at Fig. 8 (a) and (b) respectively, resulting in a penalty of greater than 15% of FBW reduction if taking into account that the only valid bands for both designs are those marked by the input reflection coefficient when using nominal dimensions. For V-GGW the critical parameters are the length of the slots from each layer L_{Lslot} and L_{USlot}, W_{nail} and $p1$. For the case of RGW the results are much worse (>50% of the FBW penalty) with any parameter. Only these

parameters are selected for the final study using combined errors and are plotted in Figs. 9 and 10.
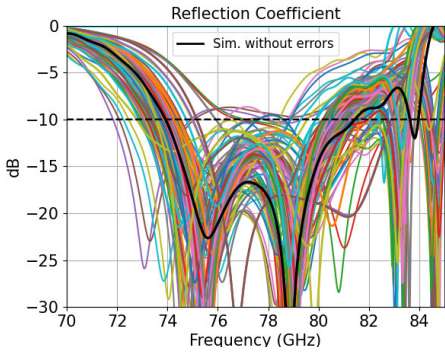
(a) Design in V-GGW. Total amount of 243 combined errors.
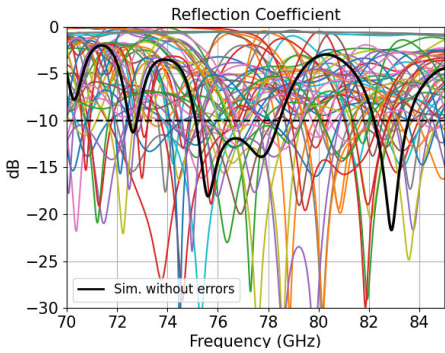
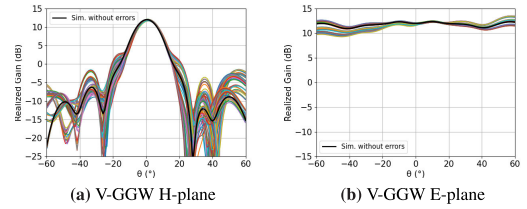**(b)** Design in RGW. Total amount of 81 combined errors

FIGURE 9. Input reflection coefficients for the main combination of errors in color, the black trace corresponds to the simulated antenna with nominal dimensions.

For the case of the input reflection coefficients in this V-GGW design, 89% of the combined errors guarantee a frequency range from $74.25 GHz$ to $80 GHz$, resulting in a 7.5% secured FBW. Clearly, V-GGW shows much better tolerance stability than RGW, as predicted previously in the Design subsection.

Only pattern stability for the design in V-GGW is represented in Fig. 10 because the results are well-matched, showing good pointing stability as well as realized gain. An increase of up to 7.5dB in SLL was due to the errors related to the slot spacing dY_{up} from the top layer L_3. Of course, if considering misalignment errors between each layer, we will have a worse response in terms of SLL although it has almost no impact on the input reflection coefficients.

IV. EXPERIMENTAL RESULTS

The antenna was manufactured using two different methods. $L1$ and $L2$ were fabricated using a standard CNC milling machine from the UPC facilities.

(a) V-GGW H-plane   **(b)** V-GGW E-plane

FIGURE 10. V-GGW design radiation pattern cuts for the main combination of errors in color, - corresponds to the simulated antenna with nominal dimensions. The tolerance of the pattern for the design in RGW was not included as the input reflection coefficients are very mismatched.
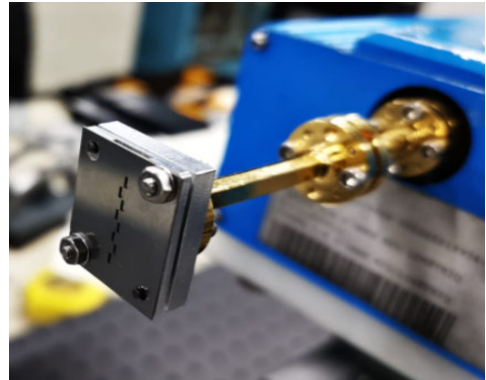
FIGURE 11. Manufactured antenna at the head of the PNA N5222A network analyzer.

TABLE 5. Summary of the main antenna dimensions and the deviations in the fabricated one in mm. The errors for the case of the slots and nails are the maximum errors. Parameters marked with at least one * are used for the tolerance analysis from section III.

Param.	Nom. (mm)	Error (mm)	Param.	Nom. (mm)	Error (mm)
Layer 1			**Layer 2**		
H_{gr}*	2.7	0.02	L_{Lslot}**	2.35	0.07
L_{gr}*	13.95	0.08	W_{Lslot}*	1.1	0.11
W_{gr}*	1	0	dY_L*	4.25	0.05
L_W*	3.1	0.05	r_{c2}	0.5	-
W_W*	1	0.12	H_{t1}*	0.4	0.09
H_W	1.35	-	L_{t1}*	1.55	-0.15
r_{c1}	0.5	-	H_{t2}*	0.35	0.12
H_1*	5	0.03	L_{t2}*	1	-0.17
			W_{t1}*	1.1	0
Layer 3			W_{t2}*	1.1	0
			H_2*	1.75	-0.04
L_{USlot}**	2	0.03	**AMC**		
W_{USlot}*	0.5	-0.01			
dY_{up}**	2.25	0.01	p*	0.88	0.03
$DispX3$*	0	0.15	W_{nail}**	0.5	0.07
$DispY3$*	0	-0.10	H_{nail}*	0.95	0.01
dx*	0.4	0	$p1$**	0.1	0.05
r_{c3}	0.025	-	H_3*	0.25	0

$L3$ was fabricated externally using laser cutting technology as the width of the slots was too thin to be performed at our facilities. Fabricated dimensional errors are listed in

Tab. 5, which were measured using the Nikon Measurescope MM-11 with a precision of 10um. Pictures showing the main fabricated parts of the structure are shown in Fig. 12.
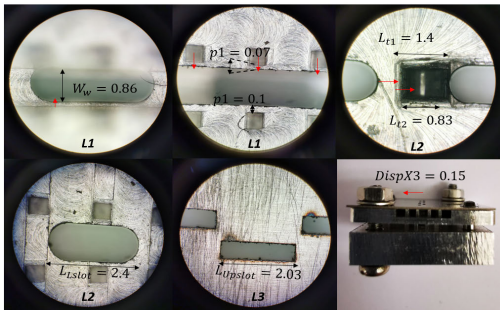

FIGURE 12. Manufactured antenna seen by the microscope, showing the main parts of the structure.

The most deviated errors were caused by the displacement of the $L3$ layer ($DispX3$ and $DispY3$), the connection of the WR10 (W_W) to the waveguide structure, the width of the slots W_{Lslot} of $L2$ and dimensions (height × length) of the stepped matching element ($H_{t1} \times L_{t1}$) and ($H_{t2} \times L_{t2}$) with a deviation up to 0.15 mm. The reason for the large displacement off $L3$ was the positional error of the calibrated and screwed holes. Measurements were performed in a $4 \times 4 \times 3\ m^3$ room from the UPC facilities, with a proper time gating post-processing technique, the reflections inside the room can be filtered out [25]. The measurements and simulations using CST Studio software included the reflection coefficients and realized gain patterns, which were cut at 77 GHz, and are shown in figures 13, 15 and 16.
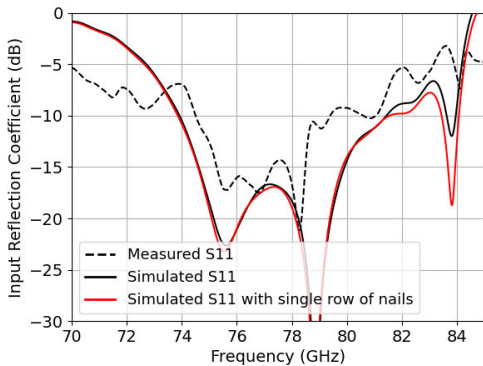

FIGURE 13. Input reflection coefficients of the antenna. In black a double row of nails for the AMC is used and in red color corresponds to the simulated antenna by just using only one row of nails to show that it can be compact in the transversal direction of the array. Discontinuous lines (- -) are the measured results while continuous lines (-) are simulated results.

There is a good correlation between the measured input reflection coefficient (74.5GHz - 81.25GHz) and the simulated one (74GHz - 81.5GHz). A portion of mismatched
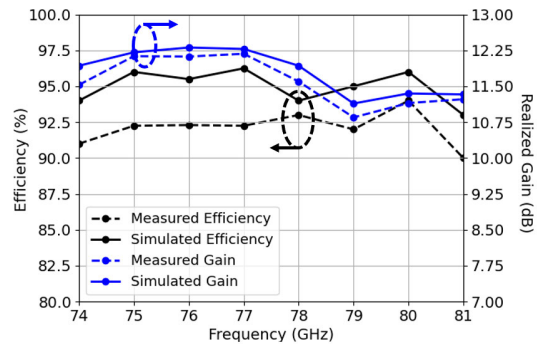

FIGURE 14. Left vertical axis corresponds to the efficiency in black and the right axis corresponds to the realized gain in blue color. Discontinuous lines (- -) are the measured results while continuous lines (-) are simulated results.

frequencies ranges from 79.25 to 80.75 GHz at only −9.1 dB. The design was performed using a double row of nails with direct contact with the upper layer, which would result in large dimensions in the transverse direction of the array. However one single row of nails is sufficient, resulting in a more compact form (0.57λ width × 1.91λ height) without altering the results (see Fig 13). The stability of the gain versus frequency for the whole band is shown in blue in the right axis of Fig. 14, with a maximum gain reduction down to 11dB at 79GHz. In the same Fig. 14 we can also see the efficiency of the antenna in black color which was measured to be greater than 90% for the whole band ranging from 74GHz to 81GHz.
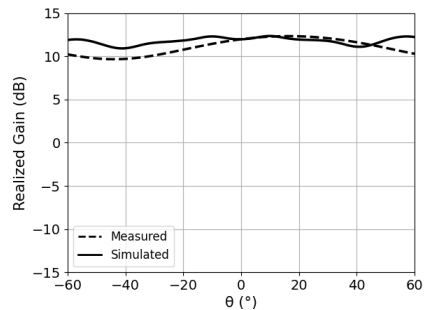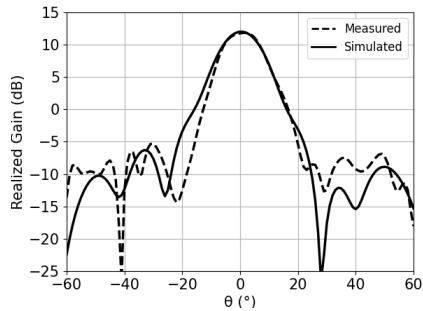

FIGURE 15. Radiation pattern cuts at E-plane, - corresponds to the simulated antenna, and - - corresponds to the actual measured prototype.

A realized gain of 12.15 dB was measured which also showed good agreement with the simulations for both planes at 77GHz. A simulated SLL of −18.5dB in H-plane was increased up to −16.5 dB at $\theta = -28$ deg in the measurements caused by the misalignment of the radiating layer l_3 with respect to the other two ones, leading to a non-perfect symmetrical field distribution among the radiating slots.

V. LIMITATIONS OF THE STUDY
In this paper we show a new method for exciting series fed slot arrays in V-GGW, although the design is easy to be scaled

FIGURE 16. Radiation pattern cuts at H-plane, - corresponds to the simulated antenna, and - - corresponds to the actual measured prototype.

to a larger aperture antenna for 5G mmWave applications by just adding more arrays, there are some remaining studies to be done.

First, when scaling to N arrays spaced at 0.57λ (minimum achievable inter-array space with this design), a compact distribution network needs to be designed.

Second, only eight elements were used in the series-fed array. For achieving high gain levels required by future 5G mmWave applications, further studies have to be carried out by using more array elements depending on the specific 5G mmWave application and see its impact on the FBW and the tolerances in order to simplify its scalability.

VI. CONCLUSION

A single compact series-fed array antenna using a novel aperture coupling mechanism in V-GGW technology has been proposed. The measured gain of the antenna was 12.15dB by comparing it to a standard horn antenna of 23.5dB. The efficiency at 77GHz was measured to be 92.25% by assuming a directivity similar to the simulated one (12.5 dB). The antenna offers a simulated FBW of 10% which is reduced to 9% when measuring it.

The antenna shows good stability against fabrication errors of up to 0.1 mm for both input reflection coefficients and radiation pattern, which is much better than the design in RGW. It provides a minimum realized gain of 12.1dB at 77GHz for the worst case of combined errors at the simulation level and offer good tilting stability. The radiating aperture of the antenna can be increased by adding more unit arrays to increase the directivity and the frequency can be scaled depending on the specific application of future 5G mmWave wireless networks requiring massive deployments.

REFERENCES

[1] J. G. Andrews, S. Buzzi, W. Choi, S. V. Hanly, A. Lozano, A. C. K. Soong, and J. C. Zhang, "What will 5G be?" *IEEE J. Sel. Areas Commun.*, vol. 32, no. 6, pp. 1065–1082, Jun. 2014.

[2] J. Rodriguez, *Small Cells for 5G Mobile Networks*. 2014, pp. 63–104.

[3] P. Wang, Y. Li, L. Song, and B. Vucetic, "Multi-gigabit millimeter wave wireless communications for 5G: From fixed access to cellular networks," *IEEE Commun. Mag.*, vol. 53, no. 1, pp. 168–178, Jan. 2015.

[4] *FCC Advances 70-90 GHz Changes To Support Wireless 5G Backhaul*. [Online]. Available: https://www.fiercewireless.com/tech/fcc-advances-70-90-ghz-changes-to-support-wireless-5g-backhaul

[5] S. R. Zahran, L. Boccia, G. Amendola, S. Moscato, M. Oldoni, and D. Tresoldi, "Broadband D-band antenna array based on 64 stepped horns for 5G backhauling applications," in *Proc. 15th Eur. Conf. Antennas Propag. (EuCAP)*, Mar. 2021, pp. 1–5.

[6] L. Dussopt, A. Moknache, J. Säily, A. Lamminen, M. Kaunisto, J. Aurinsalo, T. Bateman, and J. Francey, "A V-band switched-beam linearly polarized transmit-array antenna for wireless backhaul applications," *IEEE Trans. Antennas Propag.*, vol. 65, no. 12, pp. 6788–6793, Dec. 2017.

[7] J. Ala-Laurinaho, J. Aurinsalo, A. Karttunen, M. Kaunisto, A. Lamminen, J. Nurmiharju, A. V. Räisänen, J. Säily, and P. Wainio, "2-D beam-steerable integrated lens antenna system for 5G *E*-band access and backhaul," *IEEE Trans. Microw. Theory Techn.*, vol. 64, no. 7, pp. 2244–2255, Jul. 2016.

[8] S. Afoakwa and Y.-B. Jung, "Wideband microstrip comb-line linear array antenna using stubbed-element technique for high sidelobe suppression," *IEEE Trans. Antennas Propag.*, vol. 65, no. 10, pp. 5190–5199, Oct. 2017.

[9] J.-H. Lee, J. M. Lee, K. C. Hwang, D.-W. Seo, D. Shin, and C. Lee, "Capacitively coupled microstrip comb-line array antennas for millimeter-wave applications," *IEEE Antennas Wireless Propag. Lett.*, vol. 19, no. 8, pp. 1336–1339, Aug. 2020.

[10] J. Hirokawa and P. S. Kildal, "Excitation of an untilted narrow-wall slot in a rectangular waveguide by using etched strips on a dielectric plate," *IEEE Trans. Antennas Propag.*, vol. 45, no. 6, pp. 1032–1037, Jun. 1997.

[11] S. C. Y. Tyagi, P. Mevada, and R. Jyoti, "High-efficiency broadband slotted waveguide array antenna," *IET Microw., Antennas Propag.*, vol. 11, no. 10, pp. 1401–1408, 2016.

[12] M. A. K. S. Lubis, C. Apriono, F. Y. Zulkifli, and E. T. Rahardjo, "Design of narrow wall slotted waveguide antenna for X-band application," in *Proc. Prog. Electromagn. Res. Symp.-Fall (PIERS-FALL)*, 2017, pp. 2625–2628.

[13] D. P. Yusuf, F. Y. Zulkifli, and E. T. Rahardjo, "Design of narrow-wall slotted waveguide antenna with V-shaped metal reflector for X-band radar application," in *Proc. Int. Symp. Antennas Propag. (ISAP)*, Oct. 2018, pp. 1–2.

[14] T. Uesaka, N. Nakamoto, T. Fukasawa, N. Yoneda, T. Yamamoto, T. Koyanagi, I. Kakimoto, and Y. Konishi, "Design of edge-slotted waveguide array antenna manufactured by injection-molding," in *Proc. IEEE Int. Symp. Phased Array Syst. Technol. (PAST)*, Oct. 2019, pp. 1–4.

[15] H. Takahashi, T. Kosugi, A. Hirata, J. Takeuchi, K. Murata, and N. Kukutsu, "Hermetic sealing technique for F-band waveguides and packages," in *Proc. 41st Eur. Microw. Conf.*, Oct. 2011, pp. 269–272.

[16] E. Rajo-Iglesias, M. Ferrando-Rocher, and A. U. Zaman, "Gap waveguide technology for millimeter-wave antenna systems," *IEEE Commun. Mag.*, vol. 56, no. 7, pp. 14–20, Jul. 2018.

[17] E. Pucci, E. Rajo-Iglesias, and P.-S. Kildal, "New microstrip gap waveguide on mushroom-type EBG for packaging of microwave components," *IEEE Microw. Wireless Compon. Lett.*, vol. 22, no. 3, pp. 129–131, Mar. 2012.

[18] S. Kildal, A. Zaman, E. Rajo, E. Alfonso, and A. Nogueira, "Design and experimental verification of ridge gap waveguide in bed of nails for parallel-plate mode suppression," *IET Microw., Antennas Propag.*, vol. 5, no. 3, pp. 262–270, 2009.

[19] E. Rajo-Iglesias and P. Kildal, "Groove gap waveguide: A rectangular waveguide between contactless metal plates enabled by parallel-plate cut-off," in *Proc. 3th Eur. Conf. Antennas Propag.*, Apr. 2010, pp. 1–4.

[20] Z. Shaterian, A. K. Horestani, and J. Rashed-Mohassel, "Design of slot array antenna in groove gap waveguide technology," *IET Microw., Antennas Propag.*, vol. 13, no. 8, pp. 1235–1239, Jul. 2019.

[21] J. I. H. Herruzo, A. Valero-Nogueira, S. M. Giner, and A. V. Jiménez, "Untilted narrow-wall slots excited by parasitic dipoles in groove gap waveguide technology," *IEEE Trans. Antennas Propag.*, vol. 63, no. 11, pp. 4759–4765, Nov. 2015.

[22] Z. Talepour, S. Esmaili, and A. Khaleghi, "Ridge gap waveguide antenna array using integrated coaxial power divider," in *Proc. Loughborough Antennas Propag. Conf. (LAPC)*, Nov. 2015, pp. 1–5.

[23] A. Haddadi, C. Bencivenni, and T. Emanuelsson, "Gap waveguide slot array antenna for automotive applications at *E*-band," in *Proc. 13th Eur. Conf. Antennas Propag. (EuCAP)*, Mar./Apr. 2019, pp. 1–4.

[24] A. Farahbakhsh, D. Zarifi, and A. U. Zaman, "60-GHz groove gap waveguide based wideband *H*-plane power dividers and transitions: For use in high-gain slot array antenna," *IEEE Trans. Microw. Theory Techn.*, vol. 65, no. 11, pp. 4111–4121, Nov. 2017.

[25] M. Dadic, R. Zentner, and Z. Lenic, "Time-gating in antenna and microwave measurements using RDFT," in *Proc. 22nd Int. Conf. Appl. Electromagn. Commun. (ICECOM)*, Sep. 2016, pp. 1–4.
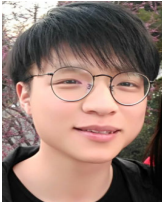
IVAN ZHOU was born in Valencia, Spain, 1996. He received the degree in engineering physics and the master's degree in advanced telecommunications technologies from the Polytechnic University of Catalonia (UPC), in 2019 and 2020, respectively, where he is currently pursuing the Ph.D. degree with the Antennalab, Signal Theory and Communications Department. He was involved in millimeter wave antenna design, radome design, and ray tracing algorithms.

LLUÍS JOFRE (Life Fellow, IEEE) received the M.Sc. and Ph.D. degrees in electrical engineering (telecommunication engineering) from the Universitat Politècnica de Catalunya (UPC), Barcelona, Spain, in 1978 and 1982, respectively. He was a Visiting Professor with the Ecole Supèrieure d'Electricitè Paris, from 1981 to 1982, where he was involved in microwave antenna design and imaging techniques for medical and industrial applications. Since 1982, he has been with the Communications Department, Telecommunication Engineering School, UPC, as an Associate Professor, and then a Full Professor, since 1989. From 1986 to 1987, he was a Visiting Fulbright Scholar with the Georgia Institute of Technology, Atlanta, GA, USA, where he was involved in antenna near-field measurements and electromagnetic imaging. From 2000 to 2001, he was a Visiting Professor with the Department of Electrical and Computer Engineering, Henry Samueli School of Engineering, University of California at Irvine, CA, USA, where he was involved in reconfigurable antennas and microwave sensing of civil engineering structures. He has been the Director of the UPC-Telefonica Chair on Information Society Future Trends, since 2003. He was the Principal Investigator of the 2008–2013 Spanish Terahertz Sensing Lab Consolider Project and the Research Leader of the 2017–2020 ComSense Lab Maria de Maeztu Project. He has authored more than 200 scientific and technical articles, reports, and chapters in specialized volumes. His current research interests include antennas, electromagnetic scattering and imaging, and system miniaturization for wireless, and sensing industrial and bio-applications from microwaves to terahertz frequencies. He was the Academic Director of the Consortium for Future Urban Mobility (Carnet) and the Chairman of the EIT-Urban Mobility European Association.

JORDI ROMEU (Fellow, IEEE) was born in Barcelona, Spain, in 1962. He received the Ingeniero de Telecomunicación and Doctor Ingeniero de Telecomunicaciòn degrees from the Universitat Politècnica de Catalunya (UPC), in 1986 and 1991, respectively. In 1985, he joined the Antennalab, Signal Theory and Communications Department, UPC, where he is currently a Full Professor, and involved in antenna near-field measurements, antenna diagnostics, and antenna design. He was a Visiting Scholar with the Antenna Laboratory, University of California at Los Angeles, Los Angeles, in 1999, on an NATO Scientific Program Scholarship, and the University of California at Irvine, in 2004. He holds several patents and has published 60 refereed articles in international journals and 80 conference proceedings. He was a Grand Winner of the European IT Prize awarded by the European Commission for his contributions in the development of fractal antennas, in 1998 (More information can be found in http://www.researchgate.net/profile/Jordi−Romeu).

• • •

7.2 [IZ-II]

Article

Ultra-Wideband Narrow Wall Waveguide-to-Microstrip Transition Using Overlapped Patches

Ivan Zhou * and **Jordi Romeu Robert**

School of Telecommunication Engineering, Universitat Politècnica de Catalunya, 08034 Barcelona, Spain; jordi.romeu-robert@upc.edu
* Correspondence: ivan.zhou@upc.edu; Tel.: +34-934-016826

Abstract: An ultrawideband rectangular waveguide to microstrip line transition operating at the whole LMDS and Ka band is presented. The transition is based on exciting three overlapped transversal patches that radiate into the narrow wall of the waveguide, making the design feasible to be used in $\lambda_g/2$ spaced phased arrays. Both top-side and bottom-side versions were designed and compared to show their differences. They were validated by means of a manufactured back-to-back (B2B) configuration, with a measured fractional bandwidth of 21.2% (top-side) and 23% (bottom-side). The maximum single transition measured insertion losses were 0.67 dB (top-side) and 0.85 dB (bottom-side) in the whole band of operation.

Keywords: ultra-wideband; millimeter-wave; beamforming

1. Introduction

With the upcoming 5G millimeter-wave (mmWave) communication, a clear enhancement of the data speed, latency, and network efficiency is expected [1]. Transmission losses at these frequency bands are high [2,3], which requires the use of low loss transmission lines and antennas such as rectangular waveguide (RW) and horns, for example [4]. In addition, packaging and integration of low loss antennas into the RF chipsets or connectors often require microstrip-to-waveguide transitions, making the design more integrated and compact [5,6].

There are three main type of transitions: inline [7,8], bottom-side (BS) [9–11], and top-side (TS) [12–16]. For the case of inline transitions, the direction of propagation of the fields for both microstrip line (ML) and RW are the same, whereas for the TS and BS, their directions are perpendicular. In the case of TS, the ML and the RW are on the same face of the substrate, whereas for the BS the ML and the RW are on opposite faces, which may be necessary depending on the design requirements.

Inline transitions have the advantage of offering huge bandwidth with low insertion losses (IL). In [8], a tapered ridge along the axis of the RW was proposed, covering the whole Ka-band, but it requires the RW to be fabricated in two separate pieces and the substrate to be suspended in the air; in order to guarantee a good performance, a solid substrate must be implemented. In [10], a BS transition was proposed via proximity coupling through a patch antenna, although it offers 18% of fractional bandwidth (FBW), it requires perpendicular input/output ports from the large wall of the RW, which makes the design bulkier. In [11], this FBW is highly increased to 33.3% by means of an E-plane probe, but side feeding is needed, which also shows the same disadvantages as inline transitions. In [14], this large wall is avoided with a narrow-wall design consisting of a V-shaped aperture coupled patch; however, only 7.5% of FBW is achieved. TS RW to ML transitions are also explored as in [15], where the RW is excited through a transversal patch antenna coming from the narrow wall; however, intrusion elements inside the RW have to be carefully inserted in order to enhance the FBW from 11% to 15%, which increases the fabrication complexity.

This intrusion element is avoided in [16] through a patch fed by a coupled ML, but only 11% of FBW is achieved.

In comparison with the transitions presented in this paper, a narrow-wall ML-RW transition is designed and validated using a manufactured back-to-back (B2B) configuration that can work for both TS and BS at the same time without increased manufacturing complexity. The transition consists of an ML that feeds an array of three overlapped transversal patches from the narrow wall of the RW, offering a much higher bandwidth when compared to similar presented work. The design shows a FBW of 21.2% for the TS design and 23% for the BS design.

2. Transition Design

The focus of this first section consists of the conversion of the Q-TEM mode of a 50 Ω ML [17] to the TE01 mode of a WR-34 ($W_{rw} \times L_{rw}$) [18]; a detailed description of the working principle will be given in Section 2.1 for the case of the TS transition where the RW is located on the same side of the substrate as the ML. In Section 2.2, a BS transition using the same working principle will be presented by just adding a metallic bias to connect the TS ML with the BS ML. Both TS and BS transitions will be compared in Section 3 to show the advantages and disadvantages of each type of transition, as depending on each design requirement, TS or BS will be needed.

2.1. Top-Side Transition

Figure 1a shows the isometric view of the transition, and Figure 1b shows its top and bottom view. The transition is designed using a 0.81 mm thick RO4003 substrate with a dielectric constant of Er = 3.55 and a loss tangent of 0.002.

(a)

(b)
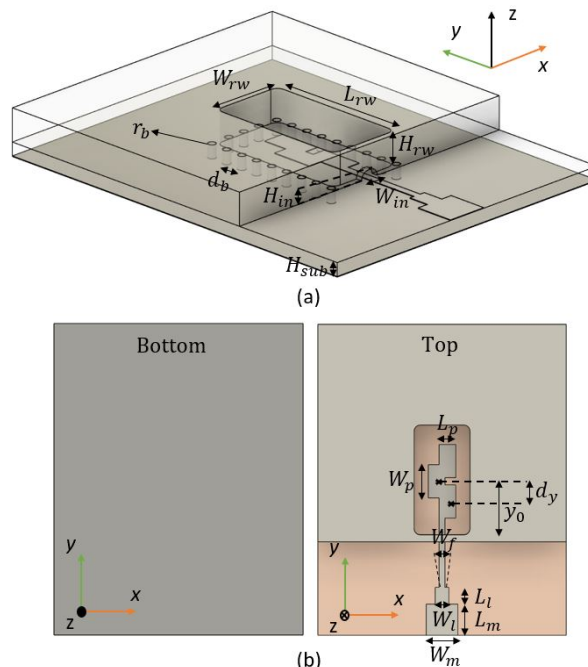
**Figure 1.** Artist view of the Top-Side transition for (**a**) isometric view and (**b**) top and bottom view.

A full-wave electromagnetic simulation tool, CST Microwave Studio, is used for its optimization. In order to excite the TE01 mode from the waveguide, excitation of transversal currents in the $\hat{x}$ direction is needed. A simple and direct ML-RW mode conversion can

be found in [15]. By using a single transversal patch with an approximated length of $\frac{1}{2}\lambda_g$, radiation with the proper polarization is achieved to excite the TE01 mode from the RW. However, it is bandwidth limited. As a way to enhance this bandwidth, an array of three overlapped transversal patches is proposed in this paper, the length Lp of the patches, the width W_p, inter-element distance d_y and array position with respect to the entrance of the RW y_0 are jointly optimized to provide maximum bandwidth. The overlapping of these $0.2\lambda_g$ length patches is crucial for the excitation of transversal $J\hat{x}$ currents. In Figure 2 we show a sketch of the current distribution at the central frequency of 26.5GHz along the patches (a) without the middle patch (no overlapping) and (b) with the middle patch (with overlapping). As we can see in Figure 2a, which is the transition with the parameters from Table 1 but without overlapping, the $J\hat{x}$ transversal currents are not excited by the patches at the central frequency f_0, because the effective length of the patches is not close to $\frac{1}{2}\lambda_g$.

Table 1. Dimensions in millimeters of each designed parameter for the top-side transition.

H_{sub}	0.81	W_f	0.47	W_{rw}	4.5
dy	1.625	W_l	1.1	L_{rw}	8.8
W_p	2.67	L_l	1.35	H_{rw}	2
L_p	1.35	L_m	2.5	H_{in}	0.5
Y_0	4.3	W_m	2.55	W_{in}	1.2
r_b	0.25	d_b	1.17		

With the introduction of a central patch element that overlaps with the other two from Figure 2a (see Figure 2b), the path of the currents along the transversal $\hat{x}$ direction is effectively enlarged, from $0.2\lambda_g$ to $0.4\lambda_g$, exciting in phase $J\hat{x}$ currents at lower frequencies, so the Q-TEM mode from the ML is directly converted to the TE01 mode for the RW as a result of the radiation of the array into the RW. Note that the currents are diagonal, so the path that the currents are taking to travel is slightly larger than $0.4\lambda_g$. In Figure 3 we can see the resonance frequencies for both cases with the presence of the RW.
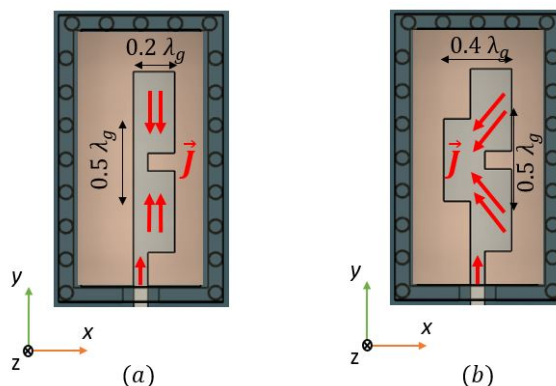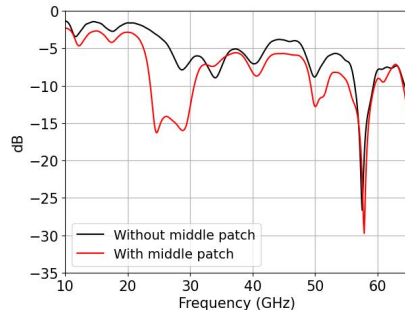

Figure 2. Top view of the current distribution at $f_0 = 26.5$ GHz of (**a**) the transition without overlapping, (**b**) the transition with overlapping.

The overlapped patches offer an intrinsic higher bandwidth behaviour when compared to a single patch element. The array is fed by a ML of width W_f, and it is matched to a 50 Ω circuit with a stepped section of $W_t \times L_t$. The entrance to the RW has dimensions ($Win \times Hin$), it should ideally be as little as possible to avoid leakage from the RW but not short-circuiting with the ML; however, a considerable dimension was chosen to be

manufacturable. There are via holes of radius r_b and periodicity d_b surrounding the aperture of the RW that connects the RW to the ground plane of the substrate; by reducing this periodicity, the insertion losses are not reduced.

Figure 3. Input reflection coefficients without overlapping (black) and with overlapping (red).

2.2. Bottom-Side Transition

The working principle of the BS transition is the same as the TS transition. The parameters are not exactly the same, as they were slightly re-optimized for this BS case, see Table 2. Figure 4 shows the top view, bottom view, and isometric view of this transition. The entrance of the ML along the bottom side is achieved by leaving a U-slot of width c around the ground. By adding a bias of radius r_b at the edge of this ML, we can connect and feed the overlapped patches from the other side, the TS. The ground plane has an extension of E_x with respect to the narrow wall RW. The via holes also have to be extended to the end of this ground plane, otherwise leakage through $\hat{x}$ direction will appear due to the currents excited by the U-slot.

(a)

(b)
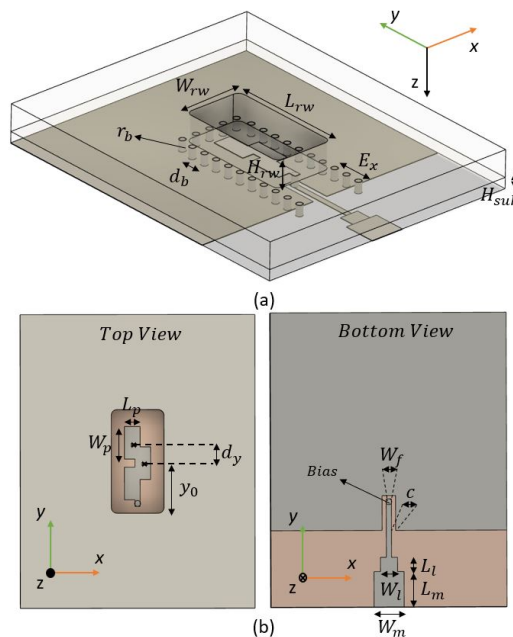
Figure 4. Artist view of the Bottom-Side transition for (**a**) isometric view and (**b**) top and bottom view.

Table 2. Dimensions in millimeters of each designed parameter for the bottom-side transition.

H_{sub}	0.81	W_f	0.44	W_m	2.55	Y_0	4.4
dy	1.73	W_l	1.45	L_m	2.5	r_b	0.25
W_p	2.77	L_l	1.2	H_{rw}	2	W_{rw}	4.5
L_p	1.33	d_b	1.17	C	0.15	L_{rw}	8.8
E_x	1.58						

This type of BS transition has an advantage with respect to the TS transitions involving interference reduction, as the RF-chipset may be located at the contrary face from the radiating elements. However, it comes with many disadvantages, as will be seen in the next section.

3. Simulated Results

Simulations involving a parametric study were carried out for both TS transition (see Figure 5) and BS transition (see Figure 6) to show a better understanding of the sensitivity of each parameter.
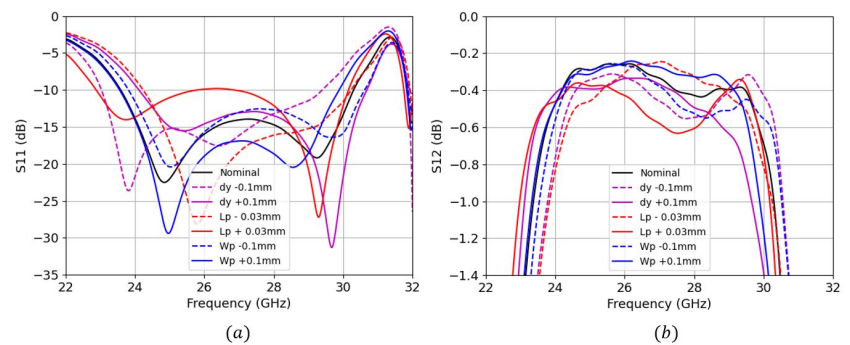
Figure 5. Top-side parametric study of S-parameters (**a**) input reflection coefficient (**b**) insertion losses.
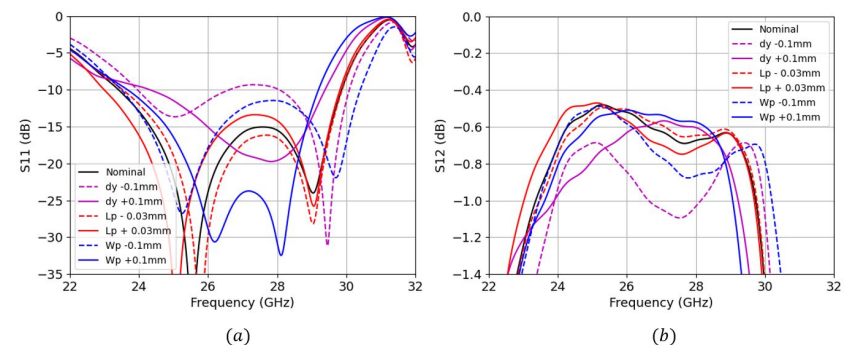
Figure 6. Bottom-side parametric study of S-parameters (**a**) input reflection coefficient (**b**) insertion losses.

We can see that the input reflection coefficient for both designs are very similar, ranging approximately from 23.75 GHz to 30 GHz. However, the maximum insertion losses (IL) for the BS are slightly worse (-0.65 dB) than for the TS (-0.4 dB) along the frequency band of operation. For the case of TS transition, we can clearly see two main resonant frequencies at 24.8 GHz and 29 GHz. The lower resonance frequency is controlled by the patch's length

L_p, whereas the upper resonance frequency is controlled by the patch's width W_p. Both resonant frequencies can be simultaneously shifted by adjusting the d_y. For the case of BS transition, L_p also controls the lower resonance frequency, W_p controls both resonances as well as d_y. We can also see that the sensitivity of the insertion losses against these parameter changes are much higher for the BS case; we see a maximum penalty of up to 0.4 dB for the $d_y - 0.1$ mm trace, and only 0.2 dB for the $L_p + 0.03$ mm trace from the TS case.

In Figure 7 we plot the leaked radiation for both TS and BS transitions. This simulation consists of placing both ML and RW ports and plotting the far-field when exciting the ML port. The leakage for the TS is -10.28 dB, whereas that for the BS is higher, peaking at -7.6 dB. In order to reduce this, the slot's width c from this ground should be as small as possible; however, it would not be viable to be manufactured. Another way to reduce this leakage is by inserting a quarter wavelength metallic box to enclose this slot [19].
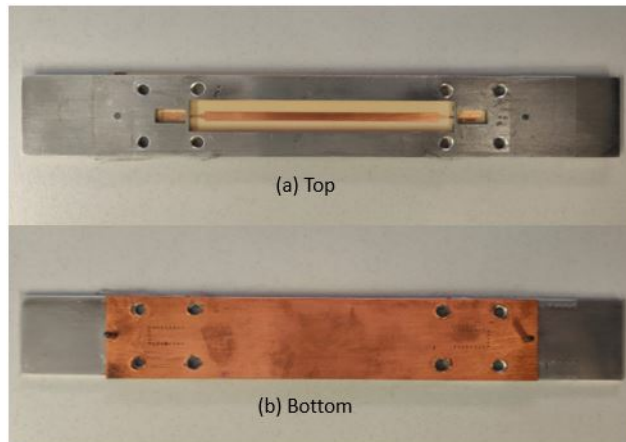

(a)Top-Side   (b) Bottom-Side
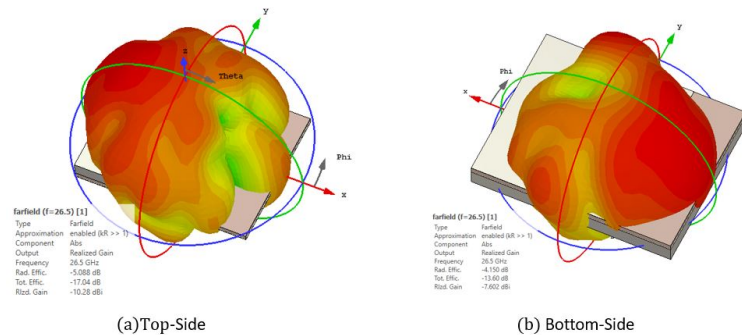
Figure 7. Simulated radiation leakage for the nominal case for both (**a**) TS and (**b**) BS transitions.

The TS transition shows better input reflection coefficients, insertion losses, and radiation leakage performance.

4. Assembly and Measurements

A B2B transition was designed and manufactured at the UPC facilities for both TS and BS designs. The PCB was fabricated using the standard photolithography technique, and the RW assembly connection was manufactured using a CNC milling machine (see Figures 8 and 9). The two designs were measured with the vector network analyzer ZNB-40 from Rohde-Schwarz.

In Figures 10 and 11, the 73 mm long B2B input reflection coefficient and IL from both simulations and measurements are shown for TS and BS designs, respectively. There is a good correlation between the simulations and measurements; for the case of TS transition the design offers a measured -10 dB bandwidth ranging from 24.25 GHz to 30 GHz (FBW of 21.2%) with a little portion of mismatched band ranging from 26.35 GHz to 26.65 GHz at just -9.5 dB and a maximum B2B IL of 1.35 dB, which is 0.67 dB (half) for a single transition. Note that the IL does not take into account the propagation losses (1.3 dB for the 73 mm long ML), as it was already taken away from both simulation and measurement plots. This portion of slightly mismatched frequencies is due to a positional error of the holes that are used to attach the WR-34 to the transition; obviously, the results would be much better if, instead of a B2B transition, a direct single ML-RW transition was used to be measured.

Figure 8. Top view and bottom view of the B2B manufactured TS transition.
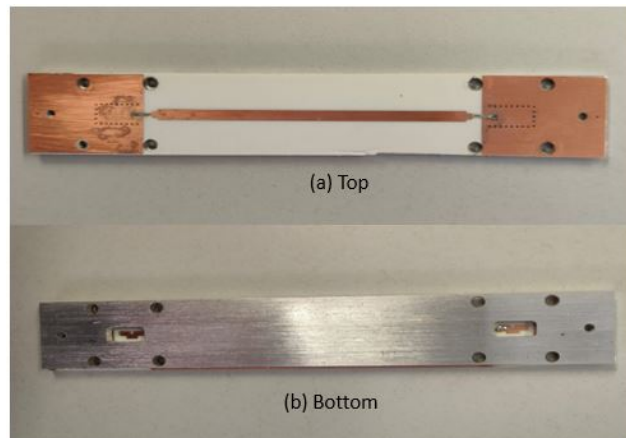

Figure 9. Top view and bottom view of the B2B manufactured BS transition.

For the case of BS transition, the design offers a measured -10 dB bandwidth ranging from 24.6 GHz to 31 GHz (FBW of 23%) and a maximum IL of 1.7 dB, which is 0.85 dB for a single transition. This IL is worse than the simulated one because of slight manufacturing errors, as seen in the previous section, BS is less robust than TS.

Clearly, the TS offers much better and stable IL along the frequency band of operation. Although for both cases there is a small portion of slightly mismatched frequencies around the central frequency point, the TS design is a preferred option in terms of IL, simpler manufacturing process, and robustness to fabrication errors.
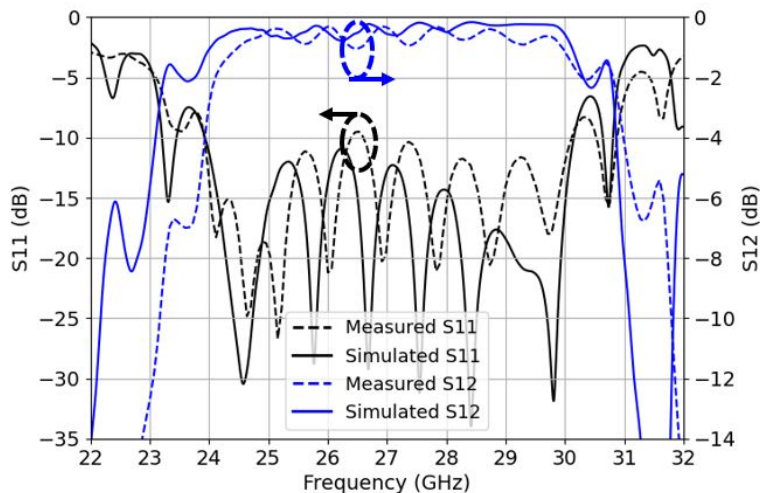
Figure 10. Top-side back-to-back S11 reflection coefficients (left y-axis) in black and insertion losses S12 (right y-axis) in blue for the measurements and simulations.
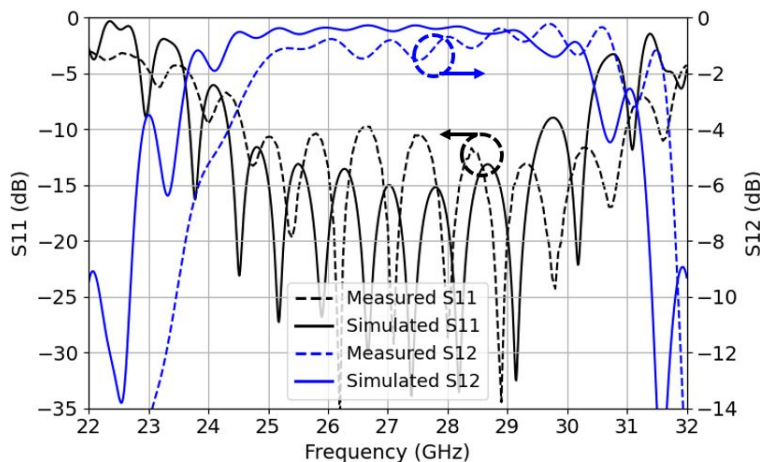
Figure 11. Bottom-side back-to-back S11 reflection coefficients (left y-axis) in black and insertion losses S12 (right y-axis) in blue for the measurements and simulations.

5. Comparison with Other Work

Table 3 shows the comparison with other related work. There are mainly three types of transitions as described in the introduction: inline, BS and TS. The wall column refers to the feeding of the ML through the RW, whereas the back-short column refers to whether a back-shorting cavity is needed. Inline transitions [8] provide much higher FBW (33.3%) with low IL (0.6 dB) with the cost of having to manufacture the RW in two separate pieces as the ML is inserted along the axis of the RW, so it remains floating inside the RW, which requires solid substrates. Although it has brilliant performance, the direction of propagation of the fields along the RW is aligned with the one in the ML, which may not be useful depending on the design requirement.

Table 3. Similar work that can be found showing the comparison of B2B parameters like minimum IL, maximum IL, FBW, and the operating band.

Work	Type	Wall	Max IL	FBW	Band	Backshort
[8]	Inline	Aligned	0.6 dB	33.3%	Ka	Yes
[10]	BS	Broad	NA	18%	W	No
[14]	BS	Narrow	0.7 dB	7.5%	W	No
This Work BS	BS	Narrow	0.85 dB	23%	LMDS, Ka	No
[15] (A)	TS	Narrow	1 dB	15%	W	No
[15] (B)	TS	Narrow	1.1 dB	11%	W	No
[16]	TS	Narrow	NA	11%	W	No
This Work TS	TS	Narrow	0.67 dB	21.2%	LMDS, Ka	No

Perpendicularity between the direction of propagation of the fields in the ML and the RW are often required, making the designs easier to manufacture, for example, horn antennas that are usually placed above the PCB. That is why TS and BS transitions may be preferred. In [10], a broad wall BS transition was designed with an FBW of 18%, but it is bulky in the transversal direction of the ML, which may be inconvenient for many applications related to phased arrays, for example. TS or BS narrow wall transitions are mainly limited by the bandwidth. The highest one found in the literature reaches only up to 15% of FBW for the TS and only 7.5% for the BS. In both designs of our work, we achieved a much higher FBW, 21.2% and 23%, respectively. Although for the BS case, the IL is just 0.15 dB worse, the TS case is greater for both IL and FBW.

6. Conclusions

A novel waveguide to microstrip transition using an array of three overlapped patches has been designed for its integration with the RF chipset. Two designs were designed and manufactured using the same principle for both TS and BS integration. The TS B2B transition offers a measured 21.2% of FBW with a maximum single transition IL of up to 0.67 dB. The BS B2B transition offers 23% of FBW with a maximum single transition IL of up to 0.85 dB. Both TS and BS transitions offers a similar input reflection coefficient, but a higher radiation leakage is found for the BS (2.7 dB more).

The transition is suitable to be used for the whole LMDS and K-band for 5G millimeter-wave applications requiring low cost and high bandwidth for the integration of circuits/antennas requiring RW interfaces, or RW-antennas requiring feeding from ML, such as horn antennas.

Author Contributions: Conceptualization, I.Z.; methodology, I.Z. and J.R.R.; validation, I.Z. and J.R.R.; formal analysis, I.Z. and J.R.R.; resources, I.Z. and J.R.R.; data acquisition, I.Z; funds acquisition, J.R.R.; writing—original draft preparation, I.Z. and J.R.R.; writing—review and editing, I.Z. and J.R.R. All authors have read and agreed to the published version of the manuscript.

Institutional Review Board Statement: Not applicable.

Informed Consent Statement: Not applicable.

Data Availability Statement: Not applicable.

Conflicts of Interest: The authors declare no conflict of interest.

References

1. Liu, D.; Gaucher, B.; Pfeiffer, U.; Grzyb, J. *Advanced Millimeter-Wave Technologies: Antennas, Packaging and Circuits*; Wiley: Hoboken, NJ, USA, 2009.
2. Wang, X.; Kong, L.; Kong, F.; Qiu, F.; Xia, M.; Arnon, S.; Chen, G. Millimeter Wave Communication: A Comprehensive Survey. *IEEE Commun. Surv. Tutor.* **2018**, *20*, 1616–1653. [CrossRef]
3. Zhou, I.; Jofre, L.; Romeu, J. Technology Assessment of Aperture Coupled Slot Antenna Array in Groove Gapwaveguide for 5G Millimeter Wave Applications. *IEEE Access* **2021**, *9*, 139556–139564. [CrossRef]
4. Sifat, S.M.; Shams, S.I.; Kishk, A.A. Integrated Multilayer Horn Antenna for Millimeter-Wave Application. In Proceedings of the 2020 IEEE International Symposium on Antennas and Propagation and North American Radio Science Meeting, Toronto, ON, Canada, 5–10 July 2020; pp. 1433–1434. [CrossRef]
5. Pérez-Escudero, J.M.; Torres-García, A.E.; Gonzalo, R.; Ederra, I. A Gap Waveguide-Based Compact Rectangular Waveguide to a Packaged Microstrip Inline Transition. *Appl. Sci.* **2020**, *10*, 4979. [CrossRef]
6. Seo, K. Planar Microstrip-To-Waveguide Transition in Millimeter-Wave Band. In *Advancement in Microstrip Antennas with Recent Applications*; IntechOpen: London, UK, 2013. Available online: https://www.intechopen.com/chapters/43413 (accessed on 10 March 2013). [CrossRef]
7. Pérez-Escudero, J.M.; Torres-García, A.E.; Gonzalo, R.; Ederra, I. A Simplified Design Inline Microstrip-to-Waveguide Transition. *Electronics* **2018**, *7*, 215. [CrossRef]
8. Li, J.; Li, L.; Qiao, Y.; Chen, J.; Chen, J.; Zhang, A. Full Ka Band Waveguide-to-Microstrip Inline Transition Design. *J. Infrared Millimeter Terahertz Waves* **2018**, *39*, 714–722. [CrossRef]
9. Seo, K.; Sakakibara, K.; Kikuma, N. Microstrip-to-waveguide transition using waveguide with large broad-wall in millimeter-wave band. In Proceedings of the 2010 IEEE International Conference on Ultra-Wideband, Nanjing, China, 20–23 September 2010; pp. 1–4. [CrossRef]
10. Tuan, N.T.; Sakakibara, K.; Kikuma, N. Bandwidth Extension of Planar Microstrip-to-Waveguide Transition by Via-Hole Locations at Both Sides of Microstrip Line. In Proceedings of the 2019 IEEE International Symposium on Antennas and Propagation and USNC-URSI Radio Science Meeting, Atlanta, GA, USA, 7–12 July 2019; pp. 673–674. [CrossRef]
11. Wu, C.; Zhang, Y.; Xu, Y.; Yan, B.; Xu, R. Millimeter-Wave Waveguide-to-Microstrip Transition with a Built-In DC/IF Return Path. *IEEE Trans. Microw. Theory Tech.* **2021**, 69, 1295–1304. [CrossRef]
12. Ishikawa, Y.; Sakakibara, K.; Suzuki, Y.; Kikuma, N. Millimeter-Wave Topside Waveguide-to-Microstrip Transition in Multilayer Substrate. *IEEE Microw. Wirel. Components Lett.* **2018**, *28*, 380–382. [CrossRef]
13. Sakakibara, K.; Nguyen, T.; Kikuma, N.; Hori, T. Bandwidth Comparison of Topside Waveguide-to-Microstrip Transitions with Back-Short Waveguide and with Double-Layer Substrate in Millimeter-Wave Band. In Proceedings of the 2019 13th European Conference on Antennas and Propagation (EuCAP), Krakow, Poland, 31 March–5 April 2019; pp. 1–4.
14. Seo, K.; Kikuma, N. Narrow-wall-connected microstrip-to-waveguide transition using v-shaped patch element in millimeter-wave band. *IEICE Trans.Commun.* **2010**, *E93-B*, 2523–2530. [CrossRef]
15. Topak, E.; Hasch, J.; Zwick, T. Compact Topside Millimeter-Wave Waveguide-to-Microstrip Transitions. *IEEE Microw. Wirel. Components Lett.* **2013**, *23*, 641–643. [CrossRef]
16. Tong, Z.; Stelzer, A. A Vertical Transition Between Rectangular Waveguide and Coupled Microstrip Lines. *IEEE Microw. Wirel. Components Lett.* **2012**, *22*, 251–253. [CrossRef]
17. Kaupp, H.R. Characteristics of Microstrip Transmission Lines. *IEEE Trans. Electron. Comput.* **1967**, *EC-16*, 185–193. [CrossRef]
18. Dybdal, R.B.; Peters, L.; Peake, W.H. Rectangular Waveguides with Impedance Walls. *IEEE Trans. Microw. Theory Tech.* **1971**, *19*, 2–8.
19. Deguchi, Y.; Sakakibara, K.; Kikuma, N.; Hirayama, H. Millimeter-wave microstrip-to-waveguide transition operating over broad frequency bandwidth. In Proceedings of the IEEE MTT-S International Microwave Symposium Digest, Honolulu, HI, USA, 17 June 2005; pp. 2107–2110. [CrossRef]

7.3   [IZ-III]

UltraWideband Microstrip to Waveguide Transition for 5G MillimeterWave Applications

Ivan Zhou[1], Jordi Romeu[2]

[1] (Affiliation): Department of Signal Theory, UPC, Barcelona, Spain, ivanzhoutecno2na@gmail.com*

[2] (Affiliation): Department of Signal Theory, UPC, Barcelona, Spain, romeu@tsc.upc.edu*

Abstract—**In this paper, an ultrawideband microstrip to narrow wall waveguide transition operating at the E-Band is presented. The transition is based on exciting a microstrip folded dipole which radiates into the waveguide. The back-to-back transition provides a fractional bandwidth (FBW) of 20% and measured insertion losses (IL) ranging from 0.65dB to 1.35dB in the whole band of operation.**

Index Terms—**antennas, transitions, 5G millimeter wave.**

I. INTRODUCTION

The fifth generation (5G) millimeter-wave (mmWave) communication is a promising solution to provide high data speed, low latency, and network efficiency. However, although a higher frequency allocation comes with inherent greater bandwidth to face the demand on network capacity, the propagation losses will also increase limiting the coverage area of 5G wireless networks. New architectures involving densification of small-cell are required to face the above-mentioned problems such as backhaul systems, responsible for sending data traffic from the radio access to the backbone segment. 5G mmWave band comprises the FR2 band, with frequencies ranging from 24.25GHz to 48.2 GHz. However, the FR2 band for the latter one is not sufficient to deliver today's capacity peaks [3], offloading to E-band (71-76GHz and 81- 86GHz) spectrum is taking place.

In this regard, high gain and wideband antennas are required to face the 5G mmWave demands. Microstrip antennas are an attractive solution owing to its compactness, increasing the demand for waveguide-to-microstrip transitions to provide an effective connection between microstrip devices and the antenna feeds which are commonly designed in waveguide structures.

In this context, [1] proposed a backshort-less microstrip to waveguide transition via proximity coupling through a patch antenna, although it offers good fractional bandwidth (FBW) of 18.2%, it is fed from the broad-wall of the waveguide which may be an inconvenient if a feeding of more than two $\lambda/2$ spaced arrays is required. Narrow wall waveguides to microstrip transitions are advantageous due to the compactness in the transversal direction of the excitation port and can be classified into top-side or bottom-side depending on the location of the transition element. For the case of top side narrow wall transitions, in [2] the waveguide is excited through a transversal patch antenna; however, intrusion elements inside the waveguide have to be inserted in order to

enhance the bandwidth from 11% to 15%. This intrusion element is avoided in [3] by using a patch fed through a coupled microstrip line.

When regarding bottom-side transitions, all the RF components can be placed below the substrate, with a high reduction of the interference. In [4] a V-shaped transition is shown, although it avoids the implementation of a backshorting cavity, only 4.1% of FBW is achieved. By using a magnetic coupling semiring the FBW can be enhanced up to 35%; however, insertion losses up to 1.94dB are achieved.

In comparison with the transitions presented in this paper, a bottom side narrow wall microstrip to waveguide transition is designed by using a folded dipole antenna, offering lower insertion losses (peak of 1.35 dB) and huge FBW (20%) covering the whole 72.75 GHz - 89.5 GHz for 5G mmWave backhaul applications.

A. Transition Design

The transition was designed on a 0.25mm thick RO3003C substrate, with the standard rectangular waveguide WR-10 (1.55 mm x 3.1 mm) as an excitation port. The other port
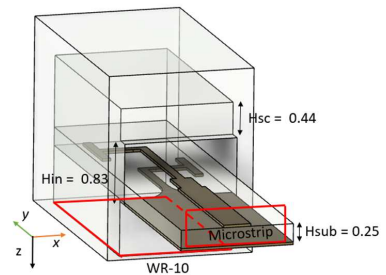

Fig 1. Isometric view

consists in a microstrip line of Wm width, with a quarter wavelength matching step of Wl x Ll. The entrance of the microstrip line is done by a rectangular hole of dimensions Wwr x Hin. A quarter wavelength backshorting metallic box

was designed to prevent leakage from the transition. There is a T-shaped dipole antenna with folded arms of Lt x Win and Ydip x Win, as a half-wavelength dipole antenna would be
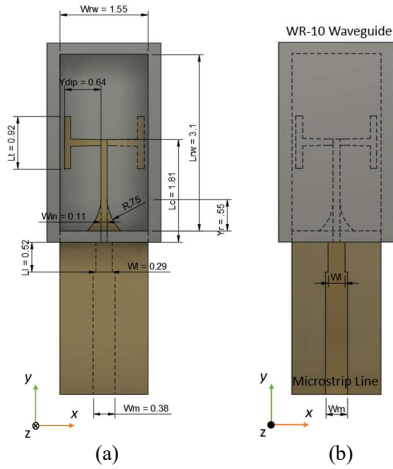

Fig 2. (a) Top and (b) Bottom view of the transition. Discontinuous lines are showing the out of sight parts of the structure.

too large along the narrow wall of the waveguide. A balun consisting of a tapering in the ground plane is used to symmetrize the currents on both arms. The tapering was optimized by adjusting the curvature radius R and the center of this curvature Yr.

B. Antenna

A series fed transversal polarized patch array was also added to the microstrip transition to fully validate its functionality.
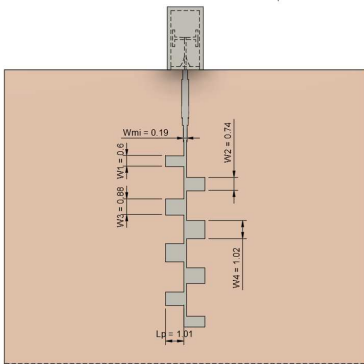

Fig 3. Series fed array design with the transition

The array consists in eight $\lambda_g/2$ (0.92 mm) spaced patch antennas, with total length of Lp and symmetrical width distribution (W1,W2,W3 and W4). The widths and length were optimized to provide the maximum bandwidth while offering a decent realized gain.

II. RESULTS

A back-to-back assembly consisting of a transmission line of 160 mm long was manufactured using standard techniques to check the insertion losses of the transition.
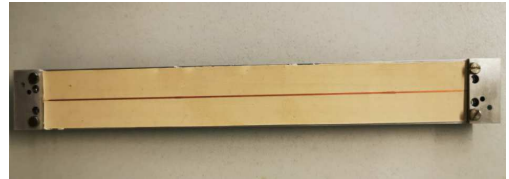
(a)

(b)

Fig 4. Manufactured back-to-back transition. (a) with the backshorting and (b) without backshorting.

As we can see in fig 5, there is a good correlation between the simulated results and the measured results. The losses due to the transmission line are excluded from both simulated and measured results. Even that, the measured insertion losses are worse than the simulated ones due to the losses on the copper ,the limited manufacturing precision and the insertion losses of the WR-10.
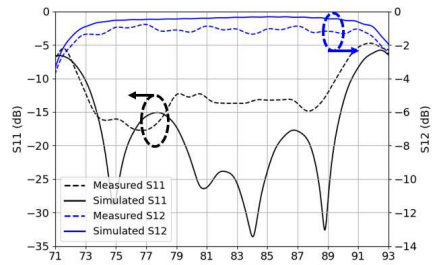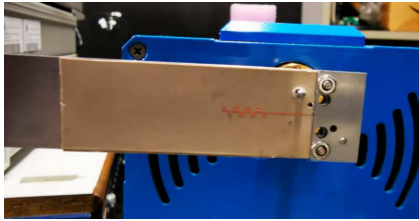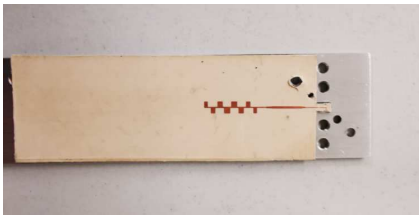

Fig 5. Comparison between the measured (--) and simulated (-) S-Parameters

The transition is well matched in the whole 72.75 GHz – 89.5 GHz providing a measured FBW of 20%. The series fed antenna including the transition to WR-10 was also manufactured at the UPC facilities, its radiation pattern was measured in a 3x3x3 m^3 room where a frequency gating

(a)

(b)

Fig 6. Manufactured antenna mounted over the transition. (a) with backshorting and (b) without backshorting.

postprocessing algorithm was applied to retrieve the radiation pattern without the interference of the reflections inside the room. The antenna was designed to work in the 76.5 GHz – 87 GHz band with a realized gain of 11dB. There is a good correlation between the simulated and measured input reflection coefficient. However, there are few bands that are mismatched (above -10dB) caused by the precision of the manufacturing process.
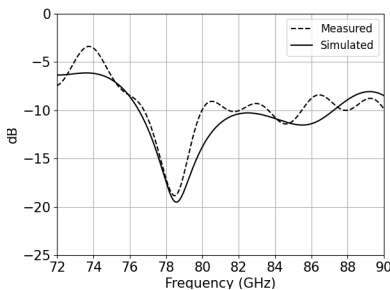

Fig 7. Input Reflection coefficient of the antenna including the transition

The measured radiation patterns for both H-plane and E-plane show less realized gain due to the insertion losses of the transition. Up to 0.8dB of gain penalty were achieved.
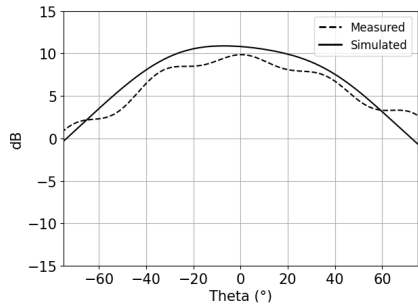

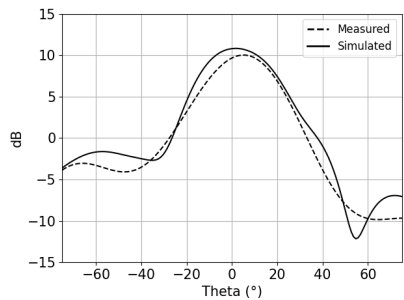Fig 8. E-plane radiation pattern cut

Fig 9. H-plane radiation pattern cut

III. CONCLUSIONS

A simple compact ultrawideband microstrip to waveguide transition was designed and validated in the lab. The transition works in the whole 72.75 GHz – 89.5 GHz band offering a FBW of 20%, with an insertion loss peak of 1.35dB and minimum of 0.65dB at the central frequency of operation (81.12 GHz). The transition was further validated using a microstrip antenna and a gain penalty of up to 0.8dB was noticed in the measurements.

This transition is a promising solution for the next E-Band backhaul systems as high-powered devices are supported mainly by waveguide connectors.

REFERENCES

[1] K. Seo, K. Sakakibara and N. Kikuma, "Microstrip-to-waveguide transition using waveguide with large broad-wall in millimeter-wave band," 2010 IEEE International Conference on Ultra-Wideband, 2010, pp. 1-4, doi: 10.1109/ICUWB.2010.5614169.K. Elissa, "Title of paper if known," unpublished.

[2] E. Topak, J. Hasch and T. Zwick, "Compact Topside Millimeter-Wave Waveguide-to-Microstrip Transitions," in IEEE Microwave and Wireless Components Letters, vol. 23, no. 12, pp. 641-643, Dec. 2013, doi: 10.1109/LMWC.2013.2284824.

[3] Z. Tong and A. Stelzer, "A Vertical Transition Between Rectangular Waveguide and Coupled Microstrip Lines," in IEEE Microwave and Wireless Components Letters, vol. 22, no. 5, pp. 251-253, May 2012, doi: 10.1109/LMWC.2012.2192719.

[4] K. Seo, K. Sakakibara and N. Kikuma, "Narrow-Wall-Connected Microstrip-to-Waveguide Transition Using V-Shaped Patch Element in Millimeter-Wave Band," IEICE Trans. Commun., vol. E93-B, no. 10, pp. 2523-2530, Oct. 2010.

[5] J. Li, J. Xu and J. Fu, "A full Ka-band microstrip-to-waveguide transition using side-inserted magnetic coupling semicircular ring," WAMICON 2012 IEEE Wireless & Microwave Technology Conference, 2012, pp. 1-6, doi: 10.1109/WAMICON.2012.6208434.

7.4   [IZ-IV]

Article

Microstrip-Fed 3D-Printed H-Sectorial Horn Phased Array

Ivan Zhou [1,*], Lluís Pradell [1], José Maria Villegas [2], Neus Vidal [2], Miquel Albert [1], Lluís Jofre [1] and Jordi Romeu [1]

1   School of Telecommunication Engineering, Universitat Politècnica de Catalunya, 08034 Barcelona, Spain; lluis.pradell@upc.edu (L.P.); miquel.albert@estudiantat.upc.edu (M.A.); luis.jofre@upc.edu (L.J.); jordi.romeu-robert@upc.edu (J.R.)
2   Department of Electronics and Biomedical Engineering, Universitat de Barcelona, 08028 Barcelona, Spain; j.m.lopez_villegas@ub.edu (J.M.V.); nvidal@ub.edu (N.V.)
*   Correspondence: ivan.zhou@upc.edu; Tel.: +34-934016826

Abstract: A 3D-printed phased array consisting of four H-Sectorial horn antennas of 200 g weight with an ultra-wideband rectangular-waveguide-to-microstrip-line transition operating over the whole LMDS and K bands (24.25–29.5 GHz) is presented. The transition is based on exciting three overlapped transversal patches that radiate into the waveguide. The transition provides very low insertion losses, ranging from 0.30 dB to 0.67 dB over the whole band of operation (23.5–30.4 GHz). The measured fractional bandwidth of the phased array including the transition was 20.8% (24.75–30.3 GHz). The antenna was measured for six different scanning angles corresponding to six different progressive phases α, ranging from 0° to 140° at the central frequency band of operation of 26.5 GHz. The maximum gain was found in the broadside direction $\alpha = 0°$, with 15.2 dB and efficiency $\eta = 78.5\%$, while the minimum was found for $\alpha = 140°$, with 13.7 dB and $\eta = 91.2\%$.

Keywords: printed antennas; 3D antennas; horns; low-loss antennas; 5G millimeter-wave antennas

1. Introduction

Fifth generation (5G) millimeter-wave (mmWave) communication is a promising solution to the problem of the demand on network capacity, providing low latency and high data speed. However, higher propagation losses will also be introduced, requiring beamforming capabilities [1] for the transmitters in order to mitigate these effects [2].

The availability of chip beamformers [3] at these frequencies makes microstrip line (ML)-based circuitry the optimum solution for the implementation of RF electronics. This is not the best choice for antenna design, due to the propagation losses inside the substrate of an ML. Investigations in [4,5] revealed that the ML is more suitable for feeding arrays of a small or medium size, because the existence of the inevitable dielectric loss in substrates limits the antenna gain. It is therefore necessary to have an alternative technology for designing high-gain antennas that can easily be integrated into beamforming chips.

In this regard, horn antennas are proposed, where the gain can be increased by enlarging the radiating aperture and the costs and weights can be reduced by using additive manufacturing techniques such as 3D printing [6]. There are multiple printing methods, such as selective laser sintering (SLS) [7], where a laser selectively sinters the particles of a polymer powder, fusing them together and building a part layer by layer; fused deposition modeling (FDM) [8], where molten plastic is extruded from a computer-controlled hot-end and cooled to form a part; stereolithography (SLA) [9], where a light source is used to selectively harden photo-activated resins; material jetting (MJ) [10], where the printheads are used to deposit a liquid photoreactive material onto a build platform layer upon layer; and direct metal laser sintering (DMLS) [11], similar to FDM but with a metallic powder. In [12], a fully 3D-printed complex corporate feeding network with 256 horns was successfully manufactured using DMLS, but the cost was high. Many cost-effective horn antenna designs have been produced using FDM [13–15], but although they

represent a large variety of applications and a successful manufacturing process, transitions from the horn to the ML (equivalent to RW–ML transitions) are usually required to provide an effective connection with the RF chipset, and this has not yet been reported in any research.

In this context, a backshort-less ML-to-RW transition via proximity coupling through a patch antenna was proposed [16,17]. Although it offers a good fractional bandwidth (FBW) of 18% by controlling the via holes, it is fed from the broad wall of the RW, which is not convenient because compact $\lambda_g/2$-spaced arrays cannot be implemented. Transitions from the narrow wall of the RW to the ML are advantageous, due to the compactness in this transversal direction with respect to the excitation port. In [18], the RW is excited through a transversal patch antenna. However, intrusion elements inside the RW must be inserted in order to enhance the bandwidth from 11% to 15%, increasing the fabrication complexity. The need for intrusion elements is avoided in [19] by using a V-shaped aperture-coupled patch. Although this avoids the implementation of a back-shorting cavity, only a 7.5% FBW is achieved. In [20], the FBW is increased up to 11% through a patch fed by a coupled ML. In comparison with the transitions presented in this paper [16,18–20], a top–side narrow-wall ML-to-RW transition is designed by using three overlapped transversal patches, offering very low insertion loss (IL) (maximum peak of 0.67 dB) and a very wide FBW (22.5%), covering the whole 23.5–30.4 GHz range for 5G mmWave LMDS and K bands. The presented transition is integrated into (and used to validate) a 3D-printed phased array (PA) using the MJ technique of H-sectorial horn antennas, with a novel corrugated layer that reduces the blind scanning problem and a simple metallization procedure consisting of only covering the outside part of the horns, making the PA ready to be integrated with any RF chipset. This has not been reported in any previous research. The measured results prove the feasibility of the 3D-printing technology for manufacturing complex active antenna systems such as PAs.

2. Transition Design

The focus of this first section is on the conversion of the Q-TEM mode of a 50 Ω ML to the TE_{10} mode of a WR-34 (with dimensions $W_{rw} \times L_{rw}$) located on the same side of the substrate as the ML, so that it can later be used to feed an array of four $\lambda_g/2$-spaced H-sectorial horn antennas using an ML. Figure 1 shows the top view of the transition, Figure 2 shows its isometric view and Table 1 shows the dimensions of the transition. The transition is designed using a 0.81 mm thick RO4003 substrate of Er = 3.55 and tan δ = 0.0027. A full-wave electromagnetic simulation tool, CST Microwave Studio, was used for its optimization. In order to excite the TE_{10} mode from the RW, the excitation of transversal currents in the $\hat{x}$ direction is required. An array of three overlapped transversal patches, as proposed in [21], was used. The length Lp of the patches, the width W_p, the inter-element distance d_y and the array position with respect to the entrance of the RW y_0 were jointly optimized to provide
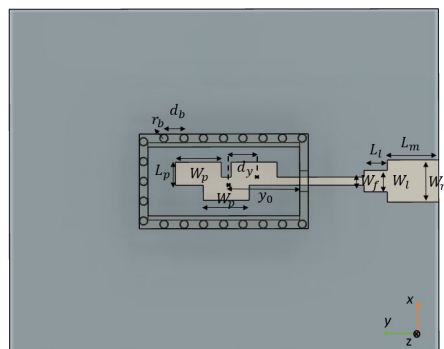

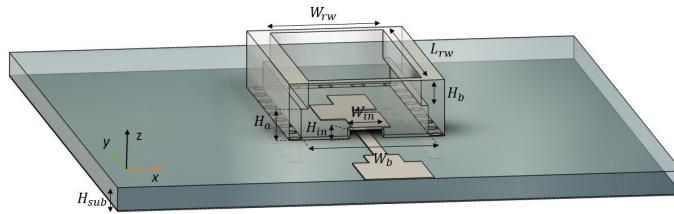**Figure 1.** Top view of the transition.

Figure 2. Isometric view of the transition.

Table 1. Dimensions in mm of each designed parameter.

H_{sub}	0.81	W_f	0.47	W_{rw}	4.2	r_b	0.25
dy	1.5	W_l	1.1	L_{rw}	8.8	d_b	1.17
W_p	2.75	L_l	1.35	H_b	1	H_{in}	0.5
L_p	1.3	L_m	2.5	H_a	2	W_{in}	1.2
Y_0	4.48	W_m	2.55	W_b	4.5		

maximum bandwidth while maintaining minimum IL. Re-optimization of the transition was carried out when integrating it with the 3D-printed PA shown in the next section. The overlapping of these patches of length $0.2\lambda_g$ is crucial for the excitation of transversal $J\hat{x}$ currents. The array is fed by an ML of width W_f and is matched to a 50 Ω circuit with a stepped section of dimensions $W_t \times L_t$. The input to the RW has dimensions Win x Hin, and ideally these should be as small as possible to avoid leakage from the RW, while also preventing short-circuiting with the ML. The final dimension was chosen considering the manufacturing feasibility.

The narrow wall of the RW is stepped (see Figure 2) from dimensions $Wb \times Lrw \times Ha$ to $Wrw \times Lrw \times Hb$, so that the dimensions of the H-sectorial horn antenna along the $\hat{x}$ direction can be reduced for the integration of a mutual coupling reduction (MCR) layer, which is introduced in Section 3. In Figure 3, we show the simulated S-parameters of the ML–RW transition. We can observe a good -10 dB input reflection coefficient ranging from 23.5 GHz to 30.4 GHz. Note that this transition was optimized jointly with the 3D-printed PA above it.
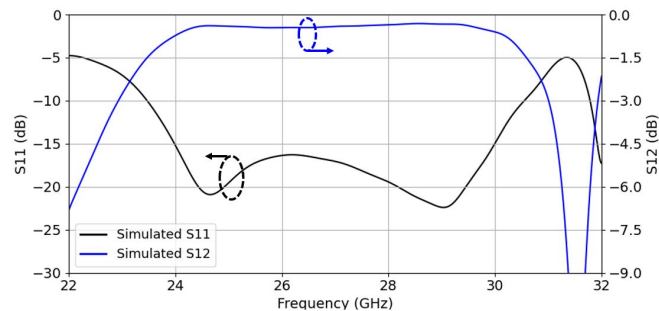

Figure 3. S-parameters of the single transition.

3. Phased Array Design

In Figure 4, an exploded view of the whole microstrip-fed 3D-printed PA of four active H-Sectorial horns is shown. The antenna was designed to be attached through four

2.4 mm coaxial cables to the F5288 digital beamformer from RENESAS, achieving four active channels. It is composed of five different layers, *L*0, *L*1, *L*2, *L*3 and *L*4. The first layer *L*0 consists of four 2.4 mm female connectors attached to the ML printed on the RO4003C substrate, which are used to feed the ML–RW transition presented in Section 2. The distance between the connectors and the transition is 25 mm. Layer *L*1 is a horn coupler that attaches layer *L*0 to layer *L*2. In turn, *L*2 is a support for six H-sectorial horns, implemented on layer *L*3 through two M2.5 screwed holes. Although a direct chip-to-ML integration would be a more elegant option to reduce design complexity and bulkiness, as well as cable losses, this was not the main goal of this research. The main goal was to demonstrate the feasibility of 3D-printing technology for manufacturing complex antenna systems such as PAs.
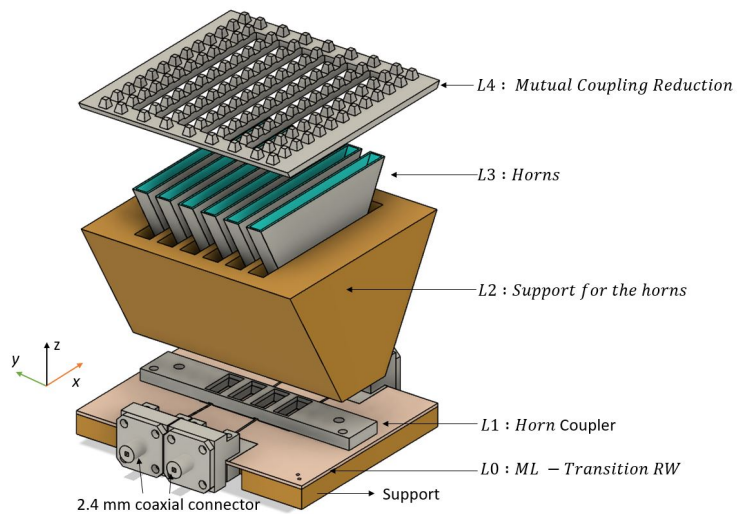
Figure 4. Exploded view of the whole design.

Only four horns are active, with two lateral dummies placed on the sides of the phased array in order to symmetrize the radiation pattern. The top *L*4 layer consists of a periodic arrangement of nails to reduce the mutual coupling (MC) between each horn antenna. Thus, the blind scanning issue is minimized, maintaining a −10 dB matching of all the four active horns for a wide range of scanning angles related to a progressive phase, ranging from 0° to 140°. The support, *L*1, *L*2, *L*3 and *L*4 were fully 3D-printed with an Objet Connex 1 printer from Stratasys, using the material jetting technique, with a tolerance of ±0.05 mm on the Z axis and ±0.1 mm on the X and Y axes. The photosensitive resin ink was High Temperature RGD525, with an electrical permittivity of E_r = 2.95 and a loss tangent of 0.0175. All the printed materials except *L*2 were metallized using copper electrodeposition.

3.1. Horn Antenna

Six H-sectorial horns were designed and 3D-printed, with dimensions as shown in Figure 5. The horns had height L_h, width W_h and thickness W_y. The entrance of the horn had width X_W and height X_h, which was optimized in order to maximize the bandwidth of the joint horn and transition design. The inner side of the horn was empty in order to reduce the transmission losses of the EM fields, and the thickness of the walls of each horn was a constant of value W_{wall}.
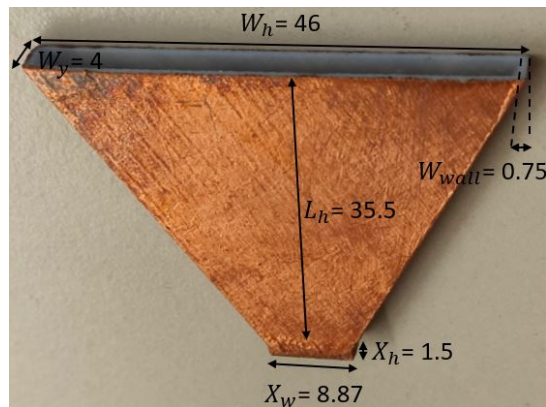
Figure 5. Horn antenna (all dimensions in mm).

Only the outer lateral parts of the horn were metallized using the conventional electrodeposition technique, rather than metallizing both outer and inner parts as is usually the case, increasing the reliability of a complete surface copper deposition process. An optimum metallization setup would be a plastic part whose surfaces are almost parallel to the fields created by the electrodes, so that the particles of copper travel directly to the surfaces and attach to them. This is the case when metallizing the outer part of the horn. However, when metallizing the inner parts of the horn (which was avoided in our case), the deposition of the copper is complicated by the presence of surfaces perpendicular to these fields.

3.2. Mutual Coupling Reduction

A mutual coupling reduction layer $L4$ was designed in order to reduce the well-known blind scanning problem [22] of phased arrays. This layer used periodic nails p_{ycorr} of a trapezoidal shape with a squared bottom shape $W_{Anail} \times W_{Anail}$, top shape $W_{Bnail} \times W_{Bnail}$ and height H_{nail}, see Figure 6. The periodic nails, also known as high-impedance surfaces, are a preferred option compared to $\lambda_g/4$ slits, due to the intrinsic wide-band behaviour.
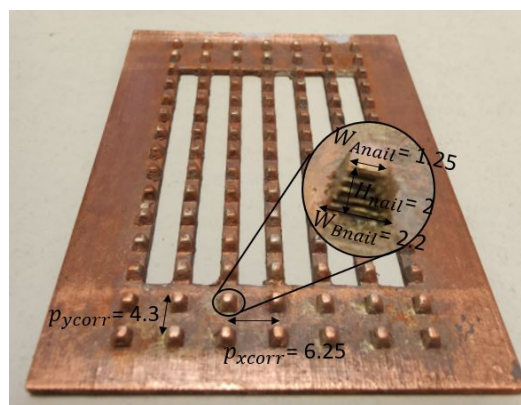

Figure 6. $L4$ layer showing the corrugations used for blind scanning reduction of a phased array.

In order to find the optimal parameters to reduce the blind scanning problem, the MC between adjacent horns must be reduced. By selecting only two horns, each one with a simulation port, it is possible to optimize their dimensions by finding the minimum

coupling between them. In Figure 7, we can see a comparison of the input reflection coefficients (a) without the nails and (b) with nails. For each port of the horn, there are six traces relating to the progressive phase from 0° to 140° at 26.5 GHz. The reason for showing both plots in this compact way is to show that all the ports from the PA are well matched for every scanning angle when using the mutual coupling reduction layer. We can clearly see that port 4 becomes mismatched when a progressive phase along the arrays differs from 0, which will clearly reduce the gain of the beamformer.
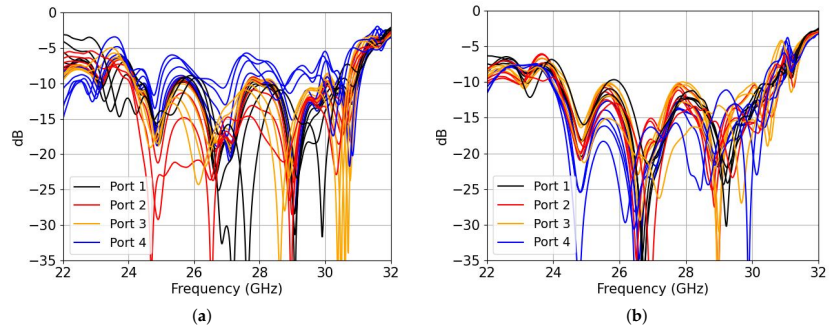
Figure 7. Simulated input reflection coefficients for each port: (**a**) without nails; (**b**) with nails. There are 6 traces per port relating to the progressive phase from 0° to 140° at 26.5 GHz.

4. Results

This section discusses the experimental results for the designed phased array. Figure 8 shows the manufactured and mounted PA connected to the beamformer, Figure 9 shows the results of the input reflection coefficients, Figure 10 shows the scanning pattern only in the azimuthal plane of the PA in dB and Figure 11 shows the phased array gain with respect to the frequency for three different progressive phases. In Figure 9, the input reflection coefficients correspond to each individual port (when measuring one port the rest remain unexcited). Note that measuring the input reflection coefficient of each port when exciting all ports and using the beamformer for scanning in the E-plane was not possible with this setup. The measured input reflection coefficients are all slightly shifted to higher frequency, with a wider bandwidth behaviour and an unexpected resonance at 31.25 GHz. The antenna is wideband in nature as the horn is a non-resonant structure, offering a measured FBW of 20.8%.
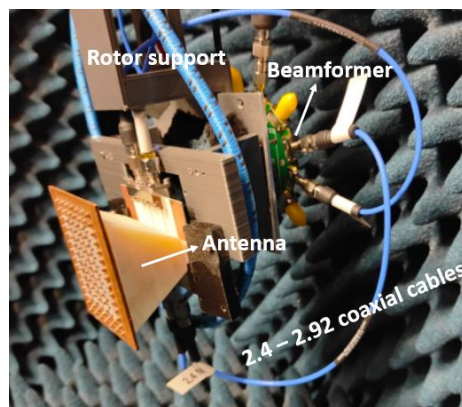
Figure 8. Entire manufactured phased array connected with the beamformer and ready to be measured in the anechoic chamber.

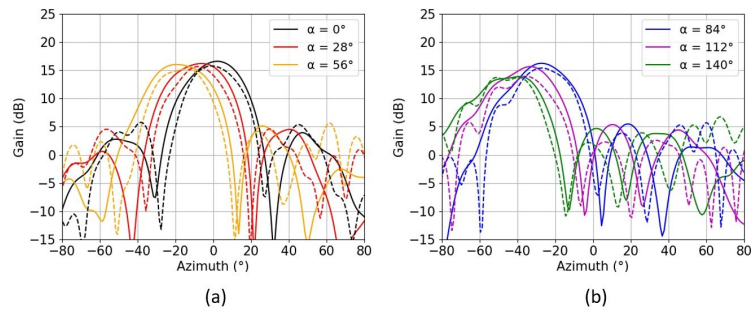Only the radiation pattern in the E-plane was measured for each scanning angle, using the digital beamformer at four different frequencies ranging only from 26.5 GHz to 29.5 GHz, since the beamformer chip was limited to operating only in the LMDS band. Each channel of the beamformer was calibrated as each cable's curvature introduced different phases.
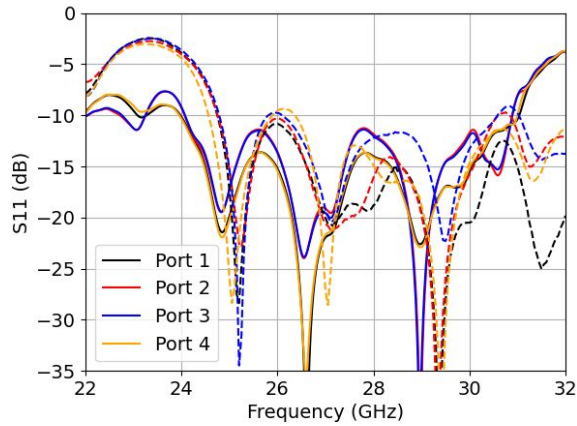
Figure 9. Input reflection coefficient (for measured - - and simulated -) for each port independently.

Figure 10. Radiation pattern in the E-plane (for measured - - and simulated -) for six different progressive phases α ranging from $0°$ to $56°$ (**a**) and from $84°$ to $140°$ (**b**), at 26.5 GHz.

The gain of the phased array was referenced to the measurement of a horn antenna with a 20.8 dB gain connected to one channel of the beamformer. Table 2 shows the measured gain, the simulated directivity and the efficiency of the antenna at the central frequency of 26.5 GHz. The antenna offers a maximum realized gain of 15.2 dB in the broadside direction and a minimum at the maximum $\alpha = 140°$. However, the efficiency is much higher in the latter case, peaking up to 91.2%.

Table 2. Measured realized gain, simulated directivity in dB and efficiency η in % for the six different progressive phases α ranging from $0°$ to $140°$.

α	$0°$	$28°$	$56°$	$84°$	$112°$	$140°$
Gain (dB)	15.2	15.15	15.04	15.05	13.75	13.7
Directivity (dB)	16.25	15.8	15.8	15.74	15.33	14.2
η (%)	78.5	86	83.9	85.3	69.5	91.2

Figure 10 shows the realized gain in the azimuth plane at the central frequency of 26.5 GHz, showing an average value of 1dB less gain than in the simulated case, due to the manufacturing process. The maximum amount of sidelobe level (SLL) was measured to be 12 dB for a progressive phase of 140°, which can be reduced because a uniform distribution among the channels was used along the array. We can see from Figure 11 that there is also a good correlation of the gains with respect to frequency. Only three different progressive phases corresponding to $\alpha = 0°$, 56° and 140° were plotted in order to keep the figure clearer.

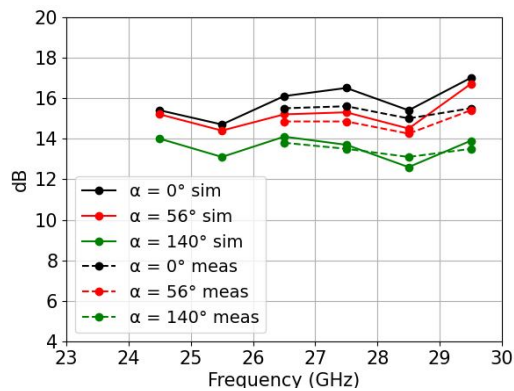**Figure 11.** Realized gain over frequency for three different progressive phases, $\alpha = 0°$, 56° and 140°. Values were measured only from 26.5 GHz to 29.5 GHz due to the limitations of the beamformer.

5. Comparison with Other Work

Table 3 shows a comparison with other studies using 3D-printing technology for horn antennas. There are mainly two types of printing technology, classified as metal or plastic printing. In [12], a 16 × 16 horn array printed using DMLS is considered. Although the complexity is high, it uses metal printing, which increases the fabrication costs. The manufacturing cost and the weight can be considerably reduced by using plastic printing technologies such as the popular FDM. In [13–15], the authors all use the same FDM technique, with copper electrodeposition for the metallization of the whole of the inner and outer plastic parts. However, as the frequency increases and the manufacturing complexity increases, there will be tiny parts that can be very difficult to metallize. In this study, a much simpler metallization procedure was used, so that only the outer part of the horn needed to be metallized, as stated in Section 3.1.

Table 3. Comparison with other studies using 3D printing technology for horn antennas.

Ref.	Gain (dB)	Aperture Size (λ)	Elements	Printing Technique	Bandwidth (GHz)	Chip Integration
[12]	33.8	13 × 13	256	DMLS	28.2–35.8	No
[13]	13.51	1.15 × 1.15	1	FDM	3.5–11.4	No
[14]	18.7	4 × 4	1	FDM	8.2–12.4	No
[15]	20	2.7 × 3.68	1	FDM	25–40	No
This work	15.2	2 × 3.9	4	MJ	24.75–30.3	Yes

In addition, for many upcoming future 5G applications, interconnection between the radiating elements and RF chipsets is required for effective integration with the antenna system. This aspect is reported in this work but not provided in any other 3D-printed horn antenna studies. The gain of the horn antenna is lower than in most of the comparison

studies because the effective aperture is much smaller and the array consisted of only four active H-sectorial horn elements, but it could be increased by adding more active elements or by enlarging the aperture in the H-plane.

6. Conclusions

A 3D-printed phased array of four H-sectorial horns that minimized the blind scanning problem and provided an easier metallization solution was proposed. A microstrip-line-to-rectangular-waveguide transition was designed for the integration of the phased array with a commercial digital beamformer. The transition offered a simulated FBW of 22.5%, with a maximum single-transition IL of up to 0.67 dB and a minimum IL of 0.3 dB. The 3D-printed phased array was used to scan from $0°$ to $140°$ at the central frequency of 26.5 GHz in steps of $28°$, giving a total of six patterns. The measured gain of the array was 15.2 dB for the case of the broadside direction, with a measured FBW of 20.8% for the case of a single-port measurement. The results proved the feasibility of 3D-printing technology for the manufacturing of phased arrays in high-frequency bands and their easy integration with digital beamformers. A future improvement would be to integrate the antenna directly with beamforming chips to avoid the use of coaxial interconnections, which introduce additional losses.

The antenna is suitable for the whole LMDS and K-band for 5G millimeter-wave applications requiring low cost, high gain and integrated solutions.

References

1. Zhou, I.; Ramírez, G.A.; Montero, L.; Blanch, S.; Romeu, J.; Jofre, L. Three-Dimensional Beamsteering Low-Complexity Reconfigurable Multilevel Antenna. *IEEE Antennas Wirel. Propag. Lett.* **2020**, *19*, 1017–1021. https://doi.org/10.1109/LAWP.2020.2986924.
2. Liu, B.D.; Gaucher, U.P.; Grzyb, J. *Advanced Millimeterwave Technologies: Antennas, Packaging and Circuits*; Wiley: Hoboken, NJ, USA, 2009.
3. Kibaroglu, K.; Sayginer, M.; Rebeiz, G.M. A 28 GHz transceiver chip for 5G beamforming data links in SiGe BiCMOS. In Proceedings of the 2017 IEEE Bipolar/BiCMOS Circuits and Technology Meeting (BCTM), Miami, FL, USA, 19–21 October 2017; pp. 74–77. https://doi.org/10.1109/BCTM.2017.8112914.
4. Levine, E.; Malamud, G.; Shtrikman, S.; Treves, D. A study of microstrip array antennas with the feed network. *IEEE Trans. Antennas Propag.* **1989**, *37*, 426–434. https://doi.org/10.1109/8.24162.
5. Cheng, Y.J.; Guo, Y.X.; Liu, Z.G. W-Band Large-Scale High-Gain Planar Integrated Antenna Array. *IEEE Trans. Antennas Propag.* **2014**, *62*, 3370–3373. https://doi.org/10.1109/TAP.2014.2310483.
6. Kamble, P.S.; Khoje, S.A.; Lele, J.A. Recent Developments in 3D Printing Technologies: Review. In Proceedings of the 2018 Second International Conference on Intelligent Computing and Control Systems (ICICCS), Madurai, India, 14–15 June 2018; pp. 468–473. https://doi.org/10.1109/ICCONS.2018.8662981.
7. Lomakin, K.; Pavlenko, T.; Sippel, M.; Gold, G.; Helmreich, K.; Ankenbrand, M.; Urban, N.; Franke, J. Impact of surface roughness on 3D printed SLS horn antennas. In Proceedings of the 12th European Conference on Antennas and Propagation (EuCAP 2018), London, UK, 9–13 April 2018; pp. 1–4. https://doi.org/10.1049/cp.2018.1235.

8. Russo, A.C.; Andreassi, G.; Di Girolamo, A.; Pappadà, S.; Buccoliero, G.; Barile, G.; Vegliò, F.; Stornelli, V. FDM 3D Printing of high performance composite materials. In Proceedings of the 2019 II Workshop on Metrology for Industry 4.0 and IoT (MetroInd4.0 & IoT), Naples, Italy, 4–6 June 2019; pp. 355–359. https://doi.org/10.1109/METROI4.2019.8792862.

9. Gupta; P. Bhat; M. Khamkar; V.Tandel; G. Salunkhe; Gauri. Designing of Cost Effective Resin 3D Printer using UV LED. 2020 International Conference on Convergence to Digital World - Quo Vadis (ICCDW), https://10.1109/ICCDW45521.2020.9318691.

10. Tsai, M.J.; Mei, C.W.; Cheng, Y.L.; Chen, F.; Hu, Z.Y.; Huang, K.C. A study of a material jetting based color 3d printing system by using multiple piezoelectric heads. In Proceedings of the 2017 International Conference on Machine Learning and Cybernetics (ICMLC), Ningbo, China, 9–12 July 2017; Volume 2, pp. 664–669. https://doi.org/10.1109/ICMLC.2017.8108984.

11. Cazden, J.; Boskovic, L.; Lier, E.; Hand, T.; Kefauver, W.N.; Filipovic, D. Performance of SLA and DMLS 3D Printed Ka-Band Resonators with Integrated Coaxial Launchers. In Proceedings of the 2021 51st European Microwave Conference (EuMC), London, UK, 4–6 April 2022; pp. 338–341. https://doi.org/10.23919/EuMC50147.2022.9784234.

12. Li, Y.; Ge, L.; Wang, J.; Da, S.; Cao, D.; Wang, J.; Liu, Y. 3-D Printed High-Gain Wideband Waveguide Fed Horn Antenna Arrays for Millimeter-Wave Applications. *IEEE Trans. Antennas Propag.* **2019**, *67*, 2868–2877. https://doi.org/10.1109/TAP.2019.2899008.

13. Oktafiani, F.; Hamid, E.Y.; Munir, A. Wideband Dual-Polarized 3D Printed Quad-Ridged Horn Antenna. *IEEE Access* **2022**, *10*, 8036–8048. https://doi.org/10.1109/ACCESS.2022.3143164.

14. Goode, I.; Saavedra, C.E. 3D Printed Linearly Polarized X-Band Conical Horn Antenna and Lens. *IEEE Open J. Antennas Propag.* **2022**, *3*, 549–556. https://doi.org/10.1109/OJAP.2022.3173161.

15. Yao, H.; Sharma, S.; Henderson, R.; Ashrafi, S.; MacFarlane, D. Ka band 3D printed horn antennas. In Proceedings of the 2017 Texas Symposium on Wireless and Microwave Circuits and Systems (WMCS), Waco, TX, USA, 30–31 March 2017; pp. 1–4. https://doi.org/10.1109/WMCaS.2017.8070701.

16. Tuan, N.T.; Sakakibara, K.; Kikuma, N. Bandwidth Extension of Planar Microstrip-to-Waveguide Transition by Controlling Transmission Modes Through Via-Hole Positioning in Millimeter-Wave Band. *IEEE Access* **2019**, *7*, 161385–161393. https://doi.org/10.1109/ACCESS.2019.2952073.

17. Ishikawa, Y.; Sakakibara, K.; Suzuki, Y.; Kikuma, N. Millimeter-Wave Topside Waveguide-to-Microstrip Transition in Multilayer Substrate. *IEEE Microw. Wirel. Components Lett.* **2018**, *28*, 380–382.

18. Topak, E.; Hasch, J.; Zwick, T. Compact Topside Millimeter-Wave Waveguide-to-Microstrip Transitions. *IEEE Microw. Wirel. Components Lett.* **2013**, *23*, 641–643. https://doi.org/10.1109/LMWC.2013.2284824.

19. Seo, K.S.K.; Kikuma, N. Narrow-Wall-Connected Microstrip-to-Waveguide Transition Using V-Shaped Patch Element in Millimeter-Wave Band. *IEICE Trans. Commun.* **2010**, *E93-B*, 2523–2530. https://doi.org/10.1587/transcom.E93.B.2523.

20. Tong, Z.; Stelzer, A. A Vertical Transition Between Rectangular Waveguide and Coupled Microstrip Lines. *IEEE Microw. Wirel. Components Lett.* **2012**, *22*, 251–253. https://doi.org/10.1109/LMWC.2012.2192719.

21. Zhou, I.; Romeu, J. Ultra-Wideband narrow wall waveguide-to-microstrip transition using overlapped patches. *Sensors* **2022**, *22*, 2964.

22. Pozar, D.; Schaubert, D. Scan blindness in infinite phased arrays of printed dipoles. *IEEE Trans. Antennas Propag.* **1984**, *32*, 602–610. https://doi.org/10.1109/TAP.1984.1143375.

References

[1] A.L. Merlo. Automotive radar for the prevention of collisions. *IEEE Transactions on Industrial Electronics and Control Instrumentation*, IECI-11(1):1–6, 1964. doi: 10.1109/TIECI.1964.234462.

[2] W.P. Harokopus. Application of radar to automobile control and sensing. In *1971 IEEE GMTT International Microwave Symposium Digest*, pages 168–169, 1971. doi: 10.1109/GMTT.1971.1122950.

[3] J.E. Stevens and L.L. Nagy. A diplex doppler radar automotive obstacle detection system. In *23rd IEEE Vehicular Technology Conference*, volume 23, pages 70–81, 1972. doi: 10.1109/VTC.1972.1622126.

[4] E.F. Belohoubek. Radar control for automotive collision mitigation and headway spacing. *IEEE Transactions on Vehicular Technology*, 31(2):89–99, 1982. doi: 10.1109/T-VT.1982.23918.

[5] Automated driving: Safer and more efficient future driving and automotive radar from its origins to future directions. *BOOK*.

[6] I. Gresham, N. Jain, T. Budka, A. Alexanian, N. Kinayman, B. Ziegner, S. Brown, and P. Staecker. A compact manufacturable 76-77-ghz radar module for commercial acc applications. *IEEE Transactions on Microwave Theory and Techniques*, 49(1):44–58, 2001. doi: 10.1109/22.899961.

[7] H. P. Forstner, H. Knapp, H. Jager, E. Kolmhofer, J. Platz, F. Starzer, M. Treml, A. Schinko, G. Birschkus, J. Bock, K. Aufinger, R. Lachner, T. Meister, H. Schafer, D. Lukashevich, S. Boguth, A. Fischer, F. Reininger, L. Maurer, J. Minichshofer, and D. Steinbuch. A 77ghz 4-channel automotive radar transceiver in sige. In *2008 IEEE Radio Frequency Integrated Circuits Symposium*, pages 233–236, 2008. doi: 10.1109/RFIC.2008.4561425.

[8] Thomas Binzer, Michael Klar, and Volker Gross. Development of 77 ghz radar lens antennas for automotive applications based on given requirements. In *2007*

2nd International ITG Conference on Antennas, pages 205–209, 2007. doi: 10.1109/INICA.2007.4353963.

[9] Christian Waldschmidt, Juergen Hasch, and Wolfgang Menzel. Automotive radar — from first efforts to future systems. *IEEE Journal of Microwaves*, 1(1): 135–148, 2021. doi: 10.1109/JMW.2020.3033616.

[10] E. Fishler, A. Haimovich, R. Blum, D. Chizhik, L. Cimini, and R. Valenzuela. Mimo radar: an idea whose time has come. In *Proceedings of the 2004 IEEE Radar Conference (IEEE Cat. No.04CH37509)*, pages 71–78, 2004. doi: 10.1109/NRC.2004.1316398.

[11] Ivan Zhou, Lluís Jofre, and Jordi Romeu. Technology assessment of aperture coupled slot antenna array in groove gapwaveguide for 5g millimeter wave applications. *IEEE Access*, 9:139556–139564, 2021. doi: 10.1109/ACCESS.2021.3119748.

[12] Ivan Zhou and Jordi Romeu Robert. Ultra-wideband narrow wall waveguide-to-microstrip transition using overlapped patches. *Sensors*, 22(8), 2022. ISSN 1424-8220. doi: 10.3390/s22082964. URL `https://www.mdpi.com/1424-8220/22/8/2964`.

[13] Ivan Zhou and Jordi Romeu. Ultrawideband microstrip to waveguide transition for 5g millimeterwave applications. In *2022 16th European Conference on Antennas and Propagation (EuCAP)*, pages 1–4, 2022. doi: 10.23919/EuCAP53622.2022.9769512.

[14] Ivan Zhou, Lluís Pradell, José Maria Villegas, Neus Vidal, Miquel Albert, Lluís Jofre, and Jordi Romeu. Microstrip-fed 3d-printed h-sectorial horn phased array. *Sensors*, 22(14), 2022. ISSN 1424-8220. doi: 10.3390/s22145329. URL `https://www.mdpi.com/1424-8220/22/14/5329`.

[15] Jianjie Yan, Haiming Wang, Jiexi Yin, Chen Yu, and Wei Hong. Planar series-fed antenna array for 77 ghz automotive radar. In *2017 Sixth Asia-Pacific Conference on Antennas and Propagation (APCAP)*, pages 1–3, 2017. doi: 10.1109/APCAP.2017.8420639.

[16] E. Levine, G. Malamud, S. Shtrikman, and D. Treves. A study of microstrip array antennas with the feed network. *IEEE Transactions on Antennas and Propagation*, 37(4):426–434, 1989. doi: 10.1109/8.24162.

[17] Yujian Li, Lei Ge, Junhong Wang, Shan Da, Di Cao, Jingxue Wang, and Yang Liu. 3-d printed high-gain wideband waveguide fed horn antenna arrays for millimeter-wave applications. *IEEE Transactions on Antennas and Propagation*, 67(5):2868–2877, 2019. doi: 10.1109/TAP.2019.2899008.

[18] Haohan Yao, Shilpi Sharma, Rashaunda Henderson, Solyman Ashrafi, and Duncan MacFarlane. Ka band 3d printed horn antennas. In *2017 Texas Symposium on Wireless and Microwave Circuits and Systems (WMCS)*, pages 1–4, 2017. doi: 10.1109/WMCaS.2017.8070701.

[19] H. Takahashi, T. Kosugi, A. Hirata, J. Takeuchi, K. Murata, and N. Kukutsu. Hermetic sealing technique for f-band waveguides and packages. In *2011 41st European Microwave Conference*, pages 269–272, 2011. doi: 10.23919/EuMC. 2011.6101718.

[20] E. Rajo-Iglesias, M. Ferrando-Rocher, and A. U. Zaman. Gap waveguide technology for millimeter-wave antenna systems. *IEEE Communications Magazine*, 56(7):14–20, 2018. doi: 10.1109/MCOM.2018.1700998.

[21] E. Pucci, E. Rajo-Iglesias, and P. Kildal. New microstrip gap waveguide on mushroom-type ebg for packaging of microwave components. *IEEE Microwave and Wireless Components Letters*, 22(3):129–131, 2012. doi: 10.1109/LMWC.2011. 2182638.

[22] S. Kildal, A. Zaman, E. Rajo, E. Alfonso, and A. Nogueira. Design and experimental verification of ridge gap waveguide in bed of nails for parallel plate mode suppression. *IET Microwaves, Antennas and Propagation*, 2009.

[23] E. Rajo-Iglesias and P. Kildal. Groove gap waveguide: A rectangular waveguide between contactless metal plates enabled by parallel-plate cut-off. In *Proceedings of the Fourth European Conference on Antennas and Propagation*, pages 1–4, 2010.

[24] Z. Shaterian, A. K. Horestani, and J. R. Mohassei. Design of slot array antenna in groove gap waveguide technology. *IET Microwaves, Antennas and Propagation*, 13, 2019.

[25] M. A. K. S. Lubis, C. Apriono, F. Y. Zulkifli, and E. T. Rahardjo. Design of narrow wall slotted waveguide antenna for x-band application. In *2017 Progress in Electromagnetics Research Symposium - Fall (PIERS - FALL)*, pages 2625–2628, 2017. doi: 10.1109/PIERS-FALL.2017.8293579.

[26] D. P. Yusuf, F. Y. Zulkifli, and E. T. Rahardjo. Design of narrow-wall slotted waveguide antenna with v-shaped metal reflector for xband radar application. In *2018 International Symposium on Antennas and Propagation (ISAP)*, pages 1–2, 2018.

[27] T. Uesaka, N. Nakamoto, T. Fukasawa, N. Yoneda, T. Yamamoto, T. Koyanagi, I. Kakimoto, and Y. Konishi. Design of edge-slotted waveguide array antenna manufactured by injection-molding. In *2019 IEEE International*

Symposium on Phased Array System Technology (PAST), pages 1–4, 2019. doi: 10.1109/PAST43306.2019.9020986.

[28] José Ignacio Herranz Herruzo, Alejandro Valero-Nogueira, Sara Martínez Giner, and Antonio Vila Jiménez. Untilted narrow-wall slots excited by parasitic dipoles in groove gap waveguide technology. *IEEE Transactions on Antennas and Propagation*, 63(11):4759–4765, 2015. doi: 10.1109/TAP.2015.2478144.

[29] J. H. Lee, J. M. Lee, K. C. Hwang, D. W. Seo, D. Shin, and C. Lee. Capacitively coupled microstrip comb-line array antennas for millimeter-wave applications. *IEEE Antennas and Wireless Propagation Letters*, 19(8):1336–1339, 2020. doi: 10.1109/LAWP.2020.3001945.

[30] S. Chakrabarty Y. Tyagi, P. Mevada and R. Jyoti. High-efficiency broadband slotted waveguide array antenna. *IET Microw. Antennas Propag.*, 2016.

[31] Z. Talepour, Sh. Esmaili, and A. Khaleghi. Ridge gap waveguide antenna array using integrated coaxial power divider. In *2015 Loughborough Antennas Propagation Conference (LAPC)*, pages 1–5, 2015. doi: 10.1109/LAPC.2015.7366065.

[32] A. Haddadi, C. Bencivenni, and T. Emanuelsson. Gap waveguide slot array antenna for automotive applications at e-band. In *2019 13th European Conference on Antennas and Propagation (EuCAP)*, pages 1–4, 2019.

[33] Alicia E. Torres-García Ramón Gonzalo Pérez-Escudero, José M. and Iñigo Ederra. A gap waveguide-based compact rectangular waveguide to a packaged microstrip inline transition. In *Applied Sciences 10, no. 14: 4979.* doi: https://doi.org/10.3390/app10144979.

[34] Kazuyuki Seo. Planar microstrip-to-waveguide transition in millimeter-wave band. In Ahmed Kishk, editor, *Advancement in Microstrip Antennas with Recent Applications*, chapter 11. IntechOpen, Rijeka, 2013. doi: 10.5772/54662. URL `https://doi.org/10.5772/54662`.

[35] Kazuyuki Seo, Kunio Sakakibara, and Nobuyoshi Kikuma. Microstrip-to-waveguide transition using waveguide with large broad-wall in millimeter-wave band. In *2010 IEEE International Conference on Ultra-Wideband*, volume 1, pages 1–4, 2010. doi: 10.1109/ICUWB.2010.5614169.

[36] Nguyen Thanh Tuan, Kunio Sakakibara, and Nobuyoshi Kikuma. Bandwidth extension of planar microstrip-to-waveguide transition by via-hole locations at both sides of microstrip line. In *2019 IEEE International Symposium on Antennas and Propagation and USNC-URSI Radio Science Meeting*, pages 673–674, 2019. doi: 10.1109/APUSNCURSINRSM.2019.8888571.

[37] Yuki Ishikawa, Kunio Sakakibara, Yuta Suzuki, and Nobuyoshi Kikuma. Millimeter-wave topside waveguide-to-microstrip transition in multilayer substrate. *IEEE Microwave and Wireless Components Letters*, 28(5):380–382, 2018. doi: 10.1109/LMWC.2018.2812125.

[38] Kunio Sakakibara, Tuan Nguyen, Nobuyoshi Kikuma, and Toshikazu Hori. Bandwidth comparison of topside waveguide-to-microstrip transitions with back-short waveguide and with double-layer substrate in millimeter-wave band. In *2019 13th European Conference on Antennas and Propagation (EuCAP)*, pages 1–4, 2019.

[39] Kazuyuki SEO, Kunio SAKAKIBARA, and Nobuyoshi KIKUMA. Narrow-wall-connected microstrip-to-waveguide transition using v-shaped patch element in millimeter-wave band. *IEICE Transactions on Communications*, E93.B (10):2523–2530, 2010. doi: 10.1587/transcom.E93.B.2523.

[40] Eray Topak, Jürgen Hasch, and Thomas Zwick. Compact topside millimeter-wave waveguide-to-microstrip transitions. *IEEE Microwave and Wireless Components Letters*, 23(12):641–643, 2013. doi: 10.1109/LMWC.2013.2284824.

[41] Ziqiang Tong and Andreas Stelzer. A vertical transition between rectangular waveguide and coupled microstrip lines. *IEEE Microwave and Wireless Components Letters*, 22(5):251–253, 2012. doi: 10.1109/LMWC.2012.2192719.

[42] H. R. Kaupp. Characteristics of microstrip transmission lines. *IEEE Transactions on Electronic Computers*, EC-16(2):185–193, 1967. doi: 10.1109/PGEC.1967. 264815.

[43] D. F. Williams, J. Jargon, U. Arz, and P. Hale. Rectangular-waveguide impedance. In *2015 85th Microwave Measurement Conference (ARFTG)*, pages 1–5, 2015. doi: 10.1109/ARFTG.2015.7162902.

[44] Yujian Li, Lei Ge, Junhong Wang, Shan Da, Di Cao, Jingxue Wang, and Yang Liu. 3-d printed high-gain wideband waveguide fed horn antenna arrays for millimeter-wave applications. *IEEE Transactions on Antennas and Propagation*, 67(5):2868–2877, 2019. doi: 10.1109/TAP.2019.2899008.

[45] Haohan Yao, Shilpi Sharma, Rashaunda Henderson, Solyman Ashrafi, and Duncan MacFarlane. Ka band 3d printed horn antennas. In *2017 Texas Symposium on Wireless and Microwave Circuits and Systems (WMCS)*, pages 1–4, 2017. doi: 10.1109/WMCaS.2017.8070701.

[46] D. Pozar and D. Schaubert. Scan blindness in infinite phased arrays of printed dipoles. *IEEE Transactions on Antennas and Propagation*, 32(6):602–610, 1984. doi: 10.1109/TAP.1984.1143375.

[47] Sophocles J. Orfanidis. Electromagnetic waves and antennas. http://eceweb1.rutgers.edu/ orfanidi/ewa. *Online Book*.

[48] R.H.J. Cary. Radomes. *Online Book*.